Technische Universiteit Delft

Flood wave monitoring using LSPIV

A methodology for monitoring flood waves in an equatorial urban stream with fast response time

TU Delft

G. H. Gerritsen

On the cover

View on the gauging site at the Chuo Kikuu combined with outlines of the discharges found using the LSPIV method and precipitation rates observed at a nearby TAHMO station.
Dar es Salaam, Tanzania, December 2019
G. H. Gerritsen

Flood wave monitoring using LSPIV

A methodology for monitoring flood waves in an equatorial urban stream with fast response time

by

G.H. Gerritsen

to obtain the degree of

Master of Science
in Civil Engineering

at Delft University of Technology,

to be defended publicly on Thursday August 13, 2020.

Student number:	4274164	
Supervisor:	Dr. ir. H. C. Winsemius	TU Delft
Thesis committee:	Prof. dr. ir. M. Kok	TU Delft
	Ir. F. O. Annor	TU Delft
	Ir. W. M. J. Luxemburg	TU Delft

An electronic version of this thesis is available at https://repository.tudelft.nl/

Examples of coding used for this thesis are available at
https://github.com/ghgerritsen/ThesisLSPIV

TU Delft

Preface

This report illustrates my end point of the Masters degree Water Management at Delft University of Technology. It discusses the use of Large-Scale Particle Image Velocimetry (LSPIV) to estimate discharges during a flood wave: is it possible to determine how much water is flowing through a river with only the use of a camera (and a few other things).

During this final phase of my student's life I have been able to dive deep into one single subject, explore a new continent, and experience the nearness of so many people. It is these people who I want to thank for their support.

First of all, I want to thank my supervisor Hessel Winsemius. Your unapproachable enthusiasm for the work you are doing, countless discussions and thorough feedback have not only improved this thesis, but has shown me what so valuable in the execution of research and beyond. I also want to thank the other members of my committee for their valuable feedback: Matthijs Kok, Frank Annor, and of course Willem Luxemburg.

Furthermore, I want to thank the people from HOT and OMDTZ, where I could stay and work during my time in Dar es Salaam, and helped me out during my fieldwork. Even more a thank you to Freddie Mbuya. Thank you for your willingness to help me setting up a gauging site, and letting me use your home to work from.

Lastly, I want to thank my family, friends, people from *het hokje* and all others who have been providing support and new insights during these final stages of my masters. It has been a wonderful experience.

Dankjulliewel.

G.H. Gerritsen
Delft, August 2020

Abstract

An increasing amount of Earth's population are living in urban environments near deltas, estuaries, and coastal areas. Areas which are increasingly prone to flooding due to land degradation and increasing rainfall intensities. To be able to develop warning systems for flood events, create precipitation-runoff relationships, validate runoff models, or simply to understand the behaviour of the rivers in these cities, understanding of the amount of water flowing through these rivers is needed. The low-cost and novel gauging method using Large-Scale Particle Image Velocimetry (LSPIV) could complement discharge measurements at locations and stages where the possibilities of using traditional gauging methods are limited. This report investigates the feasibility of using LSPIV to quantify river discharges in an equatorial urban stream with fast response time.

LSPIV uses videos to extract the surface flow velocities by tracing the movements of seeds on the water's surface. Combined with the local bathymetry and water level, an estimation of the river's discharge can be made. This study consists of two sets of experiments. The first set of experiments were performed at the Dommel regarding (1) processing software, (2) image preparation, (3) seeding densities, and (4) point of views and discussed by assessing their accuracy relative to benchmark measurements – based on the mean error (ME) and root mean squared error (RMSE) – and the method's precision – based on the relative standard deviation (RSD). Results of these experiments showed that the Python library OpenPIV performs similar to the more widely used Fudaa-LSPIV, and additional contrast correction provides limited improvements, if the appropriate correction is applied. As can be expected, increased seeding densities result in increased precision and accuracy. For no artificial seeding the RSD and RMSE are 1.827 and 0.322 respectively. For extensive artificial seeding values of 0.520 and 0.188 are found. A minimum amount of 10% of the water surface should be covered with seeds for acquiring reasonable results. Due to multiple unknown factors, no conclusions on the point of view of the camera could be made. According to literature an inclined angle between 15°and 30°relative to nadir provide the best results.

The second set of experiments were performed along the Chuo Kikuu, Dar es Salaam, Tanzania, to assess whether LSPIV can be used to monitor flood waves in an equatorial urban stream with rapid response time. A flood wave was monitored through the capture of 73 5 second videos. These videos were turned into separate frames and corrected for lens distortion and perspective distortion. Thereafter the frames were gray scaled and gamma correction was applied. After the LSPIV process additional filtering removed unrealistic low flow velocities, and through substitution missing velocities were replaced with flow velocities based on the vertical logarithmic progression relationship between the surface flow velocities and water depth. The surface flow velocities found using this method match optical observations. Discharges were estimated using the empirical depth-average coefficient and local bathymetry. Results showed that the post-processing reduces the uncertainty bandwidth with 37% and increases the mean flow velocities with 96%.

The found discharges were compared with precipitation measurements observed at a nearby TAHMO meteorological station. The total volumetric precipitation was determined by estimating the contributing catchment using a digital elevation map (DEM) and the locations of man-made drainage systems. When comparing the volumetric precipitation with the flood wave, a runoff coefficient of 53% [35-68] is found. This coefficient falls within the ranges found in literature, but is probably an underestimation of the true runoff due to an overestimation of the catchment area.

This study shows that the LSPIV method is feasible for continuously monitoring flood waves in an urban environment. Especially during peak flows LSPIV proves to be valuable, as observations using conventional gauging methods are labour intensive, unsafe, or not executable. Because of the possibility to monitor streams from a distance – which ensures access to power and safety against vandalism – there is a possibility to observe complete flood waves at regular intervals without the need for direct contact with the water. For Dar es Salaam, this method opens doors for continuous and secure stream monitoring, at low costs and with local devices.

Contents

1

Introduction

The majority of humanity, either living in urban or rural areas, live approximately within a 3 kilometre radius of a fresh water source (Kummu et al., 2011). Traditionally, humanity chose to inhabit places close to rivers, lakes and coasts to ensure water supply for domestic use, agriculture and livestock, and for fishery (McCool et al., 2008). Over time, especially coastal delta cities were able to flourish due to ease of communication, transportation, and industrial and agricultural production (Krueger et al., 2012). Nowadays, the majority of the largest cities are located along the coast and most of them are situated in delta regions (Adnan and Kreibich, 2016). Currently about 55 percent of Earth's population lives in urban areas[1], it is expected that in 2030 this will be 60 percent and in 2050 over 68 percent (United Nations, 2019). Especially in less developed regions the urbanisation will be growing with the highest rate. Furthermore, it is expected that most of the world's population will cluster around cities near deltas, estuaries and coastal areas (Dircke et al., 2010; Hanson et al., 2011).

Due to this ongoing urbanisation, and as many cities are located alongside rivers, the number of people threatened by flood events is rising and therefore the impact is increasing. Besides the urbanisation, it is expected that future climate change will exacerbate land degradation processes and increase rainfall intensities according to the Intergovernmental Panel on Climate Change (IPCC) (Arneth et al., 2019), both resulting into more severe flood events worldwide. Over the past century, the global temperature increased, especially over the past 50 years, and the temperature is expected to rise even further over the coming decades. These increasing temperatures, which undoubtedly leads to rising sea levels, does not only affect coastal cities (McGranahan et al., 2007; Neumann et al., 2015; Nicholls et al., 2018), but has an impact on the hydrological cycle as a whole, by intensification of precipitation events, increasing evaporation and changing runoff (Huntington, 2006). These changes are highly climate zone dependent. While mid-latitude regions will probably encounter decreasing runoff, due to increased evaporation; equatorial and high-altitude regions will experience more severe droughts, and due to more severe precipitation events, an increase in runoff, leading to more severe flooding events (Arnell, 1999; Probst and Tardy, 1987).

In order to provide sustainable living conditions and to be able to develop warning systems for flood events, create precipitation-runoff relationships, validate runoff models, or simply to understand the behaviour of these rivers, having thorough knowledge of river flows through urbanised environments is of great importance. For this, collection of relevant hydro- and meteorological data is needed. However, as is stated by Ruhi et al. (2018), the number of discharge gauging stations internationally has been declining over the past years, mainly due to rising maintenance costs and the lack of funding. Despite the general decline of gauging stations the station network continues to be relatively dense and operational in Europe, North America, Japan and South Africa. However, in central Asia, the Arctic, and large parts of Africa large monitoring gaps remain (Fekete et al., 2012), resulting in insufficient information resources for hydro- and meteorological use .

Currently, the conventional way of determining river discharges is by using the volumetric method, tracer

[1]There is not one definition for an *urban environment*. The United Nations follows for each country separately the local definition.

dilution method or velocity-area method – using a current meter or an Acoustic Doppler Current Profiler (ADCP) (Gore and Banning, 2017). However, these methods are either labour intensive, expensive, or not applicable in extreme weather conditions. In the search for a remote and more cost efficient stream gauging method, hydrometry teams all around the world are looking for alternative methods and instruments (Tauro et al., 2018). One of these potential low-cost monitoring tools is Large-Scale Particle Image Velocimetry (LSPIV) which gives the opportunity to acquire surface flow velocities in the temporal and spatial domain with use of only a camera to shoot videos with, and a computer to process the acquired data. This method was first used in 1970 to track cloud movements (Leese et al., 1971). Nowadays different teams are working on further developing this method for hydrometric purposes, as it opens the possibility to estimate river flow velocities and discharges without to need for having physical contact with the water (Guillén et al., 2017; Hauet et al., 2008; Muste et al., 2010; Tauro et al., 2014b).

1.1. Research motivation

In and around the Msimbazi basin the largest city of Tanzania is located: Dar es Salaam. It is the leading commercial and economic hub of Tanzania and provides the majority of the country's GDP (Todd et al., 2019). Over the past decades the city has experienced rapid urbanisation: Dar es Salaam is the fasted growing city in the region and it is expected that Dar es Salaam will reach the 10 million mark in 2029 (United Nations, 2019). Besides this, over the past years Dar es Salaam has experienced more frequent and more severe flood events (Todd et al., 2019; World Bank, 2019). These flood events are a threat to 1 million inhabitants directly. In order to address these flood problems the Tanzanian Government, World Bank and United Kingdom Department for International Development set up the Tanzania Urban Resilience Program (TURP). The framework of this program is defined into three pillars: (1) Risk Identification, (2) Risk Reduction and (3) Disaster Preparedness & Emergency Management.

As part of the pillar *Disaster Preparedness & Emergency Management* an early warning system is under development by Deltares, TU Delft, FloodTags and the Tanzanian Red Cross Society. The project – known as the Community Water Watch project (CWW) – launched in October 2018 to design an early warning system for the Msimbazi basin that relies on open online media communication channels, weather stations of TAHMO and hydrological models.

In order to improve this early warning system, it is of great importance to have thorough understanding of the river system and therefore the amount of water flowing through the streams. However, within the urban environment, it is difficult to set up an advanced gauging station due to the possibility of vandalism. LSPIV can be an interesting choice for determining these discharges. Not only because it provides the possibility to observe river flows from a secured locations, but also due to the possibility to measure discharges during high runoff events – which is nearly labour intensive, impossible, or dangerous using conventional methods.

1.2. Aim of this research

This research aims to explore whether it is feasible to use LSPIV for measuring flow velocities at streams located in an equatorial, urban environment. The feasibility of using LSPIV is partly dependent on how processing methods and environmental conditions affect the accuracy and precision of the flow velocity estimates, and whether it is possible to distinguish different stages in flood waves. Therefore, the goal of this research is to answer the following question:

Is Large-Scale Particle Image Velocimetry a feasible method for monitoring flood waves in a stream located in an equatorial urban environment with a fast response time?

In order to answer this main research question, three sub-questions are defined. These questions are as follows:

1. *What is the impact of different processing methods and environmental conditions on the accuracy and precision of LSPIV and how do these results compare with conventional methods?*

   To assess the accuracy and precision of LSPIV, data obtained at the stream Dommel in the Netherlands is examined. This is achieved using different processing methods – such as

the different types of processing software and different image manipulation approaches – and considering different environmental conditions – like different seeding densities and points of view. The performance of LSPIV is quantified by relating the results to benchmark measurements obtained with a conventional gauging method (OTT current meter).

2. *Can LSPIV be used for reconstructing flood waves in an equatorial fast response time urban stream?*

   A flood wave is reconstructed using LSPIV with use of 72 videos obtained at the Chuo Kikuu – a small stream in Dar es Salaam, Tanzania. Using these videos, surface flow velocities are determined. After this, discharges can be determined using an empirical depth-averaged coefficient, water levels and the local bathymetry.

3. *How do discharges obtained using LSPIV relate to nearby monitored precipitation?*

   The discharges, obtained in the previous sub-question, are compared with the total volumetric precipitation falling in the corresponding catchment area to obtain the catchment's runoff coefficient. This coefficient gives an insight in whether the measurements obtained using LSPIV give eligible results.

1.3. Thesis outline

In Chapter 2 a theoretical framework is presented containing an introduction to hydrology in the urban environment, combined with the expected impact of changing climate and urbanisation on the (urban) water cycle. Thereafter, an elaboration on conventional gauging methods applied to determine river discharges is presented – discussing their advantages and weaknesses – and an outline on novel gauging methods is provided, including LSPIV. Lastly, the different components of the LSPIV method for collecting discharges is treated. Chapter 3, presents topographical and geographical information of the study sites the Dommel, a small stream in the Netherlands, and the Chuo Kikuu, a stream in Dar es Salaam, Tanzania.

In Chapter 4 the first sub-question is discussed, providing an insight on the impact of different processing methods and environmental conditions on the accuracy and precision of the LSPIV method, using videos obtained at the Dommel. Chapter 5 presents the results of the second sub-question, elaborating the process of acquiring surface flow velocities using LSPIV and converting these flow velocities into discharge estimations. In Chapter 6 the previously found discharges are related to the corresponding precipitation event, by comparing their total volumes. Both Chapters 5 as 6 make use of data obtained in Dar es Salaam, Tanzania.

In Chapter 7 the LSPIV method is discussed by considering the impact of the different processing assumptions, study site related inaccuracies and other steps which lead to the possible incorrectness, and how these results compare with conventional gauging methods. Subsequently, Chapter 8 present the final conclusions for the different sub-questions and main research question.

Lastly, in Chapter 9 recommendations are provided for setting up an LSPIV gauging station and for further research and for. In Appendix A a guide on applying LSPIV is provided.

2

Theoretical framework

This chapter treats three parts: (1) why do we need to gauge discharges in the urban environment, (2) what different techniques can be used for monitoring river discharges, and (3) how can Large-Scale Particle Image Velocimetry (LSPIV) be applied for river monitoring. The first part is discussed in Section 2.1, where the urban water cycle and risks for flood events in the urban environment is discussed. In Section 2.2 different conventional and novel methods for monitoring river discharges are treated. Section 2.3 treats the history and use of Particle Image Velocimetry as novel monitoring tool and its potential for acquiring river discharges in streams with fast response times. Lastly, Section 2.4 discusses the LSPIV methodology, as applied in this study.

Box 2.1: Types of flooding

Within the urban area, there are four different types of flood to distinguish. These types, together with their causes are (Jonkman, 2005):

Coastal flooding	Urban areas located to the coast can experience during wind storms and low atmospheric pressure floods due to set-up of water levels on the coast. Especially during local astronomical high tides, this can leas to extreme high water levels and severe flooding of the coastal area.
Flash flooding	During high intensity rain events quick raise of water bodies might occur. The time available to predict flash floods is limited. This type of flooding mainly occurs in mountainous areas.
Fluvial flooding	Fluvial, or river flooding occurs when a river exceeds its capacity and flows outside its regular boundaries. This can be accompanied by breaches in dikes or dams next to the river. Fluvial flooding is mainly caused by extended periods of precipitation in the upstream catchment, melting snow or due to a blockage in the river.
Pluvial flooding	Pluvial flooding, or ponding is caused by precipitation events which exceeds the capacity of the local drainage systems.

2.1. Water and the urban environment

Within the urban area, people are prone to different types of flooding, as is provided in Box 2.1. Within this research, it is tried to contribute to gauging methods for *fluvial* flooding. Fluvial flooding is mainly an consequence of increased by precipitation in the upstream area, resulting into rivers beds exceeding its regular boundaries. In order to understand this water recycling system on Earth, Figure 2.1a presents the different steps within this hydrological cycle on a global scale.

This hydrological cycle has no starting point nor an ending point. For hydrologists it is the basis for understanding the sources of water on and under the earth's surface and its consequent movement by various pathways back to the principle storage in the oceans (Chow et al., 1968). The main process of the hydrological cycle is as follows: water *evaporates* from (a_1) water bodies and (a_2) land. This water is transported as vapour until it (b) *condensates* and eventually (c) *precipitates* as rain or snow. Whenever the precipitation occurs on land, the water will either be *intercepted* by vegetation, discharged as (e) *surface flow* or (d) *infiltrate* into the ground. After infiltration, water will be discharged as (f) *subsurface flow* or recharge the deep ground water storage where (g) *groundwater flows* occur.

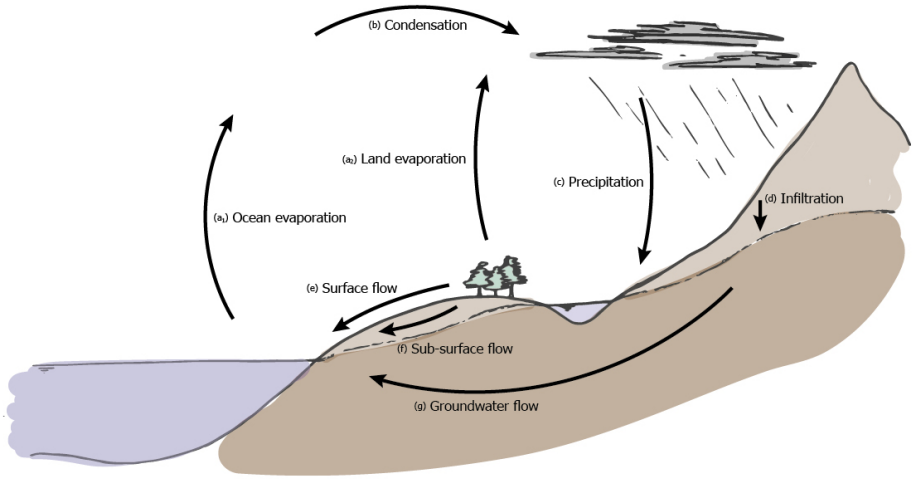

(a) The hydrological cycle.

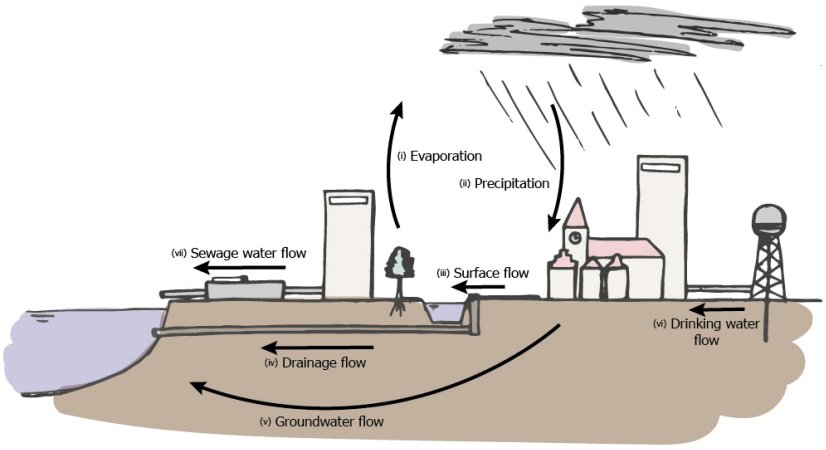

(b) The urban water cycle.

Figure 2.1: Schematic representations of the hydrological cycle and its urban water cycle component. The hydrological cycle consists of water evaporating from land and water bodies, and eventually precipitating. Through groundwater- and surface flows the cycle is closed. Three main differences between the rural and urban area water cycle are the infiltration rate -due to the presence of paved areas-, the flux of the sewerage system and the inflow of drinking water.

The urban environment and related urban water cycle forms a separate part within the hydrological cycle, as the water system in an urban area diversifies from that in a rural area in a number of points. As shown in Figure 2.1b, there is (i) *evaporation*, (ii) *precipitation* and (v) *groundwater flux*, but due to the presence of (partly) impermeable surfaces, less water is able to infiltrate into the subsurface and will mainly flow into drainage systems and open water bodies as (iii) *surface flow*. Beside this, fluxes are altered due to *groundwater extraction*, *import of water* from outside the region (vi) and the generation of *wastewater* (vii). When there is an absence of a drainage system, or the system does not meet the requirements for coping with high intensity precipitation events, *pluvial* flooding might occur.

Especially in dense urban areas, where there are little to no attributing floodplains for streams and rivers during flood waves, and limited storage capacity for rainwater is present during intense precipitation events, fluvial and pluvial flooding will occur frequently and have an impact on large amounts of people. In these regions, a more thorough understanding of the amount of precipitation, surface runoff and river discharges can benefit in mitigating flood events by developing flood warning systems and by adjusting the urban environment.

2.2. River gauging methods

To acquire river discharge information to use for developing early warning systems, creating precipitation-runoff relationships, validate runoff models, or to understand the behaviour of streams, several options are available. The different discharge gauging options can be divided into two groups: (1) conventional gauging methods, which cover methods which are currently widely used for hydrological purposes and have proven their value in different uses, (2) novel gauging methods, which try to provide alternatives for when conventional gauging methods fall short. The upcoming sections provide an brief and incomplete overview on the current state of these methods.

The applicability of a gauging method mainly depends on the goal of the measurements: is there a need for continuous discharge measurements, or does an incidental measurement suffice. Most gauging methods are only suitable for the latter, as acquiring point measurements is an labour intensive activity. To be able to estimate discharges continuously, these point measurements are then combined to establish a rating curve, where discharges are related to the water level.

2.2.1. Conventional river gauging methods

Velocity-area methods
The velocity-area method depends on measuring average flow velocities and the cross-sectional area of the stream. The discharge is then determined following Equation 2.1

$$Q = A \cdot v \tag{2.1}$$

where Q is the stream's discharge in [m³/s]; A the stream's cross-sectional area in [m²]– based on the bathymetry and water level –; and v the average flow velocity in [m/s].

There are several ways to estimate the average flow velocity of the river. The first method is using *floaters*. By throwing buoyancy floaters[2] into the stream, either the surface flow velocity can be estimated – if the object solely acts at the water surface level – or estimates for the average flow velocities – e.g. with use of a canister float or rod float – can be made. If the surface flow velocities are measured, the average flow velocities are estimated with use of the empirical depth-average coefficient – for shallow streams this coefficient is estimated at 0.7. As the use of this coefficient result in high uncertainties, a more accurate method is the use of a current meter.

The *current meter* measures flow velocities by counting the rotations of the current meter's impeller. Using the current meter, flow velocities at different depths and width sections can be measured. This way, a spatial distribution of flow velocities in the cross-sectional plain can be made. In general, to minimize amount of measurements, the average flow velocity is determined using the average of the flow velocities at $0.2 \cdot D$ and $0.8 \cdot D$ – where D is the local stream depth – or using the $0.6 \cdot D$ flow velocity as estimation for the average flow velocity.

[2] floaters with the same density as the fluid.

When dividing the cross-section in different sections, Equation 2.2 is solved

$$Q = \sum_{n=1}^{N} v_n \cdot d_n \cdot b_n \tag{2.2}$$

where v_n, d_n, and b_n are the section's depth-averaged flow velocity, depth and width, respectively. Using current meters are can be labour intensive, but is applicable in many different types of streams and rivers.

A more automated approach is the use of an *Acoustic Doppler Current Profiler* (ADCP). Usually mounted to a (small) boat, the ADCP simultaneously measures the stream's depth and flow velocities through the use of changes in phase of sound waves – known as the Doppler effect. Both a well calibrated current meter as an ADCP are relative expensive equipment. Besides this, an ADCP needs an minimum stream depth, but gives the possibility to acquire accurate discharges in various (flow) conditions.

Dilution gauging

A third option of estimating discharges through dilution gauging. By injecting a known quantity of a tracer to the stream, and observe how the concentration changes further downstream – at a point where the tracer is fully mixed – discharges can be estimated. Usually, salt is used as tracer and the concentration is traced back from the electro conductivity. In Figure 2.2 a schematic view of the method is proved. The discharge is estimated using the following formulas:

$$Q = \frac{M}{\sum \phi_t \cdot \Delta t} \tag{2.3}$$

$$\phi_t = ([EC_t - EC_0]) \cdot f \tag{2.4}$$

where ϕ_t is the concentration at time t; Δt is the time step; EC_t the electro conductivity at time t [μS/cm³]; EC_0 the background electro conductivity [S/m]; and f the factor to convert electro conductivity into concentrations. The latter is dependent on temperature and background chemistry.

Dilution gauging can potentially be executed in every type of stream. However, as stream flows increase, so does the amount of tracing material needed to be able to observe substantial changes in concentration.

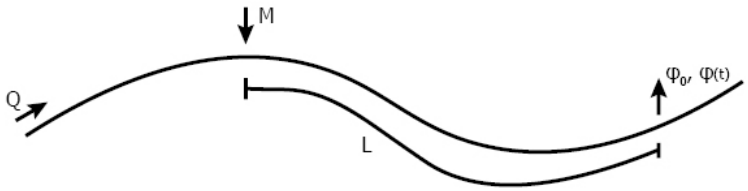

Figure 2.2: Schematic view on the dilution method. At a point in the river volume M of a tracer is added to the river. Downstream – where the tracer is fully mixed with the river – the changes in concentration ϕ are measured. Using these observations, the discharge of the river can be estimated.

Structural methods

Where previous methods require manual labour to acquire discharges, structural methods provide less intensive manual labour. Discharges are related to the water level – or stage – of the stream at locations where it is flowing over a artificial object – usually a weir. For smaller streams a V-notch weir is mostly used. For larger streams, besides weirs – e.g. the Cipolleti weir or a compound weir – trapezoidal flumes can be used. In Figure 2.3 several types of weirs are presented.

Structural methods can be costly – especially for larger streams – and can lead to changes in river behaviour downstream. They are usually applied in artificial channels – to regulate the amount of water flowing into a certain area – and downstream of dams – to check the discharge ejected.

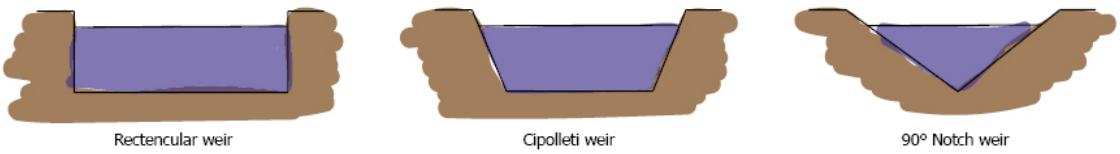

Figure 2.3: Different types of weirs, used for discharge estimations.

Slope-area methods
The most common slope-area method is based on the Manning Equation (see Equation 2.5). This method relies mainly on a correct estimation of Manning's Roughness, usually determined using one of the previous methods.

$$Q = \frac{A \cdot R^{2/3} \cdot i^{1/2}}{n} \tag{2.5}$$

where A is the cross-sectional area [m²]; R the hydraulic radius [m] – which is the cross-sectional area divided by the wetted perimeter –; i the slope of the stream's surface [m/m]; and n Manning's Roughness [s/[$m^{1/3}$]]– usually between 0.025 and 0.07 for natural streams.

2.2.2. Novel river gauging methods

In Tauro et al. (2018) novel river gauging methods are gathered, which are currently researched by different research groups world wide. The researches mainly focus on new methods for estimating water levels and velocities of the surface water remotely. This way, now under observed – e.g. flood waves – can be monitored. Therefore, these methods keep to rely on empirical formulas and rating curves. Among others, the following ideas are currently worked on:

- *Water level estimation based on satellite imagery* Already since the 1980s satellite imagery is used to estimate water levels. This method is now mainly applied on reservoirs, but as the imagery resolution becomes denser, smaller water bodies are observable.
- *Flow velocity estimation based on satellite imagery* Using optical, multispectral, and passive microwave multispectral sensors flow velocities can be estimated and converted to discharges, even if the cross-sectional geometry is unknown.
- *Horizontal Acoustic Doppler Current Profiler* Where the ADCP detects flow velocities in the vertical plain – which result in the need of crossing the river – current research is looking into adopting the technique for horizontal measurements of the flow velocities under water and at the near surface (H-ADCP).
- *Surface flow velocity estimation using radar* A potentially cheap and easy to use solution for quickly acquiring surface flow velocities could be the use of radar sensors (SVR).
- *Surface flow velocity estimation using high-resolution imagery* Using imagery, seeds on the stream's surface can be traced and converted into flow. velocities (PIV).

The latter novel gauging method – PIV – is considered in this thesis. An outline of the history and different methods are provided in the following sections.

2.3. Particle Image Velocimetry

In the following section an introduction to the history and development of particle image velocimetry (PIV) is presented combined with the current state of affairs. In the following section the methodology of the PIV version used in this research is provided (*see* Section 2.4).

PIV is a widely used method within laboratories (Adrian, 1991). In controlled volumes displacements of particles – or seeds – are tracked through imagery. By obtaining the displacement of a particle, or group of particles between two frames – based on a Gaussian fit – velocities over a large plain can be estimated. An schematic view of an experimental setup is shown in Figure 2.4.

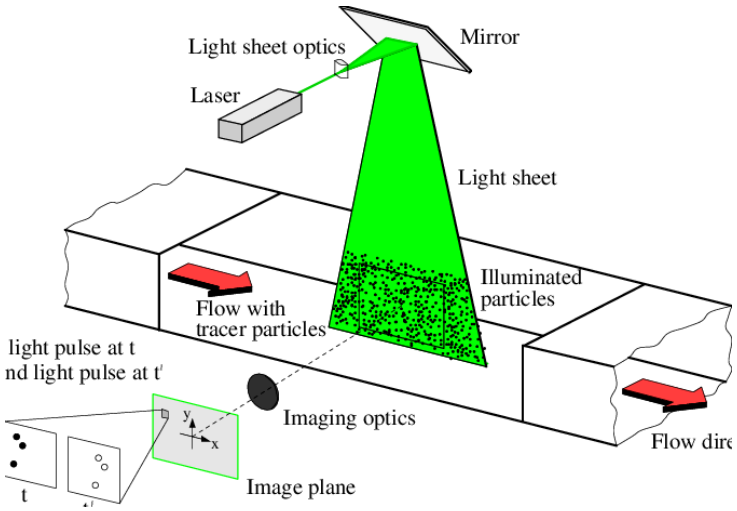

Figure 2.4: Experimental setup for PIV recording in a wind tunnel (from Kompenhans et al., 2000).

One of the first attempts to apply this method in the field was using satellite imagery for tracing movement of clouds (Leese et al., 1971), and sea ice (Collins and Emery, 1988). In the 1990s the first application of PIV on rivers were made by Fujita and Komura (1994). As PIV at much larger scales than in laboratory setups, the technique was renamed to Large-Scale Particle Imagery (LSPIV). An schematic view on the LSPIV method is provided in Section 2.4.2.

An alternative to the grid-based PIV approach is the use of particle tracing velocimetry (PTV) method where individual seeds are recognised and followed over time using a Lagrangian approach (Tauro et al., 2017, 2019). Other options are methods like the space-time image velocimetry (STIV) (Fujita et al., 2007), and dimensionality reduction algorithms (Tauro et al., 2014a).

The LSPIV is currently widely examined by different research groups around the word (e.g., Fujita et al., 1998; Hauet et al., 2008; Tauro et al., 2014b, 2016c; Xue et al., 2014). Techniques like LSPIV provides the possibility to acquire discharges over a continuous period of time, without the need for having physical contact with the stream. Especially in streams with fast response times and torrential runoff LSPIV proves to be one of the few alternatives te estimate discharges and creating rating curves (Stumpf et al., 2016). Besides this, relative to other alternatives, LSPIV proves to be a low-cost gauging method.

Muste et al. (2008) found in a elaborate review on LSPIV that errors ranges between 2-35%. The main factors influencing the results negatively are (1) seeding density, (2) identification and ground control points – and therefore the orthorectification process – (3) camera distance, and (4) the sampling time – i.e. frame rate – (Kim, 2006). Currently, the LSPIV method is mainly applied for short term purposes. Only a handful researches have applied LSPIV on the long term (Hauet et al., 2008; Le Coz et al., 2014; Stumpf et al., 2016).

2.4. Applying Large-Scale Particle Image Velocimetry

The basic principle of using LSPIV for determining surface flow velocities, is tracing particle displacements by analysing small regions (or interrogation areas) of consecutive frames through validating their similarities. The complete LSPIV method consist of three major parts: (1) the image preparation (*see* Section 2.4.1), (2) the PIV processing (*see* Section 2.4.2) and (3) the data analysis. Box 2.2 provides the general process of the method. In Appendix A an step-by-step procedure for determining discharges from scratch is provided.

Box 2.2: From video to discharge

To acquire discharges from videos, the following three steps are executed: (1) image preparation, (2) PIV processing, and (3) data analysis and discharge determination. To determine the discharge, the local bathymetry, water level, and the locations of at least four visible ground control points (GCPs) are needed.

Image preparation
Image preparation is needed to be able to better distinguish moving patterns from the imagery, and to remove image perspective effects. Usually, this consists of the following steps:

1. Lens distortion correction based on camera characteristics.
2. Video stabilisation
3. Image orthorectification based on local GCPs.
4. Gray scaling, contrast- and gamma correction.

PIV processing
Using a chosen software, displacements of traceable seeds – either naturally occurring or artificially added – are computed. The following basic steps take place:

1. Division of single images into grid cells (interrogation windows).
2. Determine displacements using correlation within the search area.
3. Determine velocity per interrogation window (x, y) by dividing the displacement over the frame time period.

Data analysis and discharge determination
After acquiring the different velocity maps, the data can be analysed as needed – for instance by applying additional filtering or replacing unlogical flow velocities. discharges can then be estimated by executing the following steps:

1. Determine time-averaged surface flow velocities.
2. Determine depth-averaged flow velocities (using an empirical based relationship).
3. Determine discharge using the velocity-area method.

2.4.1. Image preparation

The image manipulation to prepare the imagery for the LSPIV analysis consist of several steps. Subsequentially these steps are : (1) lens distortion correction, (2) stabilisation, (3) orthorectification and (4) Gray scaling, gamma- and contrast correction. The first three steps are applied to ensure equal distances are present within the imagery. The fourth step is used to improve the seed's distinguishability from the background and therefore making sure the similarity validation process is effective. There are several software which give the possibility to apply image manipulation options, like OpenCV[3].

[3]OpenCV is an open source image processing library which can be used cross-platform.

Lens distortion correction

Due to the lens curvature of the camera, imagery can be distorted. Figure 2.5 presents the two most appearing lens distortion types, namely barrel distortion – also known as fish eye distortion – and pincushion distortion (Fryer and Brown, 1986). These distortions are related to radial factors. A third type of distortion is tangential distortion, which occurs when lenses are not parallel to the image plain. Some cameras are able to cope with these distortions internally. However, most of the time some amount of post-processing is needed to adjust the imagery.

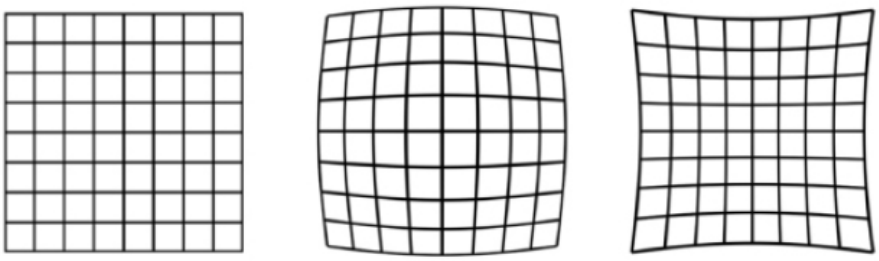

Figure 2.5: Different lens distortion types. From left to right: the original grid, barrel distortion, and pincushion distortion.

The following formulas are applied to remove radial (*see* Equation 2.6) and tangential distortions (*see* Equation 2.7)

$$\begin{aligned} x_{corr} &= x(1 + k_1 r^2 + k_2 r^4 + k_3 r^6) \\ y_{corr} &= y(1 + k_1 r^2 + k_2 r^4 + k_3 r^6) \end{aligned} \tag{2.6}$$

where x and y are the original coordinates; x_{corr} and y_{corr} the distortion corrected coordinates; r the distance of point (x, y) to the distortion centre; and k_1, k_2, and k_3 the radial distortion coefficients. For pure barrel- and pincushion distortion, k_1 is negative and positive, respectively. k_2 and k_3 can be neglected.

$$\begin{aligned} x_{corr} &= x + [2p_1 xy + p_2(r^2 + 2x^2)] \\ y_{corr} &= y + [p_1(r^2 + 2y^2) + 2p_2 xy] \end{aligned} \tag{2.7}$$

where p_1 and p_2 are the tangential distortion coefficients. The different coefficients are often stored in an array:

$$C_{dis} = \begin{bmatrix} k_1 & k_2 & p_1 & p_2 & k_3 \end{bmatrix}$$

Besides the distortion coefficient, to be able to correct the imagery, a conversion between the distortion coordinates and camera resolution is made. For this, the formula as given in Equation 2.8 is used.

$$\begin{bmatrix} x \\ y \\ w \end{bmatrix} = M_{con} \cdot \begin{bmatrix} X \\ Y \\ Z \end{bmatrix} \quad \text{where} \quad M_{con} = \begin{bmatrix} f_x & 0 & c_x \\ 0 & f_y & c_y \\ 0 & 0 & 1 \end{bmatrix} \tag{2.8}$$

where $[x, y, w]$ are the 2D homogeneous image coordinates and $[X, Y, Z]$ the 3D camera coordinates, f_x and f_y are the camera focal lengths in the x and y direction – usually, they are equal to each other – and c_x and c_y are the x and y component of the optical centre.

Stabilisation

After applying lens distortion correction, possible imagery movements can be removed by applying video stabilisation. The main steps of stabilisation are (1) extracting key points on two sequential frames, (2) matching the points on the two frames, (3) estimating the geometrical transformation, and (4) correcting for the movement.

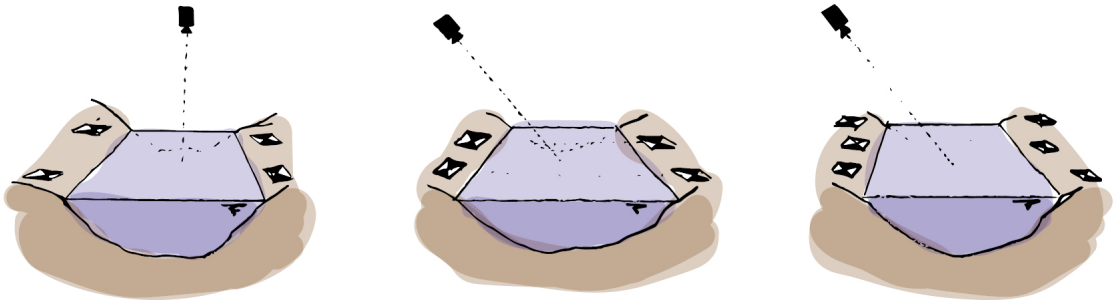

(a) When filming perpendicular to the stream, 4 GCPs are needed.

(b) When filming with an incline, 4 GCPs are needed when they are in the same plane as the water surface level.

(c) When filming with an incline, 6 GCPs are needed when they are in different planes than the water surface level.

Figure 2.6: Number of ground control points (GCPs) needed in different circumstances.

Image orthorectification

To remove the effects of image perspective – where objects closer to the camera seem to be larger than objects in the background – orthorectification is applied. When applying orthorectification, the coordinate system of the imagery are transferred to a local coordinate system. For this local coordinate system ground control points (GCPs) – set up alongside the stream – are used. For the orthorectification process to be as accurate as possible, at least four GCPs are needed, if the imagery is captured perpendicular to the stream, or when the GCPs are placed at the same level as the water level. A minimum amount of six GCPs is needed when the GCPs are not placed in the same plane as the water level. In Figure 2.6 the different gauging site set-ups are shown.

when using four GCPs, the inversion factors f_x and f_y are determined using the formula as stated in Equation 2.9.

$$p_{loc}(x, y) = p_{img}(f_x(x, y), f_y(x, y)) \tag{2.9}$$

where $p_{dst}(x, y, z)$ is the geographic location of the ground control point in the local coordinate system, usually in metric units; $p_{src}(x, y)$ is the xy-coordinate of the ground control point in the imagery, usually in pixels; and f_x and f_y the inversion factors.

Simultaneously with this process, the resolution of the image can be set by multiplying the $GCP_{dst}(x, y)$ coordinates with the desired pixels per meter coefficient. An example of the orthorectification process is shown in Figure 2.7.

When six (or more) GCPs are used – because 3-dimensional coordinates for the GCPs are needed – a pinhole model can be used. This method is explained by Jodeau et al. (2008).

Gray scaling, contrast- and gamma correction

The last step within the image preparation, is the conversion of the imagery to a gray scale, and to apply contrast- and gamma correction. Gray scaling is needed to be able to apply similarity validation between

(a) Original image

(b) Orthorectificated image

Figure 2.7: Example of the orthorectification process using four GCPs, indicated with bamboo poles alongside the stream.

sequential video frames. Contrast- and gamma correction is applied to enhance the visibility of seeds. The contrast- and gamma corrections are applied using the following formulas:

$$O_{contrast} = \alpha \cdot I + \beta \tag{2.10}$$

$$O_{gamma} = \left(\frac{I}{255}\right)^{\frac{1}{\gamma}} \cdot 255 \tag{2.11}$$

where α and β defines the contrast correction; γ the gamma correction; O_n are the corrected imagery; and I is the original imagery.

2.4.2. PIV processing

Figure 2.8 shows the steps of the PIV processing. For two sequential frames, the imagery is divided into grid cells. By determining similarity validation – for example cross-correlation or a signal-to-noise ratio (Osorio-Cano et al., 2013; Ran et al., 2016) – between the two frames within the search area, displacements can be determined. These displacements are then converted into flow velocity vectors.

After applying this process on N frames, a total of $N-1$ velocity maps are created. For each velocity map, the results can be further improved by applying additional filtering based on the similarity value in each single interrogation window, and replacing these filtered values by interpolation the known surrounding grid cells. These post-processing steps are dependent on the software used, or the results required. In Section 4.3.2 the impact of this process is discussed.

After retrieving the flow velocities, data analysis can be applied to acquire time-averaged results. An approach for this process is provided in Chapter 5.

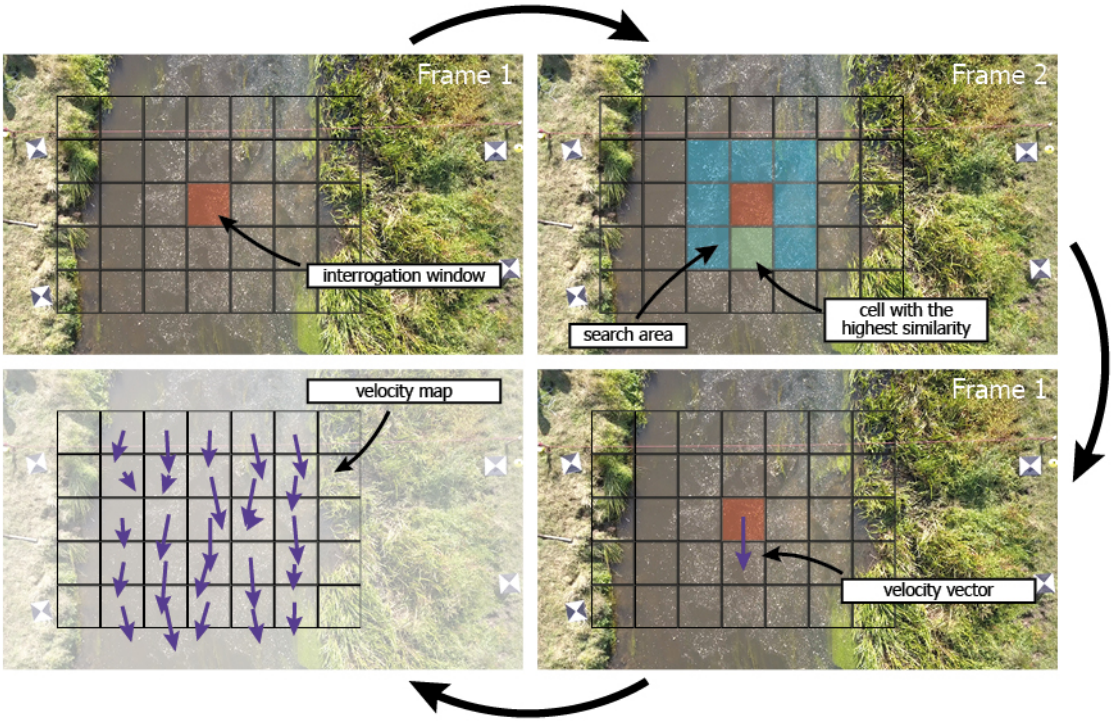

Figure 2.8: Schematic view of the LSPIV method where a interrogation window is determined (the grid is drawn larger dan usually applied) in the first frame and present seeds are compared to a search area in the sequential frame 2 to determine their displacements. By multiplying the displacement with the frame time period, the velocity is determined. When applying this over the whole image, a surface flow velocity map can be created for each individual frame.

3

Study sites

For this research, at two different locations data is gathered to answer the research questions as stated in Chapter 1. These two locations are at the *Dommel*, located in the Netherlands (*see* Section 3.1), and at the *Chuo Kikuu*, located in Dar es Salaam, Tanzania (*see* Section 3.2). This chapter will discuss several characteristics of the study sites and their surrounding.

The imagery and data acquired at the Dommel is used in Chapter 4 to determine the impact of different processing methods and environmental conditions on the accuracy and precision of the LSPIV method. The information from the Chuo Kikuu is processed in Chapters 5 and 6 to determine whether LSPIV can be used to monitor flood waves.

3.1. Dommel

The Dommel is a 120 kilometre long stream located in a *temperate oceanic climate* (Cfb) – following to the Köppen-Geiger climate classification (Beck et al., 2018). In the Netherlands, daytime temperatures varies from 2°C-6°C turing winter and 17°C-20°C in the summer. Precipitation is on average 100 mm/month and roughly evenly distributed over the year.

The Dommel flows through the northern part of Belgium and the south of Netherlands. It is a part of the drainage system of the Muese. The source of the Dommel is at the Kempens Plateau (Belgium), south of Wauberg. It meets the Muese via the Dieze near 's-Hertogenbosch in The Netherlands. Large parts of the Dommel have been canalised over the past century, but there are still parts where the Dommel shows it natural winding course and is able to freely meander. Figure 3.1 shows an impression of two different sites along the Dommel. The average discharge is 14 m³/s, but peaks of 100 m³/s are not uncommon after heavy precipitation events.

In Figure 3.2 the location of the study site is shown. At that point, the slope of the stream is approximately 0.0005 m/m. It flows through a natural area and has the possibility to freely meander.

(a) Dommel upstream Valkenswaard **(b)** Dommel downstream Eindhoven

Figure 3.1: The Dommel at different locations.

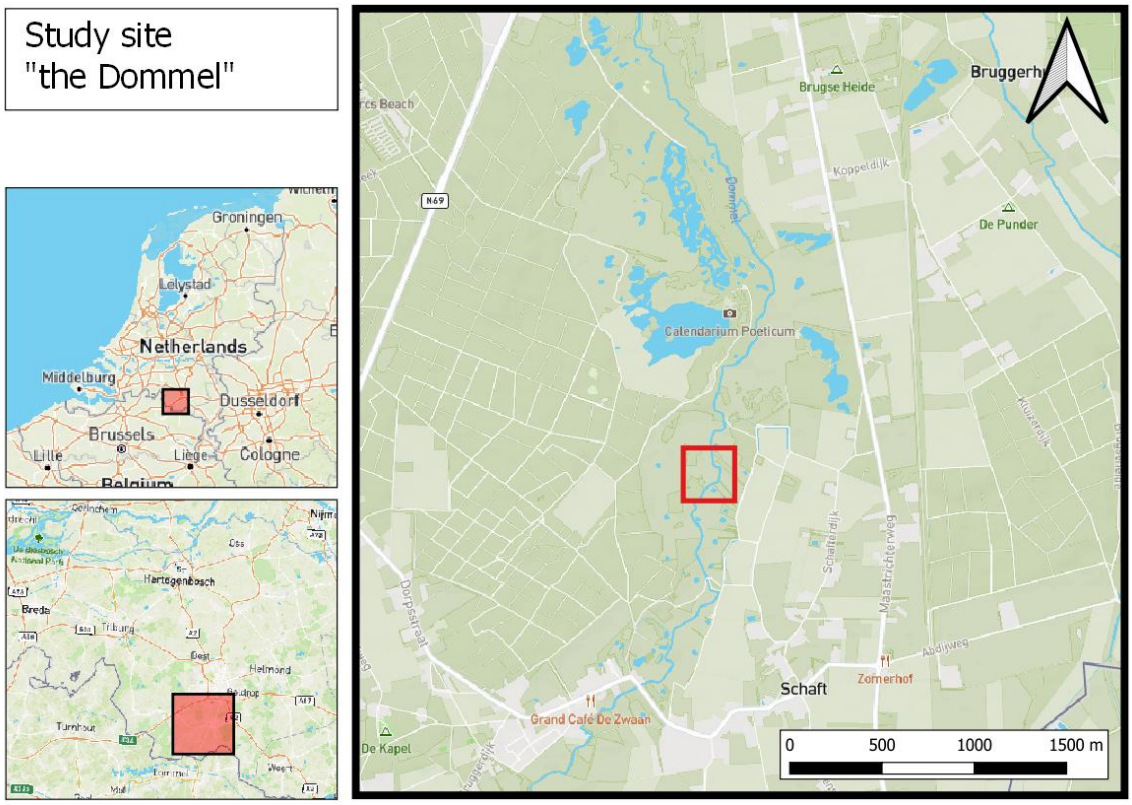

Figure 3.2: Location of the study site at the Dommel, South of Eindhoven, the Netherlands.

3.2. Chuo Kikuu

The Chuo Kikuu is a equatorial small stream in Dar es Salaam, Tanzania. Dar es Salaam – or shortly known as Dar – is located on the Eastern coast and was till 1975 the capital of Tanzania. Currently, it is still the economic centre of Tanzania. Following to the Köpping-Geiger climate classification, the climate in Dar es Salaam is characterised as a *tropical savanna climate* (Aw). Throughout the year temperatures from 28°C-32°C are measured with high humidity levels. Precipitation are clustered within two rain seasons from March-May and November-December. In April – in the middle of the rain season – on average 280 mm precipitation occur. The city experience flood events almost annually due to intense precipitation events (Todd et al., 2019; World Bank, 2019).

(a) Pluvial flooding **(b)** Street in a flood prone area **(c)** Office building of OMDTZ[4]

Figure 3.3: Impressions of Dar es Salaam, Tanzania.

The city has an population of over 6.4 million inhabitants (World Bank, 2019), and a density of 4600 persons/km². In Figure 3.3 several impressions of the city are provided.

The Chuo Kikuu – which means University in Swahili– originates near the University of Dar es Salaam

[4]OpenMapDevelopment Tanzania: Tanzanian NGO promoting community mapping projects.

in the northern part of the city and flows through several densely populated wards toward the Msasani Bay. Throughout the dry seasons, the stream stands mainly dry. During extensive rain events, high discharges occur, causing sudden rises in water level and possible severe flooding. At most parts the stream is canalised or bounded by walls, As can been seen in Figure 3.4.

(a) Stream bounded by walls **(b)** Before a flood wave **(c)** During a flood wave

Figure 3.4: Impressions of the Chuo Kikuu near the study site.

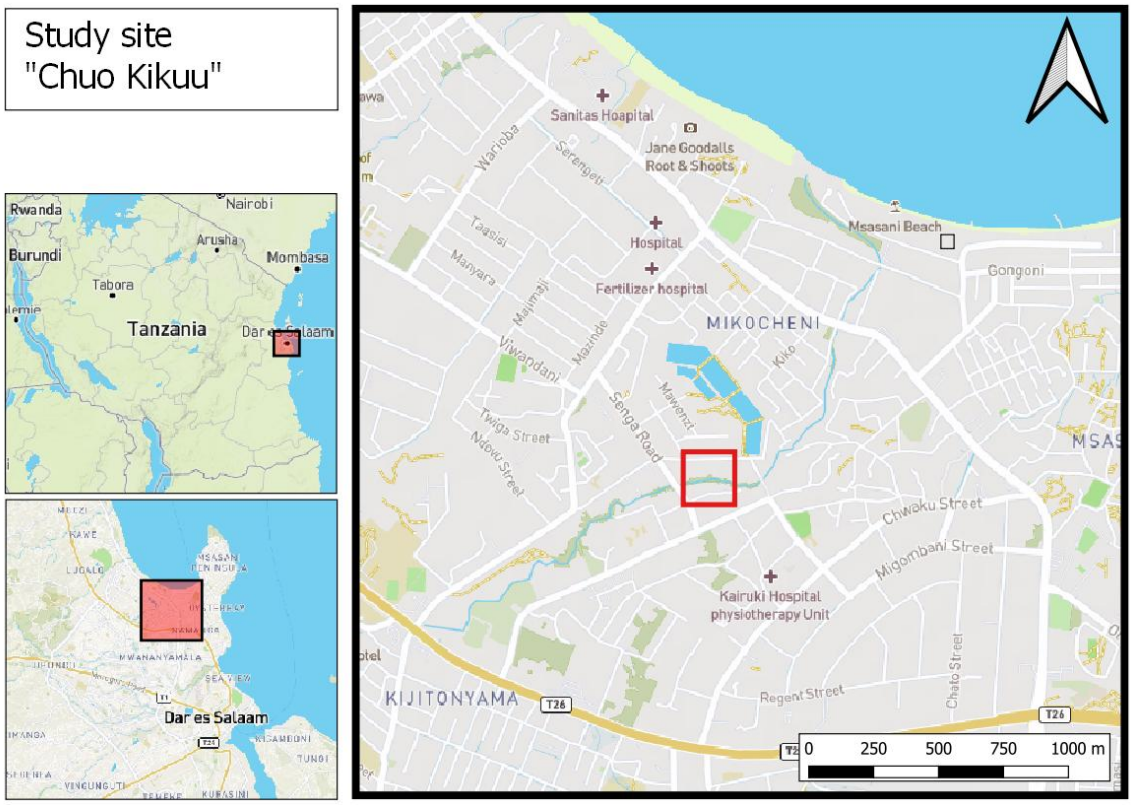

Figure 3.5: Location of the study site at the Chuo Kikuu, Dar es Salaam, Tanzania.

4

Impact processing methods and environmental conditions

This chapter covers the impact of different processing methods and environmental conditions on the accuracy and precision of the LSPIV methods. By discussing different processing methods for acquiring the LSPIV results and monitoring the impact of different environmental conditions on these results, a baseline is provided for the results at the Chuo Kikuu study site.

For all comparisons of the processing methods and environmental conditions, imagery obtained at the Dommel is used and a specific area of interest. The set up of the study site is discussed in Section 4.1. In Section 4.2 the chosen definitions for both the accuracy and precision are further explained. In Section 4.3 a closer look is taken into the impact of different processing methods related to processing software and image manipulation. Thereafter, Section 4.4 treats the impact of the seeding density is examined. In Section 4.5 the impact of the point of view on the stream is investigated related to the accuracy and precision of the LSPIV method. Lastly, in Section 4.6, the results are summarized and some take home messages regarding the following chapter are given.

4.1. Study site set-up

In Figure 4.1 an aerial view of the study site at the Dommel is provided, together with the area of interest for the different experiments. This area is chosen due its close proximity to the location where the benchmark measurements are executed. The choice for this location is also related to the seeding density experiment (*see* Section 4.4). The location provides the best distributions for all different seeding density conditions. Clearly visible in Figure 4.1a are the aquatic plants at the bottom of the Dommel. As it is expected that these plants – due to their visibility and movements – will lead to additional noise after the PIV processing, as many plants as possible were removed from the area of interest prior to the measurements.

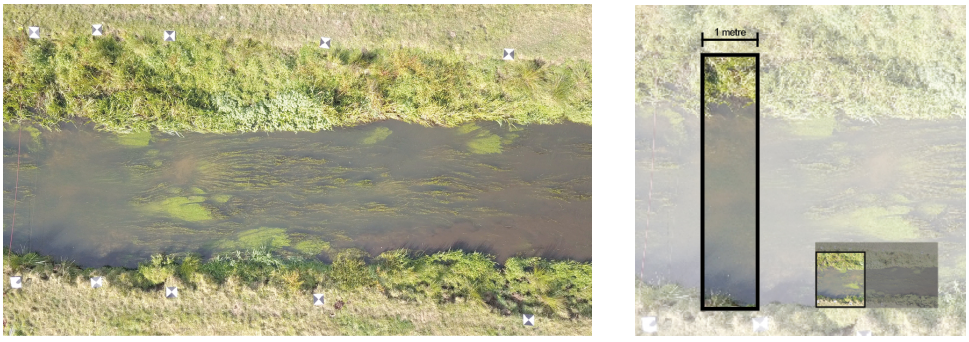

(a) Aerial view of the Dommel **(b)** Area of interest

Figure 4.1: Area of interest of the Dommel used for the processing methods and environmental conditions comparisons.

The benchmark measurements are gathered by measuring the flow velocities just below the water surface – using a OTT current meter – for every 0.5 metre stream width. By combining these eleven consecutive measurements, a median flow velocity of 0.337 m/s is found. The 25th and 75th percentiles are 0.295 and 0.353 m/s, respectively.

Along the site, several GCPs are placed. For the orthorectification method the outer four GCPs are used, under the assumption that the vertical distance between the water level and the GCPs is negligible. These GCPs are surveyed using RTK GPS equipment: using a local reference station – which had the opportunity to pin-point its location for several hours and is used to adjust for shifting errors – and a rover.

The videos are obtained using a drone – a DJI Mavic Pro – equipped with a FC220 camera which automatically corrects for the lens distortion. Each video is trimmed to a timespan of approximately 30 seconds. As the videos are shot with a frame rate of 24 frames per second, every video consist therefore of a imagery sequence of 718 till 720 frames. Due to hovering, stabilisation was removed as much as possible. However, as the UAV movements took place in three directions, full stabilisation could not be achieved, which mainly influences the imagery captured with an incline. Using the GCPs orthorectification is applied. During this process, the frame resolutions are set to 0.01 metre per pixel. In order to determine the flow velocities using LSPIV, 60 x 60 centimetre grid cells with a 30 pixel overlap are used, these are the interrogation windows. The location of the flow velocity is then set to the centre of each grid cell.

4.2. Definitions of accuracy and precision

As aforementioned, in order to quantify the impact of the different processing methods and environmental conditions, both the accuracy and precision of the LSPIV results are determined. The accuracy (*see* Box 4.1) is determined by comparing the results obtained following the LSPIV method with the flow velocities measured using a OTT current meter.

Box 4.1: Definition of accuracy

Accuracy is *the degree to which the result of a measurement, calculation, or specification conforms to the correct value* (Oxford University Press, 1989a). For this research, this is defined as the agreement of surface flow velocities obtained using LSPIV and a benchmark value, which is retrieved using an OTT current meter.

For quantifying the accuracy, two types of errors are determined: (1) the mean error (ME), which shows whether the LSPIV generally result in either larger or smaller values than the benchmark values, and (2) the root mean squared error (RMSE), which is the standard deviation of the differences between the results obtained with the LSPIV method and the benchmark value. The ME and RMSE are defined as follows:

$$ME = \frac{1}{N}\sum_{i=0}^{N} \mu_{v,0} - \mu_{v,LSPIV,i} \tag{4.1}$$

$$RMSE = \sqrt{\frac{1}{N}\sum_{i=0}^{N} (\mu_{v,0} - \mu_{v,LSPIV,i})^2} \tag{4.2}$$

where N is the number of points found in space in the LSPIV result; $\mu_{v,0}$ the benchmark median flow velocity obtained using a OTT current meter; and $\mu_{v,LSPIV,i}$ the median flow velocity over time at a specific point in space, obtained using LSPIV.

The precision (*see* Box 4.2) is determined using the median relative standard deviation. When obtaining a high median relative standard deviation (RSD), there is a wide range of different values, meaning there is a low precision. Vice versa, when finding a low median RSD, there is a high precision.

Box 4.2: Definition of precision

Precision is defined as *the refinement in a measurement as represented by the number of digits given* (Oxford University Press, 1989b). In this research, precision is characterized as the ambiguousness of flow velocities obtained using LSPIV by means of the relative standard deviation (RSD). A higher RSD means a lower precision. The RSD is obtained using the following formula:

$$RSD_i = \frac{\sigma_{v,LSPIV,i}}{\mu_{v,LSPIV,i}} \tag{4.3}$$

where $\sigma_{v,LSPIV,i}$ is the standard deviation of the flow velocity in time at a point in space; and $\mu_{v,LSPIV,i}$ the median flow velocity over time at the same point in space.

4.3. Impact processing methods

Related to the processing method, there are two components taken into consideration which could influence the velocities found with the LSPIV approach. These two elements are (1) the processing software, and (2) the image manipulation, as explained in Section 2.4. In order to determine the impact of both elements on the LSPIV results, they are applied on either two or three different videos.

The first video (*see* Figure 4.2a) does not contain any artificial seeding and results obtained using LSPIV are fully dependent on the presence and visibility of leaves, branches, air bubbles, and other traceable items that occur ordinarily in the river. The second video contains limited artificial seeding (*see* Figure 4.2b) in the form of small wooden blocks. The seeding densities are , respectively The third video extensive artificial seeding (*see* Figure 4.2c) in the form of saw dust. It is remarked that this section covers solely the impact of the processing method. The comparison between the different seeding densities will be discussed in Section 4.4.

(a) No artificial seeding (~3 particles/m²)

(b) Limited artificial seeding by adding small brown wooden blocks (~50 particles/m²)

(c) Extensive artificial seeding by adding white saw dust (~500 particles/m²)

Figure 4.2: Frame captures sections of the different field tests in the Dommel using (a) no, (b) limited, and (c) extensive artificial seeding. Different seeding densities are used to examine the impact of seeding density on the precision of the LSPIV results.

4.3.1. Types of processing software and image manipulation

Within literature, there are several software programs used for processing videos and extracting surface flow velocities and determining river discharges based on LSPIV, e.g. Fudaa-LSPIV (Le Coz et al., 2014), PIVlab (Thielicke and Stamhuis, 2014), RIVeR (Patalano et al., 2017) – which is based on PIVlab – and OpenPIV (Taylor et al., 2010). In this research, the software used is OpenPIV. The main reasons for this choice are (1) the relatively fast processing time, (2) the software is open source, and (3) the LSPIV steps are divided into different functions, which makes it easy to adapt for different cases.

(a) Original Fudaa-LSPIV output **(b)** Contrast correction option I **(c)** Contrast correction option II

Figure 4.3: Sections of the first frames of the different image manipulation methods for the extensive artificial seeding density option, where (a) shows a part of the output as generated using Fudaa-LSPIV. Both (b) and (c) use the original frame as input but different contrast correction parameters are applied.

In order to justify the use of OpenPIV, the outcomes are compared with the results of Fudaa-LSPIV, which is also an open source based software and within literature widely used (e.g., Benacchio et al., 2017; Dramais et al., 2011; Lewis et al., 2018; Theule et al., 2018; Zhu and Lipeme Kouyi, 2019). However, Fudaa-LSPIV has a long processing time compared with OpenPIV, and operates like a *black box* due to its interface.

Besides the processing software, an element with expected significant influence on the results is the image manipulation. Therefore, different types of image manipulations are compared. Using Fudaa-LSPIV, the major part of the image manipulation is carried out (*see* Section 2.4.1). This involves video stabilisation, gray scaling and orthorectification. The images resulting from this process will be referred to as the *Original* output. After this, using OpenCV the contrast of the *Original* images are adjusted in two different ways. The prospect is, by increasing the contrast, the processing software can identify seeds more easily and therefore both the accuracy and precision would improve. The parameters of both adjustments – *Contrast I* and *Contrast II* – are provided in Table 4.1. All types of image styles – as shown in Figure 4.3 – are then processed using OpenPIV and compared with the original output of Fudaa-LSPIV.

Table 4.1: Contrast- and gamma correction parameters for the two different imagery *Contrast I* and *Contrast II*

	α	β	γ
Contrast I	8	-850	0.4
Contrast II	4	-350	0.4

In order to determine the impact of the different types of processing software and image manipulation, the following four parts will be treated. The first part elaborates the data processing in OpenPIV and the differences in its output (*see* Section 4.3.2). The second part covers the output differences between OpenPIV and Fudaa-LSPIV on a single grid cell level (*see* Section 4.3.3). The third part discusses the impact of choice for different percentiles in temporal flow velocities (*see* Section 4.3.4). Lastly, in Section 4.3.5 the impact of the different processing software and image manipulation methods on the accuracy and precision is discussed.

4.3.2. Choosing the OpenPIV output

Within OpenPIV, there are three major steps which result into the commonly used output. These steps are illustrated in Figure 4.4. The first step leads to the *raw* results, where for every grid cell the x and y flow velocity component is given, together with signal-to-noise ratio – the outcome of the similarity validation. The second step removes cell values based on the signal-to-noise ratio and replaces them by NaN. This output is hereafter named the *filtered* results. During the last step, the removed values are filled in by interpolating the surrounding known grid cell values and is named the *interpolated* results.

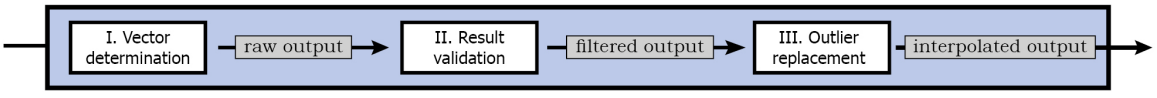

Figure 4.4: Simplified flow diagram of the processing methodology used by OpenPIV showing the three major steps leading to the generally used output.

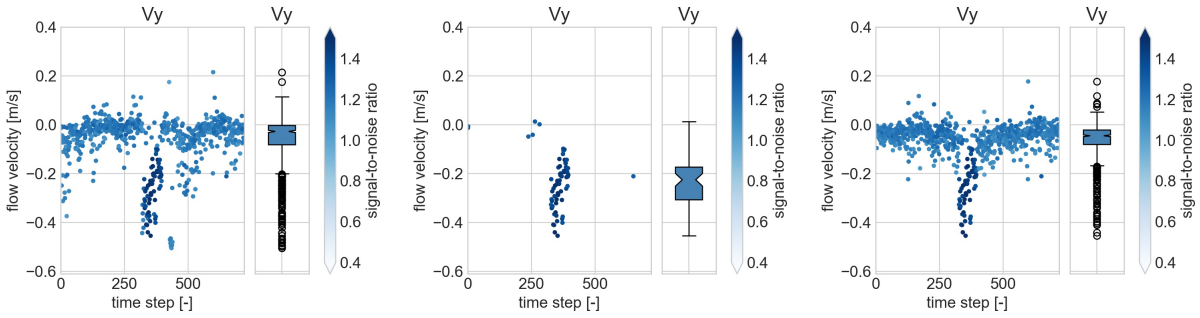

(a) *Raw* results **(b)** *Filtered* results **(c)** *Interpolated* results

Figure 4.5: Example of flow velocities in the y direction in time at a single grid cell obtained using OpenPIV. The process consists of three steps. First, (a) the *raw* results. Secondly, (b) the *filtered* results based on the signal-to-noise ratio (OpenPIV) or cross-correlation (Fudaa-LSPIV). And thirdly, (c) the *interpolated* results where the velocities which are filtered in the previous step are interpolated using surrounding grid cells at the same time step. The shade of blue indicates the level of noise.

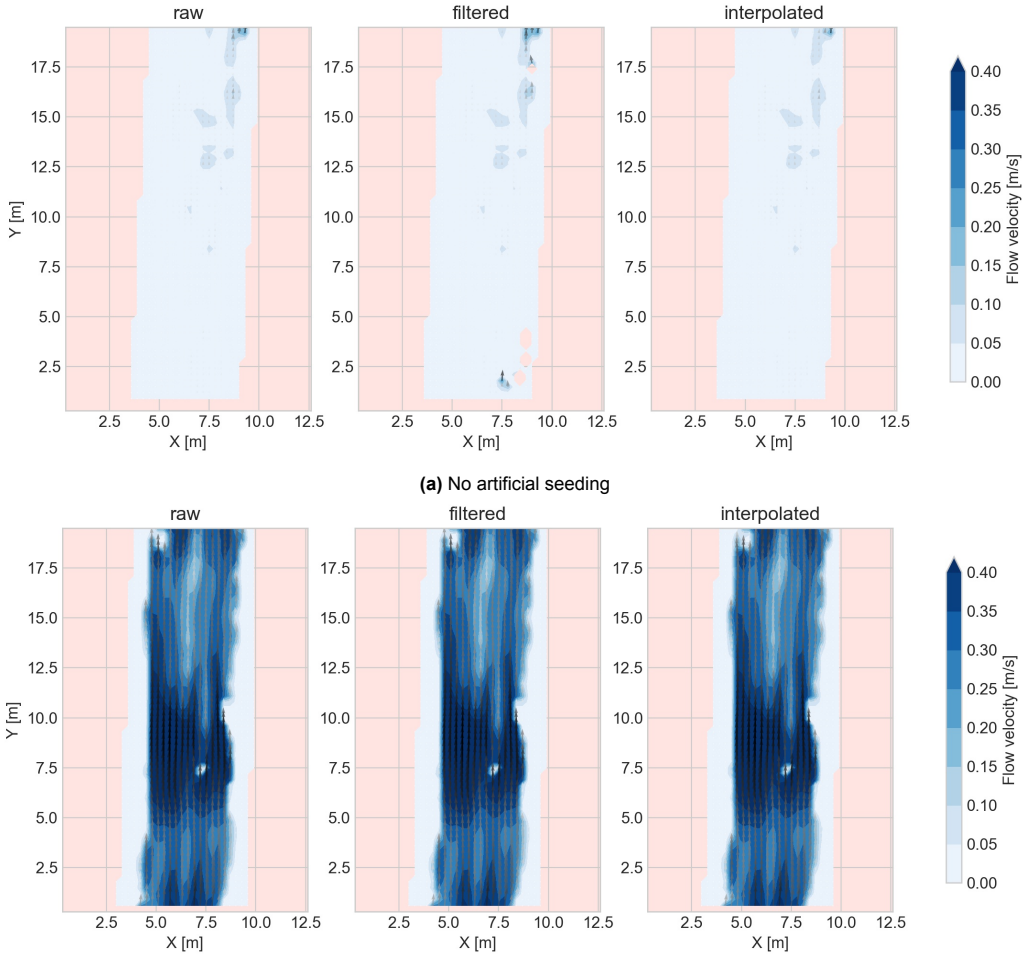

(a) No artificial seeding

(b) Extensive artificial seeding

Figure 4.6: Average surface flow velocities and directions obtained using OpenPIV at the *raw*, *filtered*, and *interpolated* point of the process for both (a) no artificial seeding and (b) extensive artificial seeding.

Using the *no artificial seeding* video, the impact of the processing steps at a single grid cell level is visualised in Figure 4.5. The *raw* results (*see* Figure 4.5a) show the flow velocities in the y-direction – this is the upward direction in Figure 4.3 – plotted against the frame step, together with the distribution visualised using a boxplot. The shade of blue for every point indicates the strength of the signal-to-noise ratio. Around time step 350, the flow velocity increases as a seed is detected. Mainly during this moment higher signal-to-noise ratios are found. The second step – named *filtered* (*see* Figure 4.5b) – shows the results at the same grid cell, but all points with a signal-to-noise ratio lower than 1.3 are excluded from the results. Lastly, the missing dots are *interpolated* using the values of surrounding grid cells at the same time step (*see* Figure 4.5c). This last step is especially useful when there are seeds detected in the surrounding grid cells.

For this single grid cell, the absolute median flow velocity obtained using the OpenPIV goes from 0.034 m/s for the *raw* results, to 0.25 m/s for the *filtered* results, ending into 0.051 m/s for the *interpolated results*. At the location, the benchmark flow velocity, obtained using an OTT current meter, was approximately 0.33 m/s. The results of the *filtered* step, gives therefore the outcome closest to the benchmark value.

For both the *no artificial seeding* and *extensive artificial seeding* sequences, Figure 4.6 illustrates the median flow velocities obtained using OpenPIV at the different processing steps over the whole video. At first sight, the impact of the *filtering* process is visible for the *no artificial seeding* video (*see* Figure 4.6a). At multiple points, higher flow velocities are noticeable. However, also grid cells containing no results at all are distinguishable. Based on the acquired results, two points are further elaborated: (1) the accuracy of the obtained flow velocities, and (2) the precision of the flow velocities.

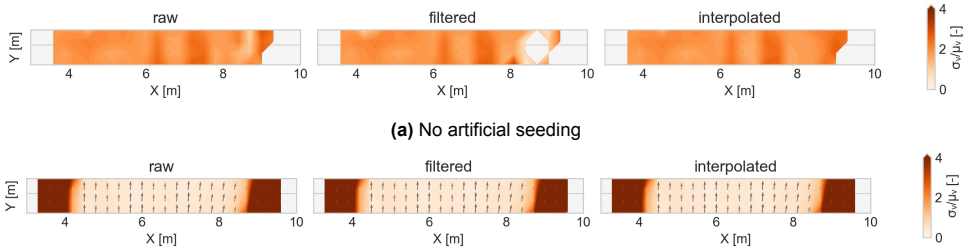

(a) No artificial seeding

(b) Extensive artificial seeding

Figure 4.7: RSD heatmap for no artificial seeding. for both (a) no artificial seeding and (b) extensive artificial seeding.

Figure 4.7a presents for the area of interest of the *no artificial seeding* video the intensity of the RSD values for the three different OpenPIV steps. Figure 4.8b presents this as a distribution. It is clear that the *filtered* results shift towards the $\sigma/\mu = 1$ line – all points below this line, have a higher median value than its standard deviation. Figure 4.8a contains the distribution for the median flow velocities. For each different step output, the results obtained using the OpenPIV underestimates the flow velocities as obtained with an OTT current meter. As could be expected from Figure 4.5, the *filtered* output returns more grid cells with higher flow velocities. However, the number of grid cells containing flow velocities ranging from 0 to 0.02 m/s stays about the same.

Figure 4.9 contains distributions for both the median flow velocities as the relative standard deviations for the *extensive artificial seeding* frame sequence. For this high amount of seeding density, there is no clear distinction between the different processing steps recognisable for both the accuracy as the precision. Using either of these outputs will therefore barely alter the found flow velocities. For low seeding densities, it is recommendable to use the *filtered* output instead of the default *interpolated* results.

4.3.3. OpenPIV and Fudaa-LSPIV rasterisation differences

For both image sequences, Figure 4.10 presents the average flow velocities using both Fudaa-LSPIV and OpenPIV on the complete frame. The figure is a visualisation of the average flow velocities of all 720 frames at a certain grid point.

Before discussing the accuracy and precision of the obtained flow velocities, it is noteworthy that there is an anomaly between the results obtained using Fudaa-LSPIV and OpenPIV caused by rasterisation.

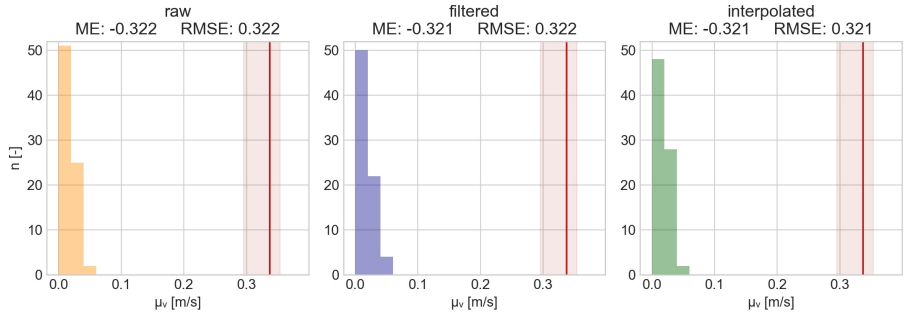

(a) Distribution flow velocities for no artificial seeding. In red, the median benchmark flow velocity is accentuated, together with the 25th and 75th percentile.

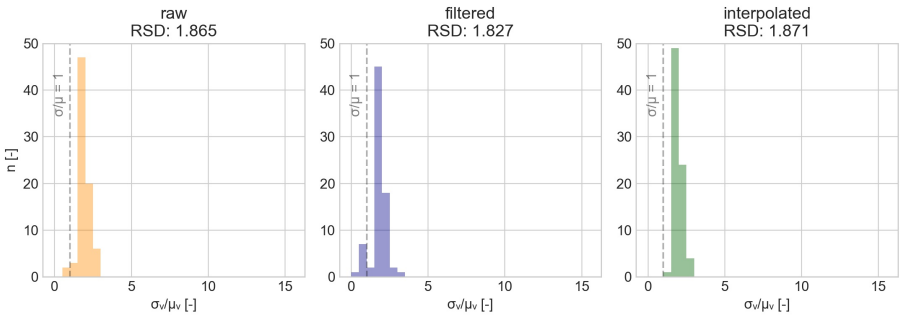

(b) Distribution RSD values for no artificial seeding. The vertical dashed line states the point where both the standard deviation as the median values are equal.

Figure 4.8: Distributions for both (a) the median flow velocities and corresponding ME and RSME values and (b) the relative standard deviation and corresponding median RSD value for the *no artificial seeding* imagery using different OpenPIV step outputs.

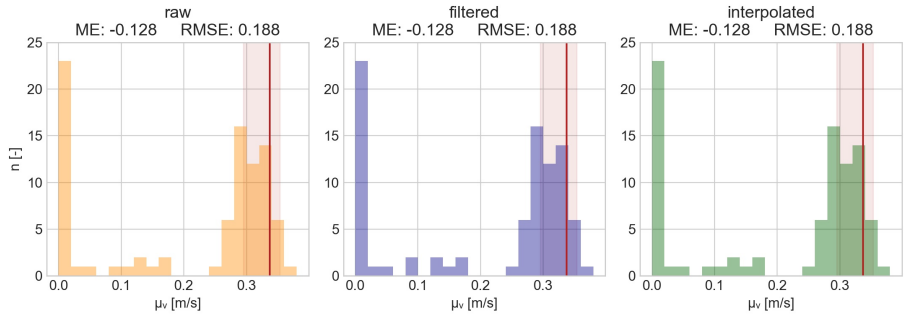

(a) Distribution flow velocities for extensive artificial seeding. In red, the median benchmark flow velocity is accentuated, together with the 25th and 75th percentile.

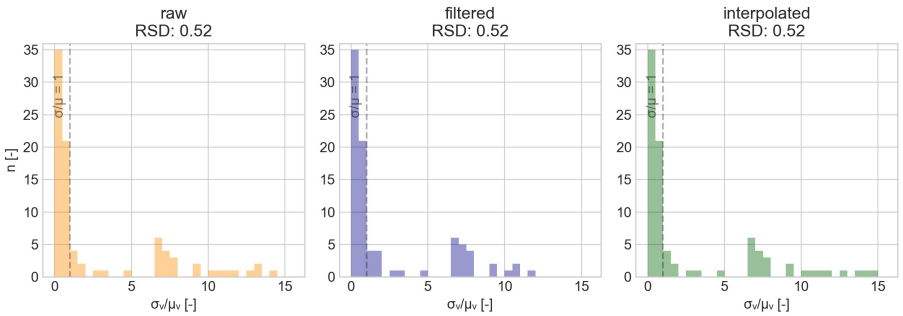

(b) Distribution RSD values for extensive artificial seeding. The vertical dashed line states the point where both the standard deviation as the median values are equal.

Figure 4.9: Distributions for both (a) the median flow velocities and corresponding ME and RSME values and (b) the relative standard deviation and corresponding median RSD value for the *extensice artificial seeding* imagery using different OpenPIV steps outputs.

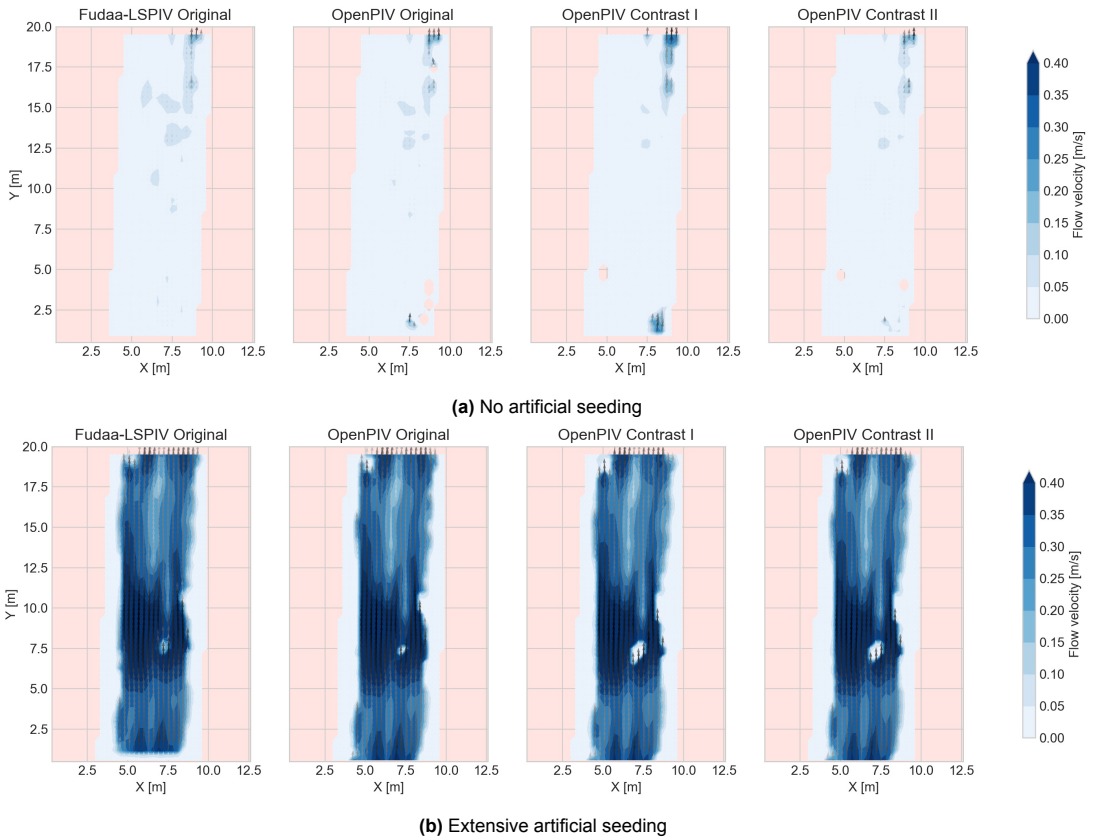

(a) No artificial seeding

(b) Extensive artificial seeding

Figure 4.10: Average surface flow velocities and directions following the LSPIV method obtained using Fudaa-LSPIV and OpenPIV for both (a) no, and (b) extensive artificial seeding using different image manipulation approaches.

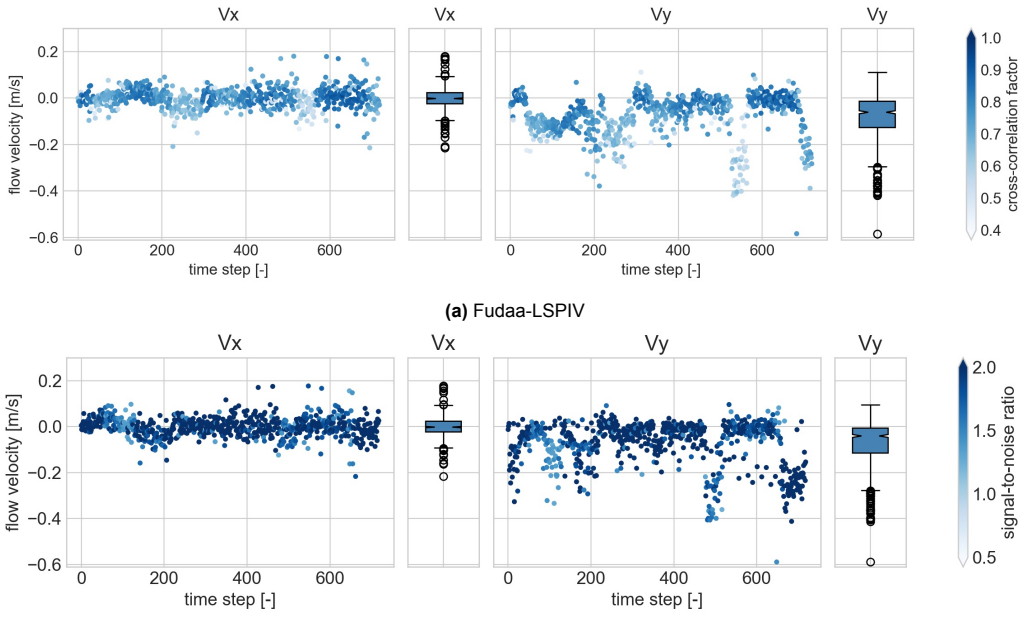

(a) Fudaa-LSPIV

(b) OpenPIV

Figure 4.11: Flow velocities in the x and y direction at a single grid cell obtained using (a) Fudaa-LSPIV and (b) OpenPIV for the no artificial seeding example. Due to rastification, peaks in measured flow velocities can be seen in different places or not seen at all. The shades of blue indicate the level of noise of individual points according to the processing software.

In order to compare the results of both software, the output obtained using Fudaa-LSPIV is rasterized to the grid as obtained using OpenPIV. When converting the Fudaa-LSPIV raster to the OpenPIV raster, the flow velocity origins – which are in the centre of each grid cell – can move up to 20 centimetres. This point is visualised in Figure 4.11. This can either cause a delay for when a seed is observed, or a seed might not be observed in that grid cell at all. For example, around time step 540 a peak in flow velocities in the y-direction is detected by the Fudaa-LSPIV approach (*see* Figure 4.11a), while this same peak is detected at time step 490 using OpenPIV (*see* Figure 4.11b).

4.3.4. Ranges in flow velocities

In this chapter, all comparisons – between the different processing methods and between different environmental conditions – are made using the median flow velocities of each single grid cell. However, as was already illustrated in Figure 4.5, after the software processing a range of data points – equal to the total number of frames – is found for each single grid cell. Due to this, not choosing the median – or 50th percentile – flow velocity, but a higher percentile instead, might improve the accuracy of the method. Therefore, a closer look is taken into the impact of choosing different percentile values.

Figure 4.12 presents for the three different seeding densities[5] – as provided in Figure 4.2 – the temporal variability of the flow velocities within the area of interest over the width. As expected, a wide range in flow velocities can be observed.

For all seeding densities, the median flow velocities underestimate the expected values. When increasing the percentiles used for the grid cell specific flow velocities, the flow velocities start to get closer to the benchmark flow velocities, as can be observed in Figure 4.13. Especially for *no artificial seeding*, flow velocities ranging between 0.2-0.3 m/s start to be noticed when using the 95th percentile. For *limited* and *extensive artificial seeding* the 95th percentile start to overestimate the benchmark values. For these seeding densities the 75th percentile comes closer to the correct flow velocities.

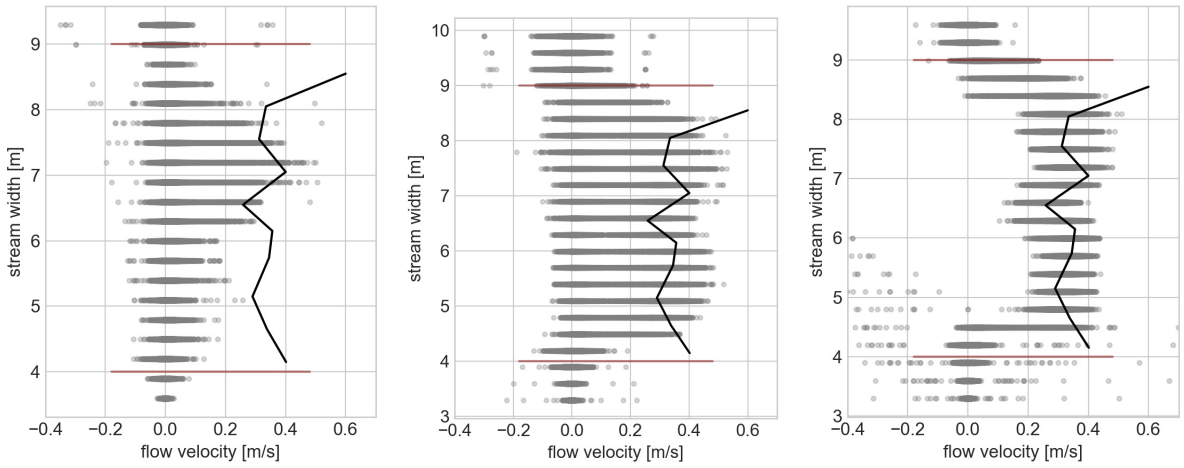

(a) *No artificial seeding* **(b)** *Limited artificial seeding* **(c)** *Extensive artificial seeding*

Figure 4.12: Distributions of flow velocities over the width of the area of interest for (a) no artificial seeding, (b) limited artificial seeding, (c) extensive artificial seeding, together with the river banks and flow velocities as gathered with a current meter, measured just below the water surface.

4.3.5. Results

Regarding the accuracy (*see* Box 4.1), Figure 4.14 contains the results for both image sequences with different seeding densities, which includes parts of the riverbanks. The plots show the absolute density of the median values found in the area of interest, together with the median bechmark flow velocities and the corresponding 25th and 75th percentile band width.

For both seeding densities, there is no clear distinction in both ME and RMSE values between neither the results from different processing software, and from by the different image manipulation methods. When

[5]The differences in accuracy and precision between the three types of seeding density are discussed in Section 4.4.

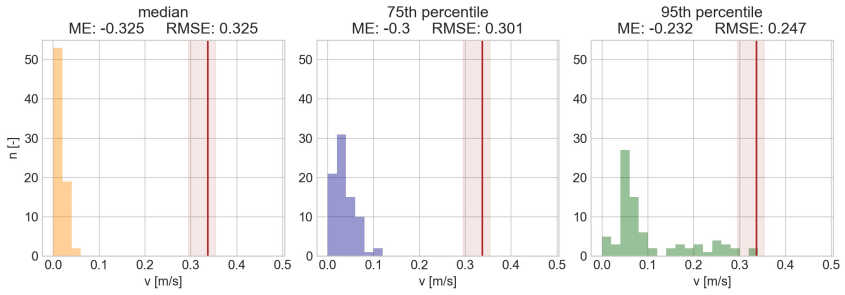

(a) *No artificial seeding* results

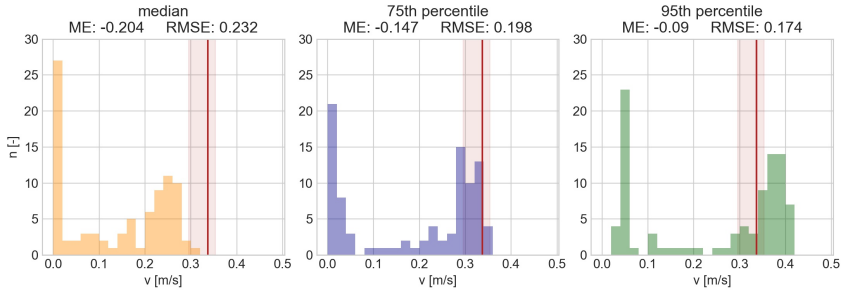

(b) *Limited artificial seeding* results

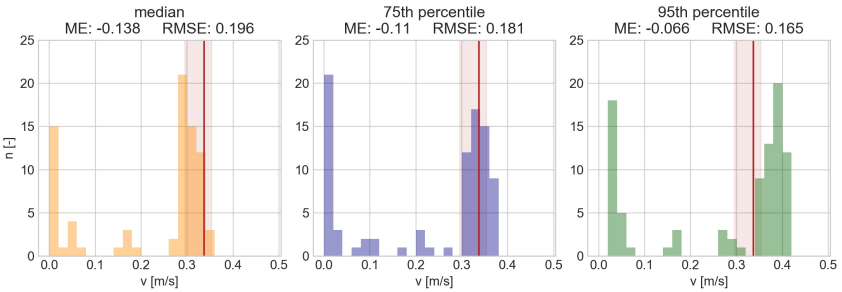

(c) *Extensive artificial seeding* results

Figure 4.13: Distributions of the mean flow velocities over the width of the area of interest for (a) no artificial seeding, (b) limited artificial seeding, (c) extensive artificial seeding, together with the benchmark flow velocities, measured just below the water surface.

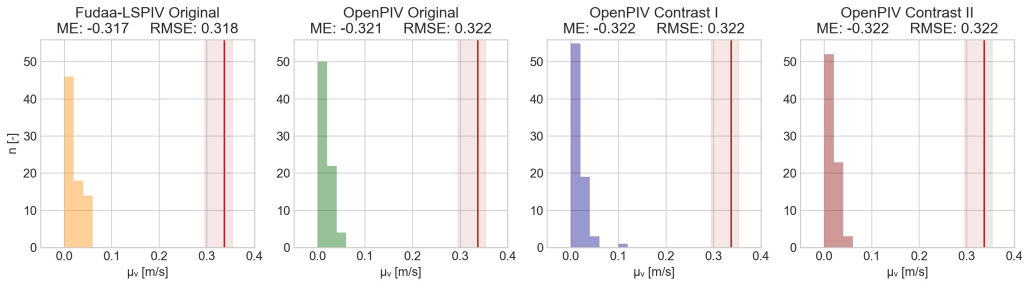

(a) No artificial seeding

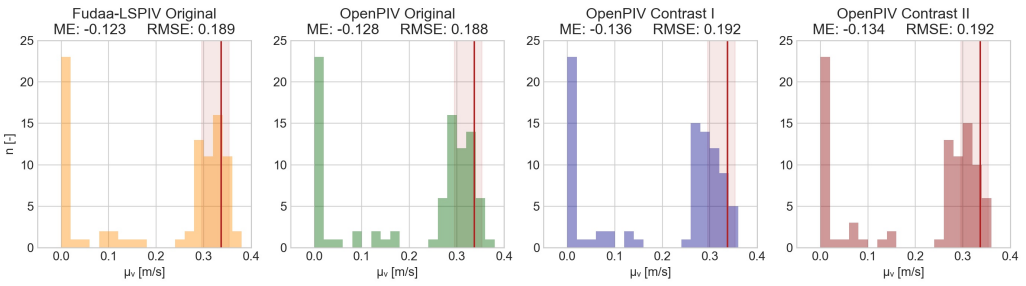

(b) Extensive artificial seeding

Figure 4.14: MEs, RMSEs and distributions for the median flow velocities found in the area of interest using different processing software and image manipulation approaches for both (a) *no*, and (b) *extensive seeding*. Also, the benchmark median velocity for the whole river width is given, together with its 25th and 75th percentiles.

looking at the differences between the *Original* imagery results, the results obtained using Fudaa-LSPIV tend to be closer to the benchmark value, than the flow velocities obtained using OpenPIV. Especially when focussing on the extensive artificial seeding imagery, this can be noticed.

Also, the impact of applying contrast corrections on top of gray scaling seems to be limited. As can be seen in Figure 4.14a, image manipulation method *Contrast I* makes it at limited locations possible to detect more seeds, and therefore accumulate higher flow velocities. However, this effect is not noticeable when applying the same contrast correction on the video with extensive artificial seeding applied (*see* Figure 4.14b). It even results in lower flow velocities at certain locations. However, the absolute differences are small.

The precision (*see* Box 4.2) of the data sets are shown in Figure 4.15 for both seeding densities, processing software, and all image manipulation methods. The bars within the figure represents the number of grid cell values falling within the range provided. The $\sigma/\mu = 1$ line is indicated by a vertical dashed line. All values occurring before this line have a standard deviation which is smaller than the median flow velocity. Moreover, heatmaps of the RSD values are given.

As was the case with the accuracy results, the results for the precision do not differ much from each other, when focussing on the processing software and image manipulation method. For both seeding densities, the RSD values lay close to each other, without anything remarkable standing out. The results obtained from the imagery with additional contrast correction seem to reduce the precision in a small quantity. Therefore, only applying gray-scaling is adequate to achieve reasonable results.

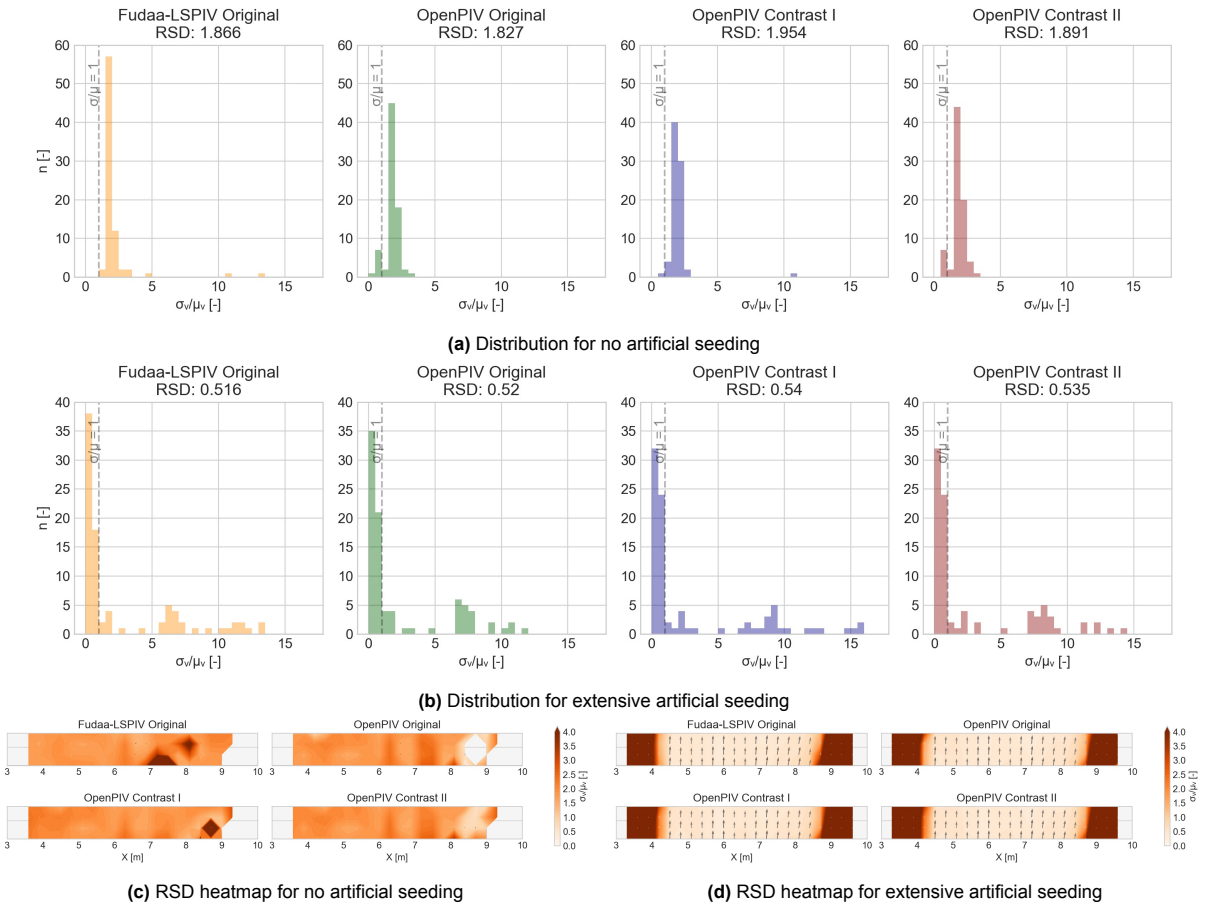

(a) Distribution for no artificial seeding

(b) Distribution for extensive artificial seeding

(c) RSD heatmap for no artificial seeding

(d) RSD heatmap for extensive artificial seeding

Figure 4.15: Distributions, median relative standard deviations (RSD) values and heatmaps for the RSD using different processing software and image manipulation approaches for both (a) no, and (b) extensive seeding. With a vertical dashed line stating the point where both the standard deviation as the median values are equal.

4.4. Impact seeding density

As is stated in most literature regarding LSPIV, one of the main elements influencing its results is the seeding density (e.g., Eltner et al., 2019; Kantoush et al., 2011; Kim, 2006; Le Coz et al., 2014; Muste et al., 2008, 2010). As stated by among others Kantoush et al. (2011), seeding particles must be large enough to be visible, but small and light enough to track the flow velocities as accurately as possible. Besides this, at least one or two seeding particles have to be present within an interrogation window to be able to quantify the flow velocity. If existing, natural seeds like debris, leaves, air bubbles and wave patterns can be used to quantify the flow velocities. However, if only a limited number of natural seeds are present, artificial seeding could be applied. Kantoush et al. (2011) summarized many laboratory tests and found offsets till 10% when applying different forms of limited and extensive seeding.

4.4.1. Seeding density conditions

To determine the impact of seeding density on the accuracy and precision of the surface flow velocities, image sequences with three different states of seeding densities are gathered. These seeding densities are either caused by natural seeds – like leaves and small twigs – or by artificial seeds – such as saw dust and wooden blocks. The imagery is shot perpendicular to the river (*see* Figure 4.2).

The first state (*see* Figure 4.2a) does not contain any additional artificial seeding. Results obtained using LSPIV completely depend on the presence of natural seeds. In the river Dommel a small amount of natural seeds can be identified, which are mainly small leaves and branches. Figure 4.2b presents the second state of seeding: *limited artificial seeding*. Using brown wooden chips. The chips cover most of the river width and the spacing between the chips is in the order of centimetres. Lastly, Figure 4.2c contains a frame section of the *extensive seeding density* state, achieved by adding white saw dust upstream of the river. The distance between the different particles is in magnitudes of millimetres.

4.4.2. Results

Figure 4.16 presents the results obtained by applying LSPIV on the three different seeding density states as aforementioned. In Figure 4.16a the median flow velocities in time over the whole imagery, together with the RSD values (*see* Box 4.2) within the area of interest is visualised. Due to the limited length of the video, for the *Limited artificial seeding* state, only a part of the river length was covered by seeds. This area falls within the area of interest.

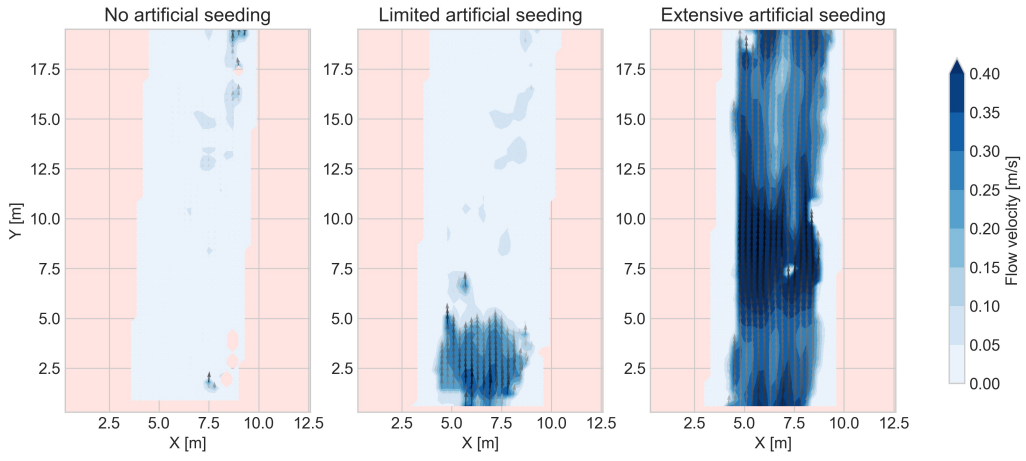

(a) flow velocities complete image

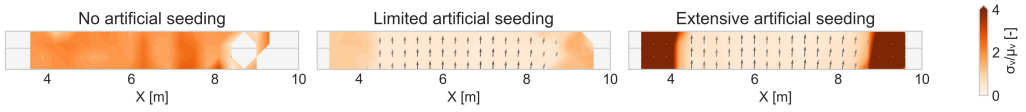

(b) Relative standard deviation area of interest

Figure 4.16: Flow velocities and relative standard deviation heatmaps for different seeding densities.

As can be seen in Figure 4.16a, the *No artificial seeding* state does barely show any results related to the median flow velocities observed. This despite the presence of natural seeds which are noticeable with the eye. It could be possible to detect these seeds by decreasing the interrogation windows. However, this substantially increases the computation time of the processing software.

Figure 4.17 presents the distributions of both the median flow velocities and the relative standard deviations in the area of interest, together with the ME, RSME and median RSD values (*see* Boxes 4.1 *and* 4.2) for the definitions and calculation method). As can be expected, the flow velocities obtained with the *Extensive artificial seeding* density come closest to the benchmark median flow velocity. Despite having the same amount of high flow velocities, the flow velocities obtained using *Limited artificial seeding* tend to be lower. This could be caused by the weight of the wood chips – the wood chips are heavier than the saw dust and could therefore flow slower than the actual flow velocity.

For both *Limited artificial seeding* and *Extensive artificial seeding*, the precision of the flow velocities is high within the river banks. However, the results on the river banks differ quite a lot. This can be caused by the hovering of the drone, which could be higher for the video with *Extensive artificial seeding*. The *No artificial seeding* state, has a overall higher RSD as the measured flow velocities are in general higher and therefore, the standard deviation has a bigger impact on the RSD results. Because of this, the median RSD for *Extensive artificial seeding* is higher than expected.

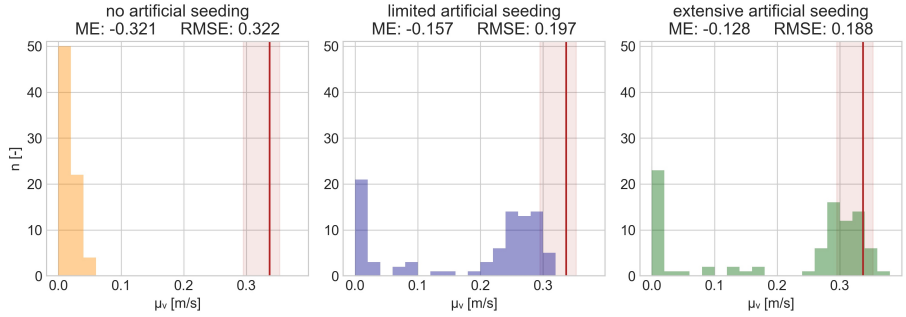

(a) Median flow velocities

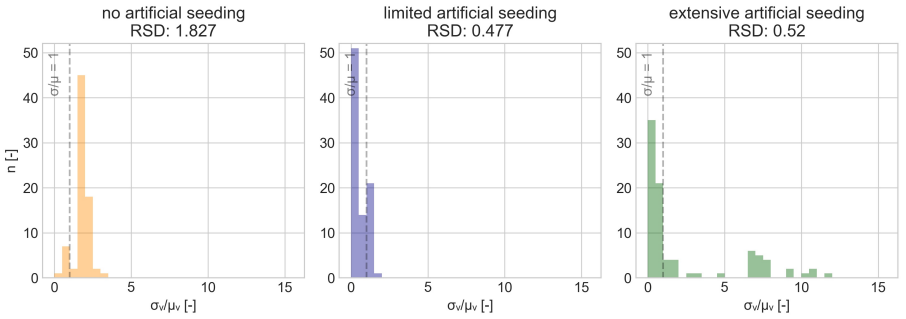

(b) Relative standard deviation

Figure 4.17: Distributions for the median flow velocities and relative standard deviation section for different seeding densities.

4.5. Impact point of view

The most ideal location to place a camera, for gathering imagery from a river for LSPIV purposes, is perpendicular to the river. In most cases this is achieved by attaching a camera to a bridge (e.g., Tauro et al., 2017, 2016a) or with use of a drone (e.g., Lewis et al., 2018; Tauro et al., 2016b). This way, influences by perspective and relief effects are limited. However, the majority of gauging sites depends on observations from an angle by placing a camera on the river bank or attaching it to a nearby building (e.g., Aya et al., 1995; Bradley et al., 2002; Dramais et al., 2011; Fujita and Komura, 1994; Hauet et al., 2008; Le Coz et al., 2010; Muste et al., 2010). In order to use these angled imagery, orthorectification has to be applied (*see* Section 2.4.1), to remove the impact of perspective and create an image which is *planimetric*. It is expected that orthorectification has an effect on the results of the LSPIV method, as seeds might get deformed by this process (e.g., Fujita et al., 1998; Kim, 2006). Kim (2006) found the erroneous vectors increase significantly when exceeding the 5°mark, related to the horizontal plane.

(a) Angle I, facing East **(b)** Perpendicular view **(c)** Angle II, facing West

Figure 4.18: Frame captures sections of the different field tests in the Dommel using different points of view.

However, in other positions, the impact of the camera angle should not be significant, neglecting the impact of lightning.

4.5.1. Different angle cases

To determine the impact of the point of view, and thereby the orthorectification process, on the accuracy and precision, two groups of cases are discussed. The first case group is a comparison between a perpendicular captured video and a video facing East (*see* Figure 4.18a). This first case group does not contain any artificial seeding and the presence of seeds solely depends on natural seeding like leaves and air bubbles. The second case group is a comparison between a perpendicular captured video (*see* Figure 4.18b) and a video facing West (*see* Figure 4.18c). At the time the videos of this second case group was captured, a limited amount of seeds was added to the stream. During both angled view captures, the camera is under an angle of approximately 20°relative to the horizontal plane.

For both cases the median flow velocities and corresponding relative standard deviations are determined, whereafter the accuracy and precision are calculated using the RMSE and median RSD (*see* Boxes 4.1 *and* 4.2 on page 21).

4.5.2. Results

The second group of imagery sequences contains a limited amount of artificial seeding. However, while the same type of seeds was used, the seeding density was not exactly the same. Figure 4.19b presents these median flow velocities. Figure 4.19d illustrates the relative standard deviation of the results in the area of interest as defined in Figure 4.1b.

The first thing to notice is the shift of the image boundaries on the x-axis. While the perpendicular (or *Aerial*) view covers a width of about 6 metres, the (*Angled view I*) only covers 5 metres. This variation is caused by the shadow created by the river banks. The river banks mask a part of the river due to the difference between the water level and the height of the surroundings. Besides this, the orthorectification applied in this case did not take the z-axis difference between the GCPs and water level into account, leading to incorrect transformations. The second difference is related to the flow directions. For the whole video, the same orthorectification has been applied. However, due to the hovering of the drone perspective, unwanted distortions will occur, resulting into inconsistent flow velocities.

For the first case group (*see* Figures 4.19a *and* 4.19c), where the angled view points East, the difference in visible river width is not big. However, as is the case for case group II, the location of the river has shifted due to the orthorectification process.

Figure 4.20 illustrates the densities for both the median flow velocities and the relative standard deviation. For both case groups, as well as the median flow velocities as the RSD values change for the worse. However, as the impact of seeding density, light exposure, and drone hovering are not taken into account for these comparisons, it is too simplistic to define these differences to the point of view.

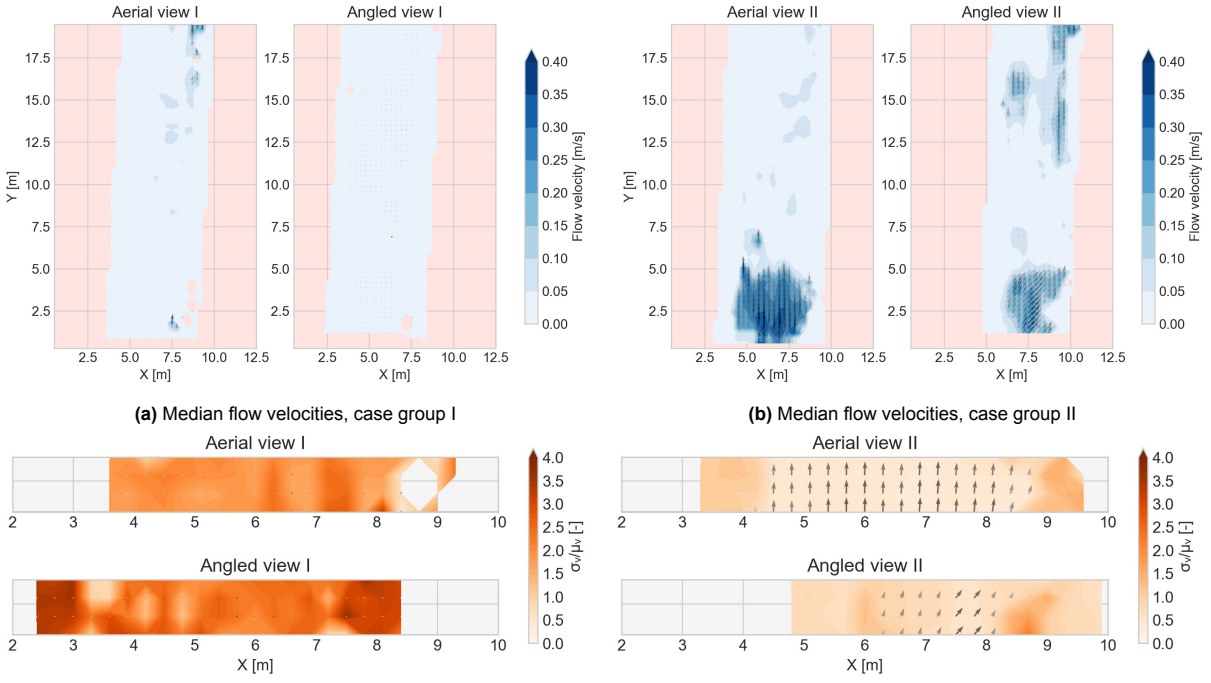

(a) Median flow velocities, case group I

(b) Median flow velocities, case group II

(c) Relative standard deviation, case group I

(d) Relative standard deviation, case group II

Figure 4.19: Median flow velocities and relative standard deviation heat maps of the orthorectified imagery for case group I ((a and c)), with an angled view facing East, and case group II ((b and d)), with an angled view facing West.

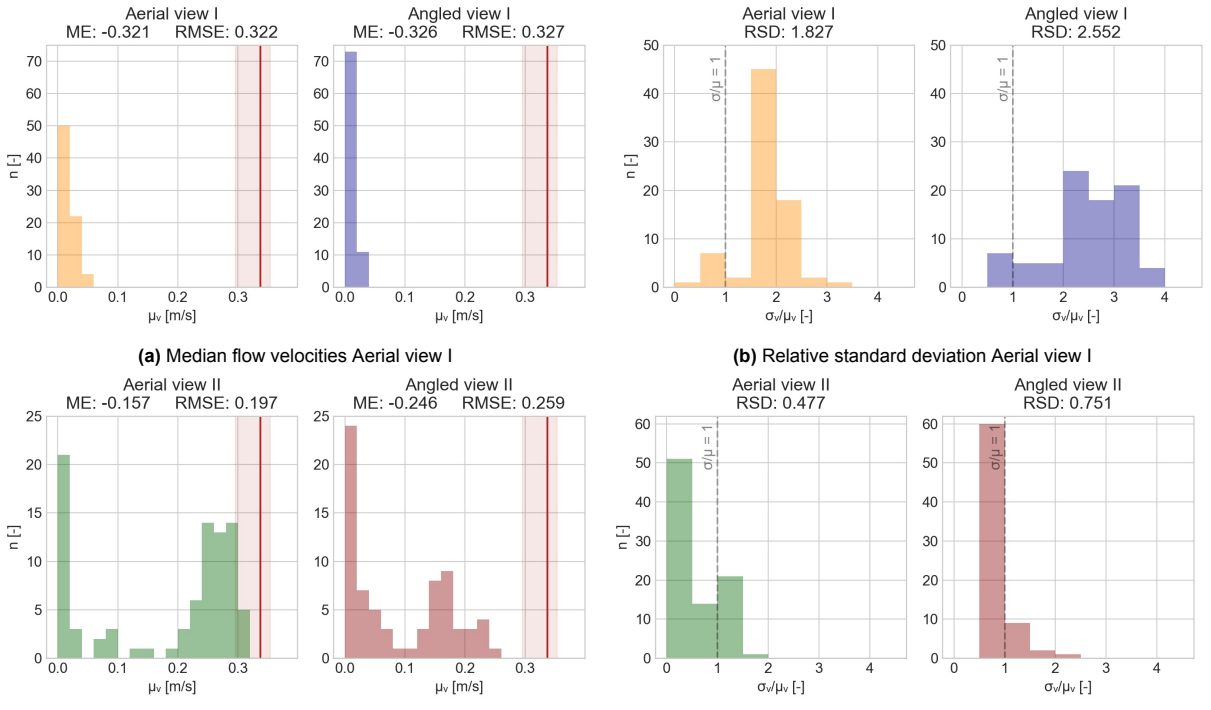

(a) Median flow velocities Aerial view I

(b) Relative standard deviation Aerial view I

(c) Median flow velocities Aerial view II

(d) Relative standard deviation Aerial view II

Figure 4.20: Distributions median flow velocities and relative standard deviation for the area of interest for both case groups. (a) and (b) relate to the angled point of view facing East, (c) and (d) relate to the angled point of view facing West.

4.6. Summary

To investigate the impact of different processing methods and environmental conditions on the accuracy and precision of the LSPIV method, this section summarizes the results. Following the structure of this chapter, first, the results related to the different processing methods are given (*see* Section 4.6.1). Thereafter, the impact of the environmental conditions is encapsulated, containing the seeding densities and the points of view (*see* Section 4.6.2).

4.6.1. Processing methods

OpenPIV output

In Table 4.2 the ME, RMSE and RSD results related to the different OpenPIV software steps are provided for two different seeding densities. The filtered results provide the best result related to precision for lower seeding densities, compared with the raw and interpolated results.

Table 4.2: ME, RMSE and RSD values related to the accuracy and precision of two different (artificial) seeding densities for the three sequential processing steps (*Raw*, *Filtered* and *Interpolated*) within OpenPIV.

	No artificial seeding			**Extensive artificial seeding**		
	Accuracy		*Precision*	*Accuracy*		*Precision*
	ME	RMSE	RSD	ME	RMSE	RSD
Raw	-0.322	0.322	1.865	-0.128	0.188	0.520
Filtered	-0.321	0.322	1.827	-0.128	0.188	0.520
Interpolated	-0.321	0.321	1.871	-0.128	0.188	0.520

Ranges in flow velocities

Subsequently, using the median flow velocities result in general for an underestimation of the flow velocities acquired with benchmark measurements. This is summarized in Table 4.3. For the *no artificial seeding* imagery – with approximately 3 particles per square metre – choosing a higher percentile substantially improves the accuracy of the method. However, when the seeding densities increase – up to 50 and 500 particles per square meter for the *limited* and *extensive artificial seeding* videos, respectively – the method start to overestimate the local flow velocities. For higher seeding densities, choosing the 75^{th} percentile gives the most logical result.

Table 4.3: ME and RMSE values related to the accuracy of the 50^{th}, 75^{th}, and 95^{th} percentile for three different (artificial) seeding densities.

	No artificial seeding		**Limited artificial seeding**		**Extensive artificial seeding**	
	ME	RMSE	ME	RMSE	ME	RMSE
50^{th}	-0.325	0.325	-0.204	0.232	-0.138	0.196
75^{th}	-0.300	0.301	-0.147	0.198	-0.110	0.181
95^{th}	-0.232	0.247	-0.090	0.174	-0.066	0.165

OpenPIV, Fudaa-LSPIV and imagery processing methods

Table 4.4 presents the grouping of both the ME, RMSE and RSD results of the different processing methods related to the comparison between OpenPIV and Fudaa-LSPIV, and the image manipulation method. Overall, all approaches – neither the processing software, nor the image manipulation method – do not have a noticeable impact on both the accuracy as the precision at the Dommel. Therefore, it is acceptable to use OpenPIV in this research instead of the more conventional used LSPIV software Fudaa-LSPIV. Furthermore, applying additional contrast correction to improve seed visibility does not provide substantially improved results.

4.6.2. Environmental conditions

Seeding density

As indicated in literature (e.g., Eltner et al., 2019; Kantoush et al., 2011; Kim, 2006; Le Coz et al., 2014; Muste et al., 2008, 2010), seeding is one of the crucial factors to influence the results of the LSPIV method. Table 4.5 presents the ME, RMSE and RSD results of videos with different seeding densities,

Table 4.4: ME, RMSE and RSD values for both the two different processing software (*Fudaa-LSPIV* and *OpenPIV*) and three different image manipulation approaches (*Original*, *Contrast I*, and *Contrast II*). The results are given for both no artificial seeding and extensive artificial seeding image sequences.

		No artificial seeding			**Extensive artificial seeding**		
		Accuracy		*Precision*	*Accuracy*		*Precision*
		ME	RMSE	RSD	ME	RMSE	RSD
Fudaa-LSPIV	Original	-0.317	0.318	1.866	-0.123	0.189	0.516
OpenPIV	Original	-0.321	0.322	1.827	-0.128	0.188	0.520
	Contrast I	-0.322	0.322	1.954	-0.136	0.192	0.540
	Contrast II	-0.322	0.322	1.891	-0.136	0.192	0.535

either by natural seeds or artificial seeding seeds like wood chips. As the seeding density increases, both the accuracy and precision improve. Seeds should not be too large or too heavy, as larger and heavier seeds might not correctly follow the flow velocities of the river. As the Dommel contained limited natural seeds, the flow velocities over the whole river width are barely traceable in this state.

Table 4.5: ME, RMSE and RSD values for three different (artificial) seeding densities. The results are given for *no*, *limited*, and *extensive* artificial seeding image sequences.

	Accuracy		*Precision*
	ME	RMSE	RSD
No artificial seeding	-0.321	0.322	1.827
Limited artificial seeding	-0.157	0.197	0.477
Extensive artificial seeding	-0.128	0.188	0.520

Point of view

In Table 4.6 the results for both the RMSE and RSD are provided related to the different point of view case groups. Due to inaccuracies in seeding density, drone hovering, and light exposure, it is difficult to define the direct effect of changes caused by the point of view. However, as stated in literature, if the angle is between 15°and 30°– relative to nadir – and the camera is fixed, the least impact on the accuracy of the LSPIV results is registered. Larger angles produce more error due to image perspective distortion (Harpold et al., 2006; Kim, 2006; Sutarto, 2015). According to Kim (2006) the camera position should not be of great effect on the accuracy of the LSPIV method, as long as the camera is stable and placed perpendicular to the flow direction. At an angle of 85°or larger the results become increasingly error prone.

Table 4.6: ME, RMSE and RSD values for the different point of view case groups. Case group I treats the angled view facing East and contains only natural seeding. Case group II treats the angled view facing West and contains limited artificial seeding.

	Case group I **No artificial seeding**			Case group II **Limited artificial seeding**		
	Accuracy		*Precision*	*Accuracy*		*Precision*
	ME	RMSE	RSD	ME	RMSE	RSD
Perpendicular	-0.321	0.322	1.827	-0.157	0.197	0.477
Angled	-0.326	0.327	2.552	-0.246	0.259	0.751

5

Surveying a flood wave using LSPIV

This chapter discusses the possibility to reconstruct flood waves in equatorial, fast response time streams using LSPIV. In Section 5.1 the set-up of the study site is discussed, including thelocations of the ground control points (GCPs) in a local coordinate system. In Section 5.2 the bathymetry of the Chuo Kikuu at the location of the measurements is discussed. Section 5.3 illustrates the process of gathering the water levels and obtaining the stream width during the various flood wave stages, using the local bathymetry. After this, in Section 5.4, the videos are submitted to the LSPIV method to gather the surface flow velocities per frame step. Thereafter, in Section 5.5, a method for obtaining the cross-sectional average surface flow velocities and their uncertainty bands, and an approximation for the depth-averaged flow velocities is given. Lastly, in Section 5.6, the discharge ranges for each video are determined, providing the median discharge and lower and upper limits. Combining all discharges results in a rating curve.[6]

5.1. Study site set-up

Along the Chuo Kikuu a LSPIV gauging site is established and piloted. Using a Hikvision CCTV camera – mounted to a wall alongside the stream Chuo Kikuu at an inclined angle of 50°– 71 different videos were obtained, capturing a flood wave as it occurred on December 17, 2019 from 06:00 till 18:30 EAT.[7] The set-up of the study site is shown in Figure 5.1, together with the chosen area of interest. The wall on which the camera is mounted, is slightly inclined related to the flow direction of the stream resulting in the left side of the imagery (upstream) being optically closer than the right side (downstream).

During the rising part of the flood wave, a noticeable amount of seeds were floating by in the form of debris – e.g. all sorts of plastics, clothing, foam, and branches. As the amount of debris substantial

(a) Location of the measured cross-section and GCPs **(b)** Area of interest

Figure 5.1: Example of a frame captured by the CCTV camera showing (a) the location of the cross-section measurements and locations of the ground control points (GCPs), and (b) the area of interest.

[6]Rating curves provide the discharge versus the water level at given points in a stream.
[7]East African Time, UTC+03:00.

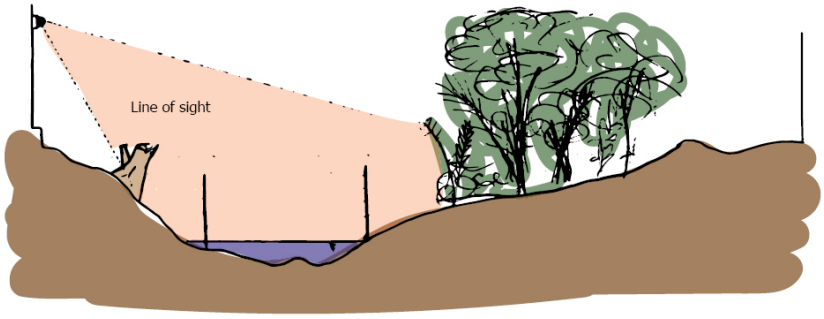

Figure 5.2: Schematic cross-sectional view of the Chuo Kikuu (looking upstream), showing the line of sight of the camera and the corresponding blind spots due to the incline of the camera and the presence of dense vegetation.

improves the accuracy of the LSPIV method – as found in Section 4.4 – it is expected that during the ascending part of flod wave, the most accurate discharges will be found. The interval between each video is approximately ten minutes. Over the following two days, two other videos were gathered to capture the full decline of the flood wave, bringing the total amount of videos to 73. Each video has a length of five seconds and is captured in 25 frames per second, resulting in 125 frames per video.

As GCPs, four bamboo sticks were placed in the river. GCP B would act as water level gauge (*see* Figure 5.1a). However, – as the GCPs easily collect debris – during the flood wave all GCPs – including the gauge – got flushed away. For the GCPs a local XY-coordinate system is set up. The coordinates of each GCP are provided in Table 5.1, following the labels as they are shown in Figure 5.1a. As it is not possible to find the GCPs for every video, the location of the GCPs on the imagery using linear functions (*see* Section 5.4.1).

Table 5.1: XY-coordinates of the ground control points in a local XY-coordinate system.

	X [m]	Y [m]
A	0.25	0.10
B	4.25	0.00
C	4.50	3.30
D	0.00	3.30

The line of sight of the camera is shown in Figure 5.2. This schematic view of the cross-section shows the blind spots of the camera: directly beneath the camera and – on the other side of the stream – the floodplain due to the presence of dense vegetation. As no flow velocity estimations from these areas can be obtained, the flow velocities are assumed to be zero.

5.2. Bathymetry

Along the centre of the imagery (*see* Figure 5.1a), measurements are performed to obtain the local bathymetry. Every 50 centimetre the ground level is determined relative to the lowest point in the stream, using a levelling rod. Figure 5.3 presents the results of these measurements together with the quadratic interpolated approximation. The Y-coordinates – providing location over the width of the stream – are relative to the location of GCP D (*see* Figure 5.1). Both the left as the right border of the bathymetry are bounded by vertical walls of approximately 2.5 metres high.

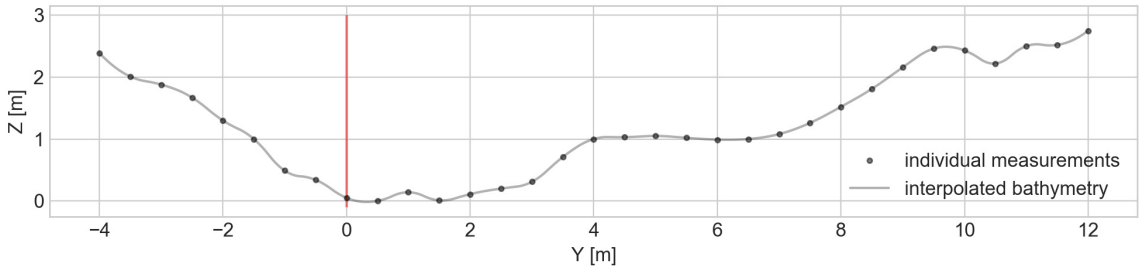

Figure 5.3: Local bathymetry relative to its lowest point of the Chuo Kikuu showing the individual measured points and the quadratic interpolated approximation. The Y-coordinates are relative to the location of ground control point D, accentuated with a vertical red line.

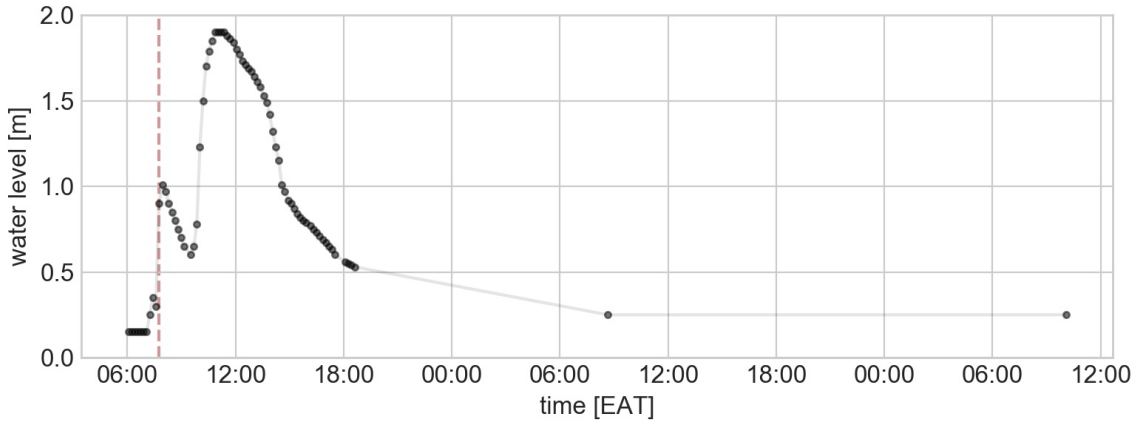

Figure 5.4: The flood wave in terms of water levels, relative to the local streambed. With a vertical dashed line it is indicated when the GCPs flushed away.

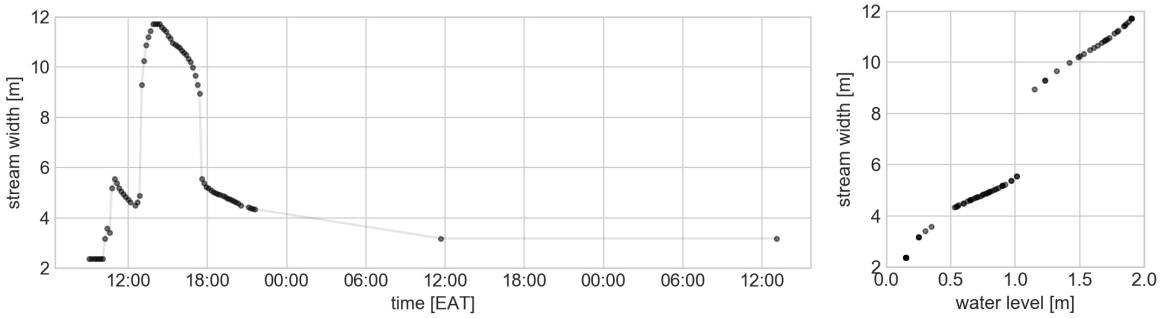

(a) Stream width during the flood wave

(b) Water level versus stream width

Figure 5.5: (a) Stream width during the flood wave and (b) the water levels against the stream showing the moment the floodplain starts to contribute to storing the water.

5.3. Water levels and stream widths

Using captures of all 73 videos, the water levels during the entire flood wave are estimated. For the first few videos, the GCP acting as gauge was used to determine the water level (point B in Figure 5.1a). For the subsequent videos, the water levels were estimated by relating the edge of the stream to the bathymetry measurements. Figure 5.4 presents for every video the estimated water level relative to the lowest point of the cross-section. In the figure two peaks can be observed, the first one peaking around 08:00 EAT and the second at 11:30 EAT. During this last peak, water levels of 1.98 metres were observed. These different peaks are referred as the first and second flood wave, respectively.

Using the water levels and bathymetry, the corresponding widths of the stream and the locations of both the banks are determined. The result of this process is shown in Figure 5.5. In Figure 5.5b the water levels are plotted against the stream widths, clearly showing the moment the floodplain starts to be filled with water. As the floodplain is densely covered with vegetation, it is assumed that this part does not actively contribute to the total amount of water flowing through the stream, and mainly has a storage function.

5.4. Applying LSPIV

Following the outline provided in Section 2.4, in order to extract flow velocities from the videos, the individual frames have to be made suitable for the LSPIV analysis by applying several manipulation steps. In Section 5.4.1 these steps are further explained following the structure of Section 2.4. In Section 5.4.2, the software processing approach is clarified.

5.4.1. Image preparation

The three image preparation steps are sequentially (1) lens distortion correction, (2) image orthorectification, and (3) gray scaling, contrast- and gamma correction. In the following sections, the

used parameters are defined as set up in Section 2.4.1.

Lens distortion correction
While the camera software used for the measurements at the Dommel (*see* Chapter 4) has a built-in function to directly correct its images for lens distortion, the CCTV camera used in Dar es Salaam does not. As the exact characteristics of the camera used are unclear, it is assumed the imagery is only affected by radial distortion. The distortion coefficients are assumed to be:

$$C_{dis} = [-1.0 \cdot 10^{-5},\ 0,\ 0,\ 0,\ 0]$$

The conversion matrix is set to:

$$M_{con} = \begin{bmatrix} 8.0 & 0 & 2.0 \\ 0 & 8.0 & 2.0 \\ 0 & 0 & 1 \end{bmatrix}$$

Image orthorectification
In order to make sure all distances within the image are the same, orthorectification is applied. However, as for each different water level the perspective changes, the p_{img} – locations of the GCPs in the imagery – will be different. Therefore, to cope with the changing water levels, the p_{img} xy-coordinates are set to be dependent on the water levels using the following linear equations, assuming the poles are placed perfectly vertical:

$$\begin{aligned} \textbf{A:}\quad & x_A = -0.0167 \cdot H + 993.5 \\ & y_A = -1.2667 \cdot H + 480 \\ \textbf{B:}\quad & x_B = 0.575 \cdot H + 1493.8 \\ & y_B = -1.2917 \cdot H + 519.75 \end{aligned} \qquad \begin{aligned} \textbf{C:}\quad & x_C = 0.85 \cdot H + 1696.5 \\ & y_C = -1.2 \cdot H + 881 \\ \textbf{D:}\quad & x_D = 0.0417 \cdot H + 939.75 \\ & y_D = -1.4 \cdot H + 850 \end{aligned} \tag{5.1}$$

where x_n an y_n are the locations of the GCPs on the imagery in pixels; and H is the water level.

As is expected, the two front GCPs (C and D) show a larger movement for the same water level than the two GCPs in the back (A and B). Simultaneously with orthorectification process, the pixel density is set to 100 pixels per metre.

Gray scaling, contrast- and gamma correction
The final steps to prepare the imagery are the gray scaling, contrast- and gamma correction (*see* Section 2.4.1). As is found in the previous chapter, additional contrast correction does not necessarily improve results. Therefore, the contrast correction is not applied on the videos obtained at the Chuo Kikuu. For the gamma correction, a factor of $\gamma = 0.4$ has been chosen.

Combining all image preperation steps lead to the image manipulation as is shown in Figure 5.6. At both sides of the manipulated frame black rectangles appear due to the orthorectification process.

(a) Original frame **(b)** Manipulated frame

Figure 5.6: Example of the full image manipulation process for imagery obtained at the Chuo Kikuu. Sequentially, the image is lens distortion corrected, orthorectified, and turned into gray scales with additional gamma correction.

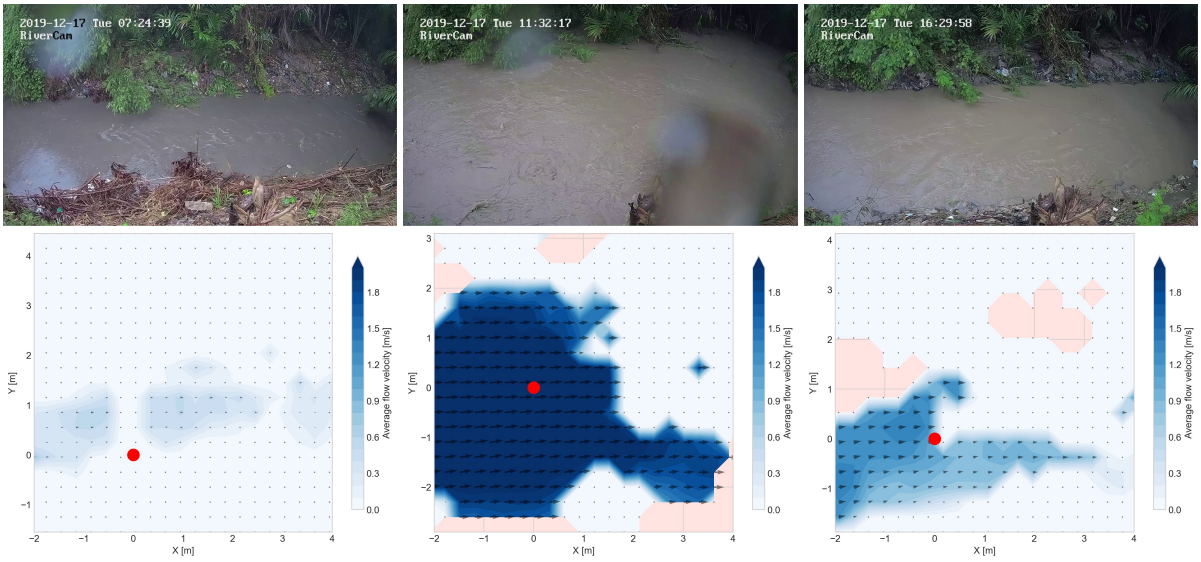

(a) 07:24 EAT **(b)** 11:32 EAT **(c)** 16:30 EAT

Figure 5.7: Three stages of the flood wave showing different water levels and sections of the corresponding averaged LSPIV results. The red dots indicate the location of GCP *D*.

5.4.2. Software processing

Similar to the processing in Chapter 4, the grid cell sizes – or interrogation windows – are set to 60 x 60 pixels, which correspond to grid cells of 60 x 60 centimetres. An overlap of 30 pixels is used. The complete imagery is then processed using OpenPIV. Figure 5.7 presents three different stages of the flood wave and the median flow velocities per interrogation window: (a) at the ascending part of the first peak, (b) during the peak of the second flood wave, and (c) during the descending part of the wave. In the latter two imageries many grid cells do not provide any, or very low values, while at those locations water is flowing. The missing sections are mainly caused by water droplets on the camera lens. The low values can either be caused by the lack of seeds at the location, or due to the averaging process. In the upcoming section possible solutions to improve the gathered results are provided.

5.5. Cross-sectional flow velocities

To be able to determine the discharge of the stream at the moment of a video capture, the depth-averaged flow velocities are needed. However, the averaged results appear to be structurally lower than the flow velocities obtained when tracing debris with the eye. When looking at the three stages as shown in Figure 5.7, the expected maximum flow velocities are assumed to be approximately (a) 1 m/s, (b) 2.5 m/s, and (c) 1.5 m/s. Section 5.5.1 presents two possible solutions for improving the obtained surface flow velocities. Section 5.5.2 treats the approach for determining the depth-averaged flow velocities.

5.5.1. Surface flow velocity adjustments

When examining the flow velocities as obtained at each individual frame of a video, it is immediately clear that due to the presence of a lot of near zero values, high flow velocities are levelled out. The velocity distributions over the width of the stream for the three example videos are provided in Figure 5.8, assuming that the Y-component of the flow velocities can be neglected. When taking a higher percentile instead – e.g. the 75th percentile – the results already come closer to the benchmark values.

However, as presented in Figure 5.8, there are a lot of measurements around 0 m/s which result in lower averaged flow velocities. Furthermore, at some locations no flow velocities are measured, where they are to be expected (e.g. in Figure 5.8c a sudden drop in flow velocities occur at $Y = 1.5$ metre). It is expected that the results can be further improved by adding two other processing steps to the surface flow velocity approximation: (1) filtering out unwanted low flow velocity measurements, and (2) replacing low flow velocities based on the vertical logarithmic progression relationship of the surface flow velocities.

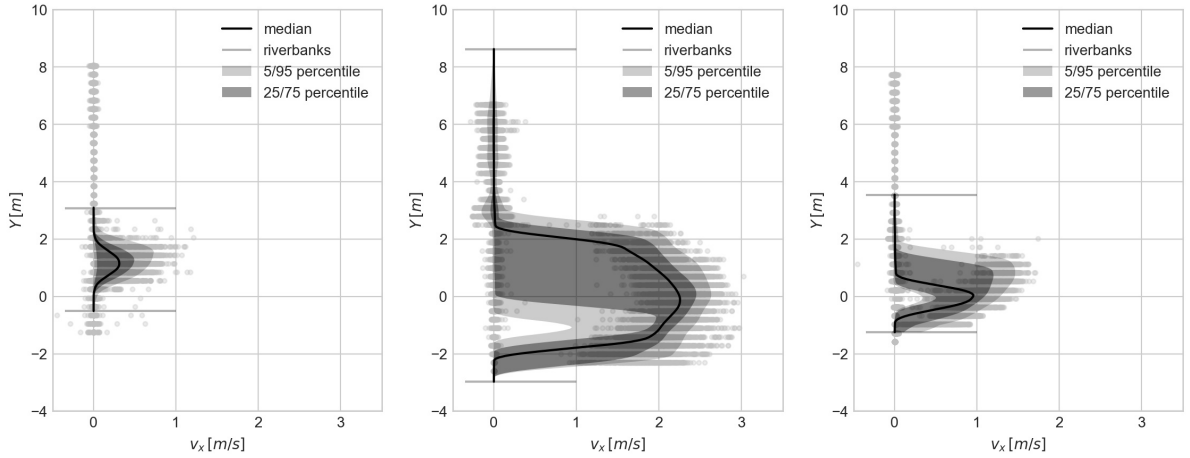

(a) 07:24 EAT **(b)** 11:32 EAT **(c)** 16:30 EAT

Figure 5.8: Distribution of the flow velocities for different width sections together with the mean flow velocity and the 5th/95th and 25th/75th percentile boundaries. The horizontal gray lines illustrate the stream banks.

Filtering flow velocities

Figure 5.8b indicates that at a single horizontal line – while containing mainly high velocity measurements – there are still several points where no flow velocities are observed. These low flow velocities result in lower averaged flow velocities. Therefore, to eliminate the effect of the low flow velocities, all values which meet the following requirement are filtered out:

$$V_X < V_{q95} - 2 \cdot \sigma_{V_X} \tag{5.2}$$

where V_X is an individual measurement point in a cross-section; V_{q95} the 95 percentile flow velocity at that cross-section; and σ_{V_X} the standard deviation of the flow velocities at that cross-section.

Applying the filtering as it stands would result in the removal of values which should not be removed. Therefore, the filtering should only be applied on cross-sectional sections when there is a division in higher and lower flow velocities. For this reason, the filter is only applied at cross-sectional sections where the following statement is true:

$$V_{q95} > 2.5 \cdot \sigma_{V_X} \tag{5.3}$$

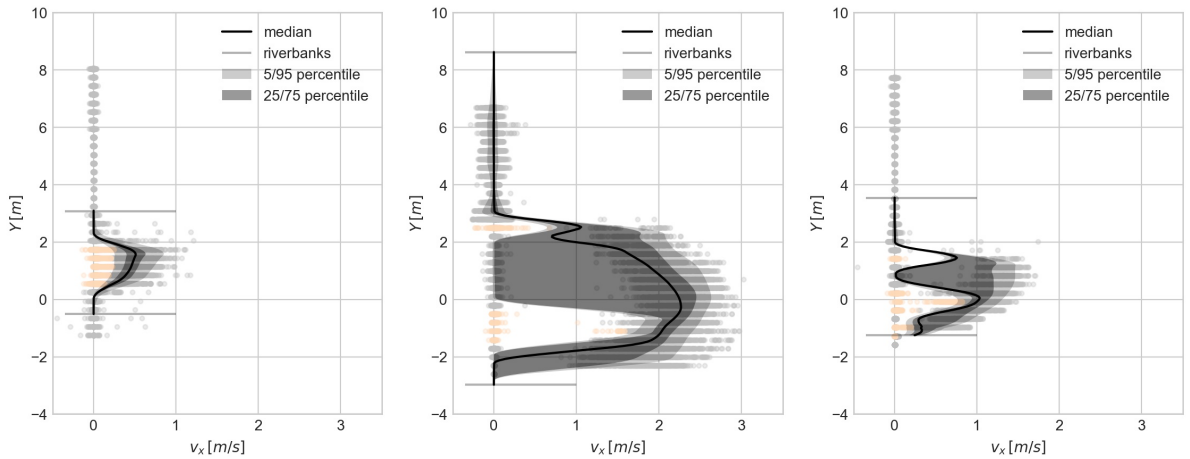

(a) 07:24 EAT **(b)** 11:32 EAT **(c)** 16:30 EAT

Figure 5.9: Distribution of the flow velocities after filtering for different width sections together with the mean flow velocity and the 5th/95th and 25th/75th percentile boundaries. The horizontal gray lines illustrate the stream banks. The orange dots represent the removed measurements.

Applying this filtering on the three videos, leads to the distributions as provided in Figure 5.9. The filtering process already improves the LSPIV results. However, the filtering process does not fully remove all unwanted measurements. As this mainly influences the lower percentiles, this is accepted. As found in Chapter 4, the most probable flow velocities are found between the 50th and 75th percentile. An potential better solution is filtering based on the bimodality of the flow velocity distributions. If bimodality – or even multimodality– is found, the lower flow velocities could be removed using – for instance – Otsu's thresholding (Otsu, 1979).

Substituting flow velocities

As presented in Figure 5.9c flow velocities estimated close to zero – mainly due to missing seeds – while nearby sections show flow velocities between 0.5-1.5 m/s. By replacing these missing flow velocities by their expected flow velocities, a more accurate cross-sectional flow profile could be obtained. The substitute flow velocities are determined using the vertical logarithmic progression relationship of the surface flow velocities at different cross-sectional sections.

Figure 5.10a presents for all videos the median flow velocities of the filtered LSPIV results over the width of the stream. Using the flow velocities at different cross-sectional sections – between $Y = -1.5$ and $Y = 0.5$ metre– a relationship between the surface flow velocities is obtained. These are visualised in Figure 5.10b. The vertical distribution is then approximated by the Prandtl-von Kármán logarithmic law:

$$V_{x;sub}(h) = \frac{u_\star}{\kappa} \ln\left[\frac{h-d}{h_0}\right] \tag{5.4}$$

where $V_{x;sub}(h)$ is the flow velocity with a water depth of h; $u_\star$ the shear velocity; κ the von Kármán contast (≈0.41); d the zero-plane displacement; and h_0 the roughness length. The shear velocity is generally approximated around 5 to 10% of the maximum flow velocity and the roughness length about one-tenth of the height of local obstructions.

By applying a non-linear least squares fit to the data set, and d is preset to be 0.15 metre – based on the local bed characteristics – it is found that for the 50th percentile values $u_\star$ and h_0 are respectively 0.235 m/s and 0.054 m. Table 5.2 presents for each percentile the parameters for Equation 5.4.

Using these parameters, the median flow velocities and their corresponding percentiles are replaced when the median flow velocity at a specific width section meets is half the value found with the vertical logarithmic progression function, the flow velocities for the different percentiles in that cross-sectional section are replaced based on the formula stated in Equation 5.4. This substitution is applied under

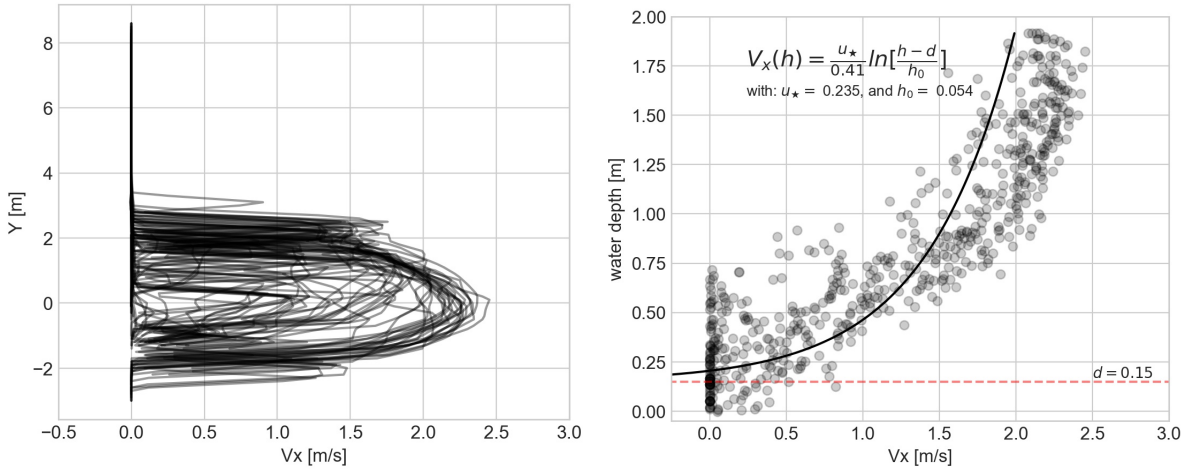

(a) cross-sectional flow velocities for all stages

(b) Vertical flow velocity profile approximation

Figure 5.10: For all videos (a) presents the cross-sectional median flow velocities. For several width sections between Y=-0.5 and Y=-2.5 the flow velocities are combined to generate a (b) vertical profile which illustrates the development of the median surface flow velocities for changing water depths.

Table 5.2: Parameters for the vertical flow velocity approximation with d=0.15 m.

	$u_\star$ [m/s]	h_0 [m]
5th	0.187	0.070
25th	0.203	0.063
50th	0.235	0.054
75th	0.236	0.038
95th	0.250	0.032

the assumption that the vertical logarithmic progression relationship of the surface flow velocities are homogeneous over the entire stream width and over time. This threshold is set to ensure that reasonable flow velocities – following the LSPIV method – are not directly substituted by the theoretical flow velocities. As it is assumed that the flow velocities are zero in the floodplain, the process is not applied at this section. The substitution is summarized in the Equation 5.5:

$$V_{q50} < 0.5 \cdot V_{x;sub} \tag{5.5}$$

Because of the assumption that the same vertical logarithmic progression relationship applies over the whole width, at certain parts flow velocities will can get overestimated, while at other places, underestimation might occur. The main reason for these differences is the variation in the river bed roughness. Moreover, at the descending part of a flood wave lower flow velocities can be expected than in the ascending part, while the same water level is reached – when most of the seeds pass by – resulting into a possible overestimation of the flow velocities in the descending part of the flood wave.

Figure 5.11 presents the results when applying both the filtering and the substitution process on the original LSPIV results. For these three examples, the substituted values seem to overestimate the flow velocities compared with the surrounding known results. However, these differences are generally within a 10% margin. For the results presented in Figure 5.11c the cross-sectional profile substantial improves.

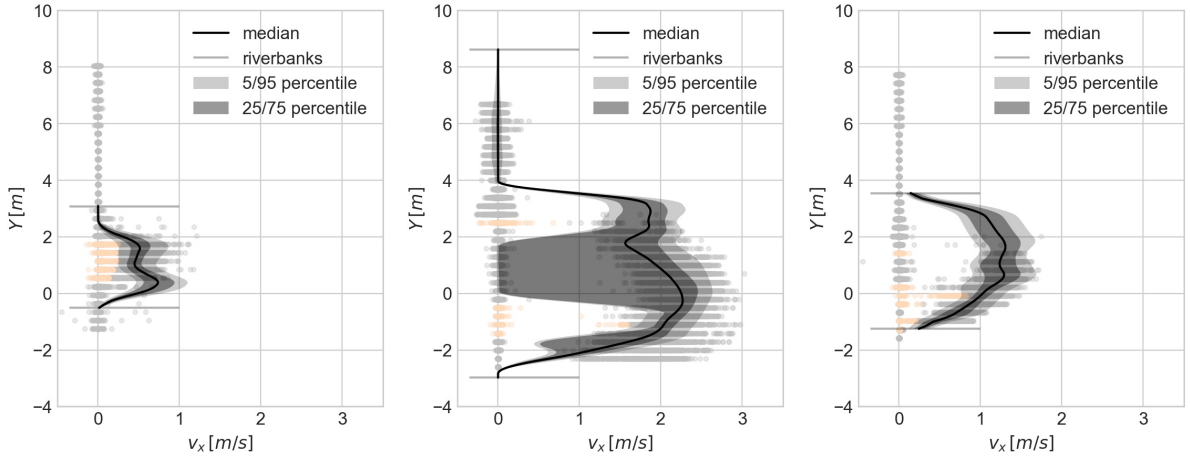

(a) 07:24 EAT **(b)** 11:32 EAT **(c)** 16:30 EAT

Figure 5.11: Distribution of the substituted flow velocities per width section. For each timestamp the filtered (orange dots) and preserved (gray dots) flow velocities are provided, together with the mean flow velocity and the 5th/95th and 25th/75th percentile boundaries.

5.5.2. Depth-averaged flow velocities

To determine the depth-averaged flow velocities, the surface flow velocities are multiplied by the empirical depth-average coefficient α. This coefficient depends on the bed roughness and river dimensions and usually varies between 0.72 and 0.93. If the depth-average coefficient cannot be determined, it is often assumed to be 0.85 (e.g., Dramais et al., 2011; Eltner et al., 2019; Le Coz et al., 2010; Muste et al., 2008). Because during the flood wave no measurements could be performed to estimate this coefficient, an assumption will be made, based on similar cases in literature.

The average flow velocity of the vertical profile – shown in Figure 5.10b – is 0.77 times the maximum flow velocity. However, as this profile only consists of surface flow velocities and therefore not correctly describes the vertical profile at a specific time, this value will not be representative: for a vertical distribution both the logarithmic distance from the bed as from the free surface should be taken into account (Yang et al., 2004). for a natural stream with roughly the same riverbed characteristics as the Chuo Kikuu, but a wider stream bed, Stumpf et al. (2016) found coefficient values ranging from 0.85 to 1.00, with an average of 0.89. To adjust for the smaller stream width of the Chuo Kikuu, the depth-average coefficient is set to 0.85.

5.6. From flow velocities to discharges

After acquiring the surface flow velocities and the depth-average coefficient, discharges can be determined. The results of this process are provided in Section 5.6.1. In Section 5.6.2 the discharges are compared with sudden gulp salt dilution measurements.

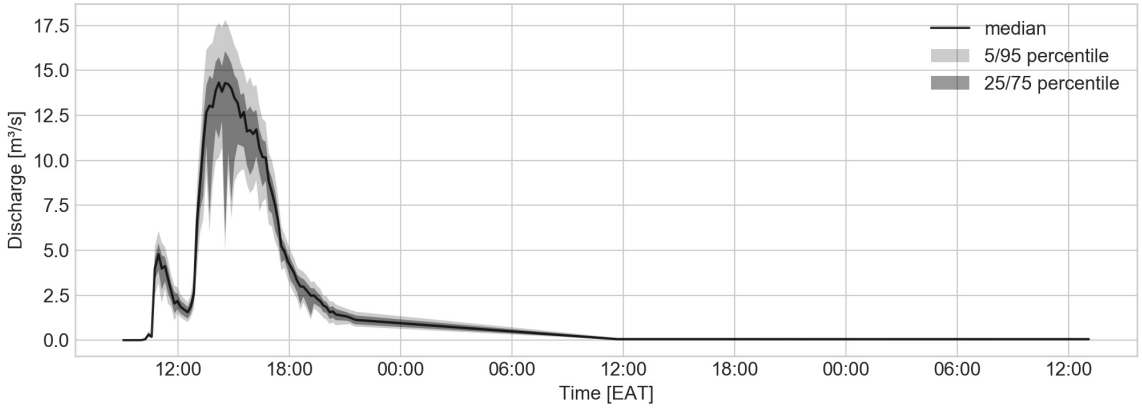

Figure 5.12: Discharges using the filtered and substituted flow velocities obtained using the LSPIV method.

5.6.1. Discharge estimation

Using the stream's bathymetry, the filtered and substituted surface flow velocities, and the depth-average coefficient, the discharge during each of the 73 video is determined. This approach is similar to the velocity-area method, discussed in Section 2.2.1. Figure 5.12 presents the end result of the complete post-processing approach.

By combining the discharges with the water levels, a rating curve is created as provided in Figure 5.13. The data points can be described as follows:

$$Q(H) = a \cdot (H - H_0)^b \tag{5.6}$$

where H_0 is the water level where $Q = 0$; and a and b are the rating curve constants.

When using the median discharges and for H_0 is 0.15 metre, values of 5.98 and 1.57 are found for a and b, respectively. In Table 5.3 the constants are shown based on the median – i.e. 50th percentile – flow velocities, and the 5th, 25th, 75th, and 95th percentiles. For open channels – like rivers and streams – it is expected that b falls within the range 1.5 to 2. For a stream similar to the Chuo Kikuu, it is assumed that b will approach 2. With a value of 1.57 the current discharges, especially at higher flow velocities, are probably underestimated. The main reason of this underestimation can be found in the fact in the assumptation that no flows in the floodplains occurs, resulting in lower discharges at higher water levels, and a lower value for b.

5.6.2. Discharge validation

During a smaller precipitation event on December 5, 2019, multiple sudden gulp salt dilution measurements were applied (*see* Section 2.2). The results of these tests are shown in Table 5.4.

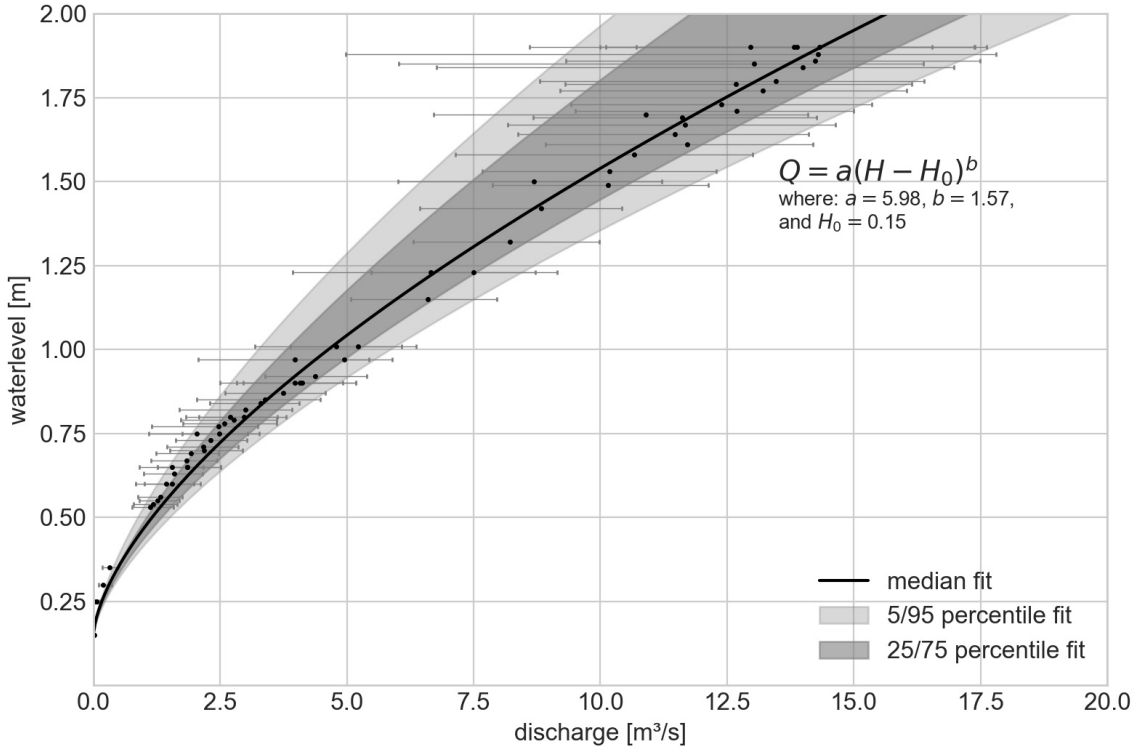

Figure 5.13: Rating curve and corresponding fit of the median discharges – including the uncertainty bands – obtained using the filtered and substituted surface flow velocities.

Table 5.3: Rating curve constants for the 5th, 25th, 50th, 75th, and 95th percentile

	a	b
5th	4.127	1.485
25th	4.809	1.456
50th	5.977	1.565
75th	6.701	1.537
95th	7.505	1.534

For similar water levels – 0.3 to 0.4 m – the discharges should be approximately 0.48 [0.25-0.90] m³/s, according to the rating curve. These discharge is lower than the discharges found with the sudden gulp salt dilution method. These differences could be caused by the fact that the salt dilution measurements were gathered during the declining part of the flood wave, while the lower water levels in the rating curve are mainly data points of the ascending part of the flood wave. Furthermore, in between December 5 and December 17, environmental conditions could have been changed. An other option is that the sudden gulp salt dilution measurements overestimation the discharges due to insufficient mixing of the salt, or due to too low salt concentrations.

Another way to validate whether the discharges found are acceptable, is a comparison with the total precipitation fallen in the contribution catchment. This method is discussed in Chapter 6.

Table 5.4: Results of the sudden gulp salt dilution measurements on December 5, 2019. During the measurements, the water levels were approximately 0.3-0.4 metre.

	EC_0 [μS/cm³]	Q [m³/s]
measurement I	292	1.64
measurement II	313	1.54
measurement III	341	1.11

5.7. Summary

With use of 73 videos – captured at the Chuo Kikuu – and the LSPIV method, an reconstruction of a flood wave is made. The imagery is prepared through orthorectification, gray scaled and gamma correction whereafter PIV processing is applied. Thereafter, the results are post-processed through filtering and substitution. Lastly, using an empirical depth-average coefficient and the local bathymetry, discharges are estimated. As during the ascending part of the flood wave, many seeds came by in the form of debris, it is expected that during these parts of the flood wave the most accurate results are gathered.

Due to the presence of dense vegetation in the line of view of the camera, flow velocities in the floodplain could not be observed. Therefore, it is assumed that the flow velocities at this part if the stream is zero. Because of this assumption, discharges are probably underestimated during high water levels. Using arbitrary chosen formulas, it is tried to filter as many unwanted values as possible. An less arbitrary approach of filtering could be the removal of flow velocities based on bimodality and Otsu's thresholding (Otsu, 1979).

With use of the found relationship for the vertical logarithmic progression relationship, values which probably underestimate the actual flow velocities are substituted, under the assumption that the same vertical logarithmic progression relationship occurs over the whole width of the stream. As the relationship is mainly based on values found in the ascending part of the flood wave – when most of the seeds flow by – and the fact that flows during the ascending part of the wave are usually higher than during the descending part, for the same water level, the discharges in the descending part of the flood wave are probably overestimated.

The impact of the filtering and substitution post-processing steps on the median discharges is provided in Figure 5.14. When comparing the total discharges, applying filtering reduces the bandwidth with 37% and the mean total discharge increases with 20%. Applying only substition of the surface flow velocities increases the total mean discharge by 84% relative to the untreated results. Applying both filtering and substitution increases the total mean discharge with 96%

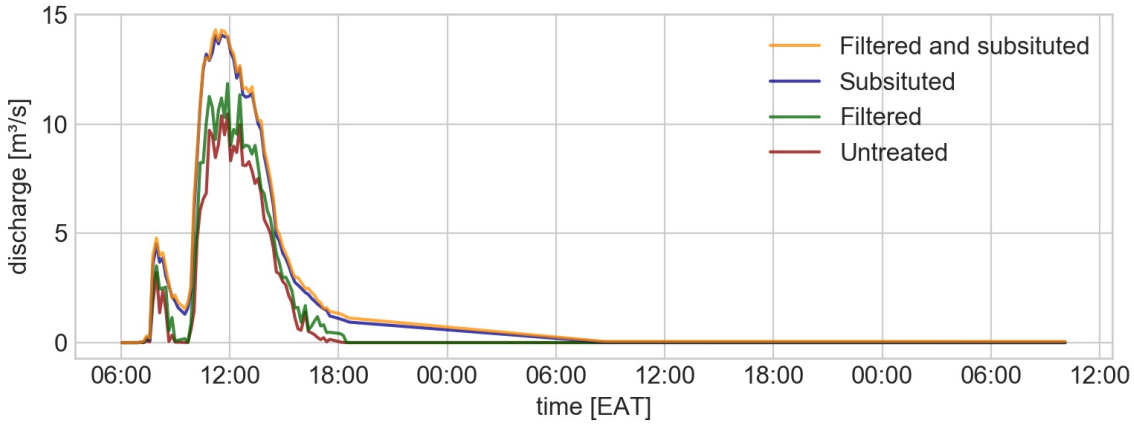

Figure 5.14: Median discharges for different post-processing approaches.

6

Comparing precipitation and discharges

This chapter discusses how discharges obtained using the LSPIV method – as discussed and summarised in Chapter 5 – compare against the total event volumetric precipitation of the contributing catchment. The event volumetric precipitation is determined using meteorological data measured at a nearby gauging station. To achieve this comparison, three steps have to be taken: (1) determination of the contributing catchment (*see* Section 6.1), (2) collection an analysis of precipitation data (*see* Section 6.2), and (3) the comparison of the event volumetric precipitation against the event integrated flows (*see* Section 6.3).

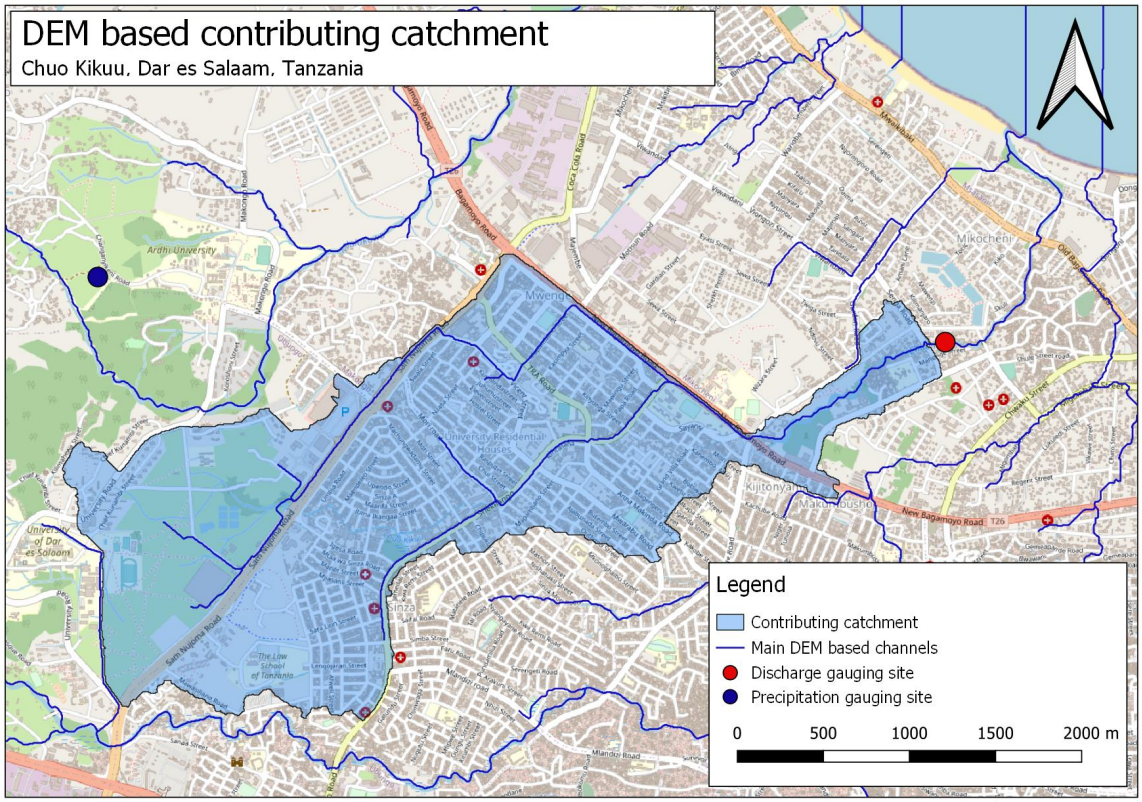

Figure 6.1: Contributing catchment of the study site in Dar es Salaam, Tanzania. De catchment is based on a 5m DEM with the local man-made drainage systems burned in. The discharge gauging site and meteorological gauging station are indicated with a red and blue dot, respectively. The total catchment area is $5.69 \cdot 10^6$ m².

6.1. Catchment estimation

In Figure 6.1 the contributing catchment for the gauging site (highlighted with a red point) is shown. This catchment is estimated using QGIS and a digital elevation map (DEM)[8] of the local area. As the environment is densely populated, and drainage systems are present, flows do not necessary follow the paths as will be found with solely the DEM. Therefore, the man-made drainage systems[9] are burned into the DEM. Using the Strahler stream order of each cell, the main tributaries are determined and compared with the practical drainage flow directions. Using the tributaries the catchment area is estimated, which is approximately $5.69 \cdot 10^6$ m². This area is probably

Estimating the contributing catchment using the DEM and locations of man-made drainage systems probably leads to an overestimation of the actual catchment size. However, this offset is as much as possible reduced by checking the flow paths found based on the Strahler stream order with the actual flow directions as stated by local data.

6.2. Precipitation data

A meteorological gauging station of TAHMO is placed approximately one kilometre away from the catchment's border (marked with a blue dot in Figure 6.1). This gauging station – together with seven other stations – is placed as part of TURP to provide meteorological data like precipitation, humidity levels, temperature and wind speeds.

Figure 6.2 presents the precipitation event of 17 December 2019 in millimetres per second as acquired by the station. The station provides for every five minutes the total measured precipitation. The days before and after the event, no precipitation was measured. The event consists of three smaller events, the first taking place from 06:00 till 08:30, the second event from 08:30 till 11:30, and the third event from 11:30 till 16:0 , which consisted mainly out of lower precipitation rates. The first of these events contained approximately 35% of the total volume of precipitation. The second and third event contributed respectively 55% and 10% to the total precipitation event.

6.3. Discharge-precipitation comparison

To determine the volumetric precipitation over the whole catchment, it is assumed that the precipitation gathered at the TAHMO station is uniformly distributed over the whole catchment. The total volume of precipitation – integrated over the event period (06:00 until 16:00 EAT) – is $770 \cdot 10^3$ m³.

In Figure 6.3 the volumetric precipitation – acquired by multiplying the precipitation measured at the TAHMO gauging station with the catchment area – together with the discharges obtained using the filtered and corrected surface flow velocities (*see* Section 5.5.1) are shown. The first point to notice is that while

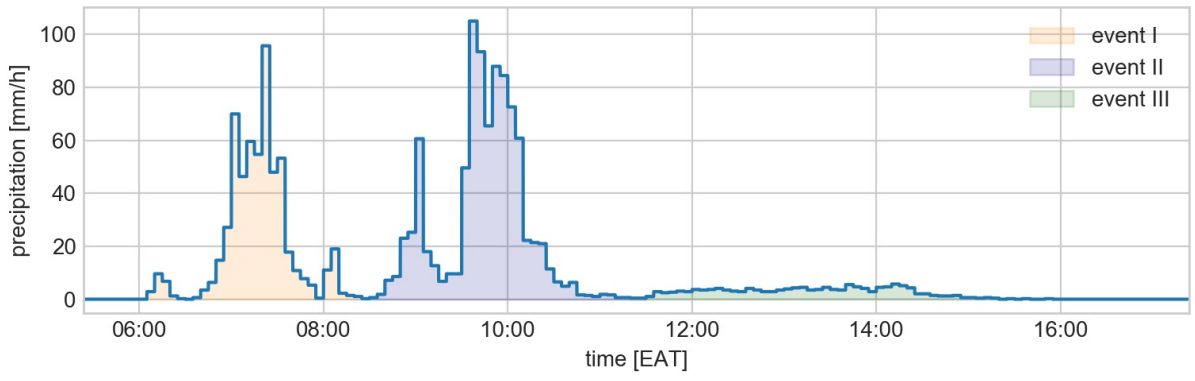

Figure 6.2: Precipitation as monitored by the TAHMO gauging station located at Ardhi University, Dar es Salaam on December 17, 2019. The different precipitation events I (06:00-08:30), II (08:30-11:30), and III (11:30-16:00) are accentuated with the colours orange, blue, and green, respectively.

[8] As part of the Tanzania Urban Resilience Program, this data, together with other types of open access data can be acquired from `https://resilienceacademy.ac.tz/`.
[9] *See* Footnote 8.

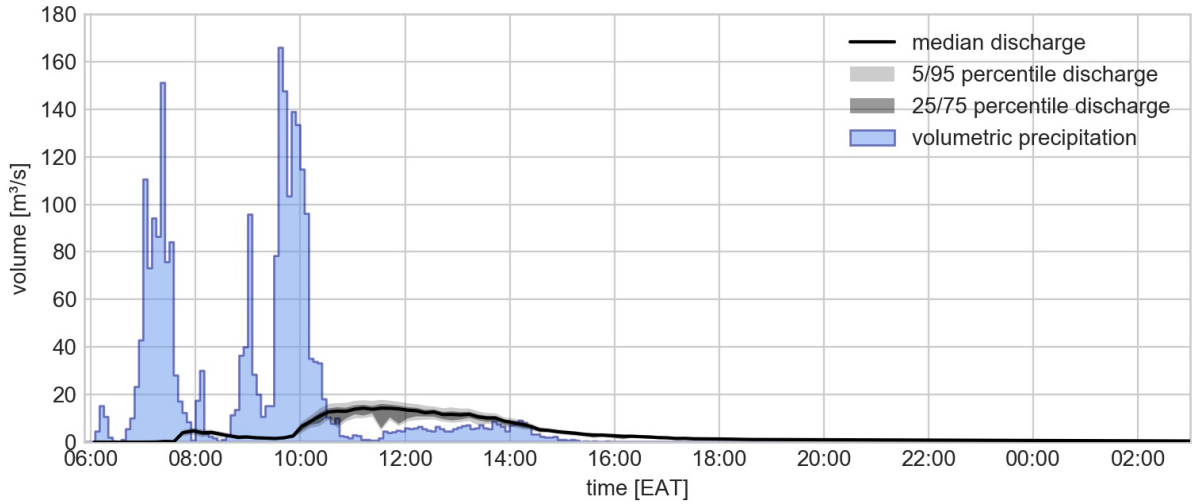

Figure 6.3: Filtered and substituted discharges as recorded at the study site in Dar es Salaam, combined with the volumetric precipitation over the contributing catchment based on the precipitation observed at the TAHMO station.

the first precipitation event contains 35% of the total precipitation measured, the first discharge peak only contains 8% [5-10] of the total discharge volume.

This major difference in portion is likely related to local buffers – e.g. local pools, roof surfaces, rainwater harvesting storage tanks, and soil storage capacity. It is expected that most of the precipitation is stored in these buffers, which were probably empty due to the long dry period prior to the precipitation event. By the time the second event took place, most of the buffers were probably (partly) filled, and therefore resulted into more runoff.

The volumetric precipitation is compared with discharges containing different post-processing steps. These are (1) the final discharges of Chapter 5 – with filtering and substitution of flow velocities– (2) when only substitution is applied and no additional filtering, (3) when only additional filtering is applied, and (4) when the raw PIV processing results are used – without additional post-processing. In Figure 6.4a the different total discharge volumes are shown.

The impact of local buffers be seen in Figure 6.4b. The runoff coefficient based on the filtered and substituted flow velocities is approximately 37% [24-48]. For similar urban environments it is expected that the total runoff is approximately 50-75% of the total precipitation event (Haase, 2009; Mitchell et al., 2003; Van de Ven and Voortman, 1985). Comparing the complete flood wave and volumetric precipitation gives an lower runoff than could be expected.

When taking a closer look at the second flood wave – from 10:00 EAT onwards – it becomes clear that the this discharge peak contains 93% [90-95] of the total discharge volume. When comparing these with the second and third precipitation event – from 08:30 till 16:00 EAT, containing 65% of the total volumetric precipitation, which correspondent with $497.39 \cdot 10^3$ m³ – the runoff coefficient rises up to 53% [35-68], which comes closer to the values found in the literature. The complete comparison is shown in Figure 6.4b using the different post-processing steps.

6.4. Summary

Using a digital elevation map and the locations of man-made drainage systems, the contributing catchment area for the discharge gauging site is estimated, which is approximately $5.69 \cdot 10^6$ m². Using this area and the precipitation data of a nearby meteorological station an estimation of the volumetric precipitation can be made. The total volumetric precipitation is $P = 770.86 \cdot 10^3$ m³.

Comparing the total volumetric precipitation with the discharges obtained at the downstream gauging station provides an estimate for the total runoff in the catchment area. These percentages give an estimation of the validity of the discharges obtained using the LSPIV method. For high density areas it is expected that the runoff coefficient is approximately 50-75% (Haase, 2009; Mitchell et al., 2003; Van de Ven and Voortman, 1985).

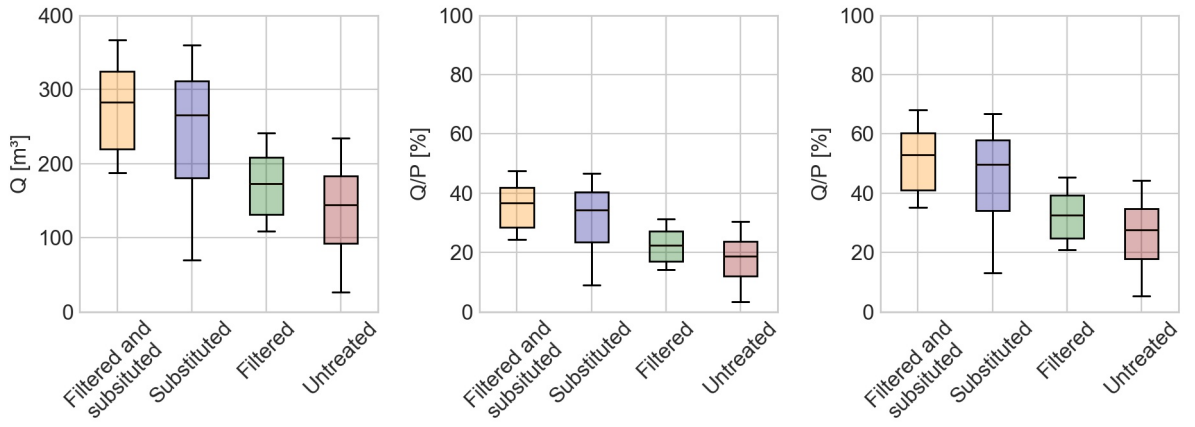

(a) Total discharge volumes

(b) Total discharge volumes as part of the total volumetric precipitation

(c) Discharge volumes of the second wave as part of the second and third precipitation events

Figure 6.4: (a) Distributions of the total discharge volumes for the four post-processing steps and (b) their part of the total volumetric precipitation (Q/P) where $P = 770.86 \cdot 10^3$ m³. In Figure (c) the discharge volumes of the second wave are compared with the volumetric precipitation of the second and third event ($P = 497.39 \cdot 10^3$ m³).

When comparing the complete flood wave with the total volumetric precipitation, the runoff coefficient is estimated to be 37% [24-48] – for the complete post-processed results – which is much lower than the expected runoff coefficient. This underestimation is probably related to local buffers – e.g. local pools, roof surfaces, rainwater harvesting storage tanks, and soil storage capacity – as there was a long dry period prior to the precipitation event and the initial storage in these buffers was therefore limited.

When only comparing the second and third precipitation event (*see* Figure 6.2) with the second flood wave, the runoff coefficient increases to 53% [35-68] as by this point, most of the buffers were filled.

Despite the runoff coefficient being within the range as provided by literature, the total runoff is probably still at the lower side of the expected percentage, taking the uncertainty bandwidth into account. This can be caused by three reasons: (1) the discharges obtained using the LSPIV method is an underestimation of the actual discharges – the uncertainties related to the method were discussed in Chapter 5 – (2) the total volumetric precipitation is an overestimation due to the assumption that the precipitation monitored at the TAHMO weather station is uniformly distributed over the catchment, or (3) due to an overestimation of the contributing catchment. However, the offset between the found and theoretical runoff coefficient is acceptable and proves that the LSPIV method is at least able to provide a rough estimation of the discharges during a flood wave.

7

Discussion

The aim of this report is to answer the question whether LSPIV is a feasible method for monitoring flood waves in equatorial fast response urban streams. In this chapter the feasibility is discussed by addressing several practical issues related to setting up a gauging site (*see* Section 7.1), the processing methods (*see* Section 7.2), and the quality and usefulness of the results (*see* Section 7.3). Lastly, in Section 7.4 the implementation of the LSPIV method in different use cases are discussed. In each section, the LSPIV method is discussed in comparison with other conventional methods for river gauging.

7.1. Gauging site setup

Within urban areas, implementing a gauging site for continuous measurements at a urban stream can be a difficult task when using conventional gauging methods. Building permanent structures in these areas are not always an option due to construction and maintenance costs, dimensions, presence of debris, and environmental impact. Other option is estimating discharges using water level gauges and rating curves, based on several point measurements. For both methods, there is a need for access to an energy source. Furthermore, as sensors need to be placed close to the stream, these sites can be prone to vandalism and theft. The LSPIV method provides the possibility to acquire flow velocities from a distance from the stream over a large area. When placed on a closed compound access to energy and safety from vandalism is ensured. Besides this, using the LSPIV method it is possible to estimate discharges at locations where conventional methods have trouble acquiring measurements or even never could be established, like at floodplains with dense vegetation. Besides this, as the LSPIV method does not need direct contact with the stream, discharges can be estimated even during the peaks of the flood waves. Rating curves established using traditional methods usually lack sufficient data points at these water levels due to practical and safety reasons.

Setting up a fixed-in-place LSPIV gauging station – either for short or long term purposes – requires several considerations regarding camera position. Most optimally, the imagery is captured at an inclined angle between 15°and 30°as this will decrease the impact of uncertainties or errors introduced by the orthorectification process and distortions due to camera movement (Harpold et al., 2006; Kim, 2006; Sutarto, 2015). The 50°incline of the CCTV at the Chuo Kikuu is larger than recommended, but the results only get increasingly error prone at an angle of 85°, as is stated by Kim (2006). Therefore it is expected that the impact of the angle of the CCTV is minimal.

Furthermore, the following requirements should be taken into account when setting up a LSPIV gauging station to ensure the collection of usable data: (1) access to a reliable energy source to ensure continuous data collection if needed, (2) resilience against different weather conditions – e.g. camera lens protection against lens flares, droplets, and fog – and (3) easy access to the acquired data, preferably by saving the imagery online.

In this study, it is found that placing ground control points (GCPs) located in the stream itself are not a suitable solution. Especially in streams with large pieces of debris floating by during flood waves – like the

Chuo Kikuu – these GCPs will be exposed to large stresses due to that debris, resulting in the necessity for maintenance, or even replacements. If the camera is placed at the side of a stream and therefore facing the stream under an angle, multiple GCPs – at least six and preferably more – are needed to apply orthorectification. Four GCPs is not feasible in this case, as they need to be in the same plane as the water surface during each stage of the flood wave. For the process of orthorectification with six or more GCPs, an algorithm that uses x, y and z location coordinates should be applied. Nevertheless, the orthorectification could still be made entirely automated with only the water level as parameter – under the assumption that the camera is static.

Preferably, a gauging site has a clear view on the entire stream and floodplains. At the gauging site along the Chuo Kikuu, large parts of the stream were not observable due to the presence of dense vegetation, which will have lead to underestimations of the discharges. Besides this, the stream should contain enough – at least 10% of the surface area – visible traceable items. The study site in Dar es Salaam provided seeding in the form of debris. Especially during the ascending part of a flood wave – when most of the debris is flushed away through the the drainage systems into the stream – the LSPIV method seemed to provide feasible results. However, due to the lack of debris in the descending part of the flood wave an underestimation of the flow velocities – and therefore discharges – may occur. This underestimation is as much as dealt with by replacing flow velocities at under-seeded sections with velocities based on a physically based relationship between the water depth and surface flow velocity in the post-processing method.

7.2. Processing methods

The processing methods of the LSPIV approach can be divided into three groups: (1) image preparation, (2) PIV processing, and (3) post-processing. The image preparation is dependent on the setup of the gauging site, but also weather conditions and the moment of day could influence the process. In this research, there has not been the opportunity to investigate the impact of the latter two on the accuracy and precision of the LSPIV method. However – as flood waves can be expected during night time, or during heavy precipitation events – it would be good to know the impact of these conditions on the image preparation process and post-processing results. Especially the contrast- and gamma correction should be adjusted to obtain imagery which are suitable for further processing.

This study performed the majority of the PIV processing using OpenPIV in the Python environment. The use of OpenPIV provides the opportunity to do all LSPIV steps – from image preparation using OpenCV to post-processing – within one programming language, and provides the possibility to apply changes to the PIV processing and post-processing if necessary. Furthermore, the use of this library offers the prospect to operationalize the flow observation method by providing the possibility to workflow which will acquire videos at a set interval. Besides this, the raw Python environment provides the possibility to quickly alter parameters to optimize the PIV processing results. However, the use of this processing requires knowledge about Python and therefore reduces the accessibility. For instance Fudaa-LSPIV provides an interface, which gives the opportunity to apply LSPIV without having the coding knowledge. The development of such an interface for Python could increase its usability.

The post-processing applied in this report provides the possibility to reduce the uncertainty bandwidth through filtering by 37%, and estimating flow velocities at locations with limited seeds through the substitution process leading to an increase of 96% of the total mean discharge when both post-processing methods are applied.

However, both the filtering the filtering as the substitution process are based on arbitrary assumptions. Especially the additional filtering method – where lower flow velocities are eliminated based on their distance to the 95^{th} percentile – should be substituted by a less pragmatic approach – e.g. by using Otsu's thresholding. Moreover, several assumptions are made regarding the substitution process – i.e. the vertical logarithmic progression relationship of the surface flow velocities is uniform over the whole width of the stream, and the relationship is similar for the ascending and descending part of the flood wave. This process could be refined through establishing different vertical progression relationships for different cross-sectional sections and for the ascending and descending part of the flood wave. As during the descending part of the flood wave limited seeds are present, an acceptable relationship can only be made based on results from multiple flood events.

7.3. Quality of the results

The methodology provided in this thesis shows the possibility to set up a gauging site to gather stream imagery, process the imagery following the LSPIV method, and to estimate discharges using the obtained surface flow velocities and local bathymetry. This process still relies on empirical formulas – i.e. the conversion to depth-averaged flow velocities – and ambiguous thresholds for the filtering and substitution process. However, as the LSPIV results is capable to show the uncertainties of the results – clearly visible in the ranges of flow velocities at different cross-sectional sections – it is known what the precision of the flow velocity results are: for each flow velocity the correlation is known and standard deviation can be determined. The precision could be further improved by optimising the post processing. For traditional gauging methods it is much harder to acquire the precision of a result, as measurements are usually time and location specific – e.g. when using current meters or ADCPs – and multiple measurements are needed to establish a bandwidth of the results. Executing these measurements are often time consuming, labour intensive and sometimes not safe to execute.

The LSPIV method is able to quickly gather discharges at different water levels and estimate a rating curve containing a bandwidth of uncertainty using a single flood event. However, as it was not possible to execute validation measurements using traditional methods, it is unknown what the accuracy of the surface flow velocities and discharges at the Chuo Kikuu are. The sudden gulp salt dilution tests – which were executed during a different day – were probably flawed due to improper execution, and therefore did not provide results which are comparable with the LSPIV results.

In order to assess whether the order of results are reasonable, this research compared the discharges found using the LSPIV method with precipitation data measured at a nearby weather station. With only the use of a DEM and locations of man-made drainage systems a contributing catchment was estimated. With an runoff coefficient of 53% [35-68], the discharges found are within the range of expected values found in literature (Haase, 2009; Mitchell et al., 2003; Van de Ven and Voortman, 1985). The actual runoff is probably higher, as flows at the floodplains were not taken into account, and the actual contributing catchment probably being smaller than found within this research.

7.4. Potential implementations

As this research shows, the LSPIV method provides the possibility to assess flow behaviour and estimate discharges. The method proves to be suitable for acquiring flow velocities at locations where observations using traditional methods never could be established. Besides this, the LSPIV method provides the possibility to estimate discharges during a flood wave at regular intervals, regardless of the water level or flow velocities, during which conventional methods would require intensive labour to acquire results, if measurements are possible at all due to safety reasons as direct contact with the stream is needed – e.g. when using current meters, ADCPs, or dilution methods. However, the main requirement is for the feasibility of the LSPIV method is the presence of seeds in the form of leaves, branches, air bubbles, or debris.

The LSPIV method could be used for several applications. These applications are, among others:

- *Establishing rating curves:* This research shows that it is possible to set up a rating curve, solely based on discharges estimated during a single flood wave. Due to the possibility to acquire measurements at an high interval – which is difficult with traditional methods. Ideally, the LSPIV gauging site only has to be operational during one flood wave, after which discharges can be estimated using the water level. When the gauging site is operational continuous, changes in the rating curve could easily detected, caused by changes in the contributing catchment.
- *Creating precipitation-runoff relationships:* As established in Chapter 6, discharges can be compared with nearby monitored precipitation. Not only can this be used to assess whether the discharges found using the LSPIV method are reasonable, but it can also be used to build a precipitation-runoff relationship, when discharges during multiple precipitation events are estimated.
- *Validating runoff models:* Many runoff models need continuous discharge measurements for validation purposes. During low flows, LSPIV might not be feasible to use – due to the absence of

seeds – but during peak flows using LSPIV provides the possibility to estimate at a regular interval combined with the bands of uncertainty related to the precision. These uncertainties can be used for the estimation of flood frequencies at locations where there are limited historical records of flood peaks reaching beyond a simple precipitation-runoff relationship (Blazkova and Beven, 2002, 2004; Cameron et al., 1999).

- *Setting up a operational early warning system:* As stated in Section 1.1, the motivation for executing this research is to assess whether the LSPIV method can be used to monitor flood waves in Dar es Salaam. The city experiences multiple flooding events annually and over a million inhabitants are directly affected by these events. For the Community Water Watch project – a project to design an early warning system for the Msimbasi river – LSPIV could be used to improve their system by gathering discharges in real time. As the gauging site should be placed in an urban environment a gauging site placed near the river is prone to vandalism. A camera used for the LSPIV method can be placed from a save distance at an enclosed compound. Furthermore, due to the presence of an extensive amount of debris, sufficient seeding is present. Especially at the ascending part of a flood wave.

For each application it has to be taken into account that LSPIV can only estimate flow velocities if sufficient seeds are present, usually during flood waves. Therefore, it is advisable to only gather videos during certain events. This could be accomplished by activating the camera when at a nearby meteorlogical station precipitation is measured, or when a certain water level in the stream is reached. In Appendix A a guide for setting up a gauging station for continuous observations is provided.

8

Conclusions

This chapter will conclude each sub question based on the results obtained in the previous chapters. These conclusions will then be used to answer the main research question, which was defined as follows:

Is Large-Scale Particle Image Velocimetry a feasible method for monitoring flood waves in a stream located in an equatorial urban environment with a fast response time?

Using the following sub questions, the main research question has been addressed:

1. *What is the impact of processing methods and environmental conditions on the accuracy and precision of LSPIV and how do these results compare with conventional methods?*
2. *Can LSPIV be used for reconstructing flood waves in an equatorial fast response time urban stream?*
3. *How do discharges obtained using LSPIV relate to nearby monitored precipitation?*

8.1. Impact processing methods and environmental conditions

Using imagery from the Dommel, different processing methods and environmental conditions were compared to each other and to benchmark measurements. Comparisons were executed based on the accuracy – using the mean error (ME) and root mean squared error (RMSE) – the precision – based on the relative standard deviation (RSD). Several different processing methods were discussed: to substantiate the use of OpenPIV, this software was compared with Fudaa-LSPIV. Despite the use of different grid shapes, both results are similar in accuracy and precision. The benefits of using OpenPIV are the faster processing time and modularity. This modularity makes combining an operational automated workflow with the image preparation and post-processing easier.

Both software provide the opportunity to filter the gathered velocities based on the a correlation factor and to replace values with low correlation through interpolation of surrounding known cells. Using the filtered results provides the highest precision when dealing with few seeds (RSD=1.827), as the interpolation process is based on grid cells where no seeds are detected leading (RSD=1.871).During increased seeding densities, interpolation is a suitable method to estimate missing values, as surrounding grid cell velocities are probably based on the presence of seeds. Applying additional contrast correction can improve the visibility of seeds. However, for the different corrections the improvements were limited. It is recommended to apply contrast correction through an automated process. The most accurate flow velocities at the Dommel acquired using the LSPIV method are between the 50^{th} and 75^{th} percentile, if at least a moderate amount of seeds is found – 10% of the surface area, as is stated in literature.

Two different environmental conditions were considered in this report: seeding density and point of view. As expected, denser seeding density increases the accuracy and precision of the LSPIV method. For no artificial seeding the RSD and RMSE are 1.827 and 0.322 respectively. For extensive artificial seeding

values of 0.520 and 0.188 are found. No conclusion can be drawn on the impact of the point of view due to UAV hovering – this resulted in image deformation due to the orthorectification process – unknown impacts of lightning, and irregular seeding densities. Laboratory studies from literature show that the LSPIV method becomes increasingly error prone with inclined angles of 85°and larger. The optimal angle is between approximately 15°and 30°relative to nadir. It is recommended to use a static camera and to make sure that the complete stream is within the line of sight.

8.2. Surveying a flood wave using LSPIV

This report shows that it is possible to reconstruct flood waves using LSPIV, by processing multiple videos. As a result of this processing, it is possible to estimate flow velocities over a large area, including uncertainties related to their precision. Using low flow filtering, this uncertainty bandwidth can be reduced with 37%. Due to the placement of the camera and the presence of dense vegetation, blind spots can be present in the scene. This results in certain areas in the scene, that are not resolved by LSPIV – i.e. no flow velocity estimations can be made. At locations where visibility is limited, or no seeds are present, the substitution process provides an option to make an educated guess to estimate the actual flow velocities. As this is not possible for the floodplain area, it is assumed that flows do not occur there. This may have led to underestimation of discharges during increased water levels.

During the descending part of the flood wave limited to no seeds were detected, which will lead to an underestimation of the flow velocities. As mentioned, these flow velocities are estimated using the substitution process. The vertical logarithmic progression relationship is mainly based on measurements in the ascending part of the flood wave – when most of the seeds in the form of debris passed by. Therefore it is assumed that this substitution method overestimates the flow velocities in the descending part of the flood wave, as lower flow velocities are expected in the descending part of the flood wave than in the ascending part due to hysteresis.

The depth-averaged flow velocities are determined using an empirical based coefficient. This coefficient is applied under the assumption that the vertical profile is uniform over the whole width of the stream and over time. The coefficient could not be estimated based on local measurements, and therefore based on similar cases in literature.

It is expected that at the ascending part of the flood wave – when most seeds are found, and the floodplain level is not yet reached – discharges with the highest accuracy are found. During the period water levels are higher than the flood plane level, it is expected that the found discharges are an underestimation of the actual discharges, as flow velocities within the flood plane area are not taken into account. During the final descending part, discharges are probably overestimated due to the substitution process. Applying both the filtering as the substitution process on the data acquired at the Chuo Kikuu, increased the total mean discharge with 96% relative to the untreated results and decreased the bandwidth with 37%.

8.3. Comparing precipitation and discharges

Comparing the total volumetric precipitation with the discharge volume of the complete flood wave showed that the LSPIV method measured 19% [3-30] runoff when no post-processing was applied, and 36% [24-48] when the complete post-processing process – through filtering and substitution – was applied. As during the first precipitation event the least runoff is expected due to filling of local storage – e.g. local pools, roof surfaces, and soil storage capacity – this report also examined the runoff caused only by the second and third precipitation event. Comparing this volumetric precipitation with the second flood wave observed, showed runoff percentages of 28% [5-44] when no additional post-processing was applied, and 53% [35-68] when the complete post-processing was used. For similar urban areas runoff coefficients ranging between 50-75% are expected. The runoff obtained after post-processing falls within this range. However, as the total discharges might be underestimated, and the catchment area might be overestimated, the runoff coefficient found is probably an underestimation.

8.4. Using LSPIV for monitoring flood waves

In conclusion, this study showed that LSPIV is a feasible method for monitoring flood waves in equatorial method for monitoring flood waves in equatorial urban streams with fast response times. When sufficient

seeding is present, obtained surface flow velocities have reasonable accuracy and precision. Discharges obtained using the LSPIV method fall within the range of expected runoff percentages. However, additional post-processing is recommended, which will lead to a reduction in precision uncertainties, and an increase of the mean discharges. Unlike most conventional discharge gauging methods, LSPIV gives the possibility to gather data at short intervals with little effort and without the need to have physical contact with the stream. Especially at streams with fast response times – where sudden high flow velocities can be observed – it is unsafe to be close to a stream. Using LSPIV therefore provides the possibility to quickly and safely generate rating curves including points at increased water levels and at regular intervals. The understanding of the uncertainties in the rating curve further increases its applicability, for instance in model calibration.

The post-processing of the LSPIV method applied in this study shows that additional processing will lead to a lower band of uncertainty within the method itself, and provides a opportunity for estimating flow velocities at locations where no flow velocities are found – due to the lack of seeds, or due to obscuration. However, it is yet unclear how the complete process compares with measurements using conventional methods. Therefore, the method's accuracy is still unclear.

The optimal angle to place the camera is at an 15°to 30°incline relative to nadir, as is stated in literature. From angles larger than 85°the method becomes increasingly error prone. The stream should contain a moderate amount of seeds to acquire reasonable results – approximately 10% of the surface area, as stated in literature. Through PIV processing, flow velocities below a certain correlation factor should be removed to eliminate as much noise as possible prior the post-processing. Thereafter, additional filtering should be applied to remove lower values, and flow velocity substitution could be applied based on a the vertical logarithmic progression of the surface flow velocities. To acquire depth-averaged flow velocities, the empirical depth-average coefficient is used. This coefficient causes the most uncertainties related to the discharges.

LSPIV is a feasible method to be applied in urban regions where there is a need for continuous gauging of flood waves. The possibility to monitor a stream from a distance – which ensures access to power and safety from vandalism – results in the possibility to observe complete flood waves at regular intervals without the direct need for contact with the water. For Dar es Salaam, this method opens doors for continuous and secure stream monitoring, at low cost, with local devices.

9

Recommendations

In this last chapter a summary of ideas for further research is provided. These recommendations relate to the setup of the gauging site, ideas for implementation, and changes in the post-processing steps. In Appendix A a recommendation for the application of the full LSPIV method is presented.

Gauging site and implementations

- *Ground control points and orthorectification:* For the orthorectification process at both the Dommel and the Chuo Kikuu four GCPs were used. To improve the applicability of the method, the use of six (or more) GCPs should be considered. Using 3-dimensional coordinates to orthorectify imagery needs a different process, which should be made suitable for Python. An suitable option is the pinhole model. This method is used in Fudaa-LSPIV and explained by Jodeau et al. (2008).
- *Upscaling:* It would be interesting to acquire discharge information at a larger river over a longer time. The equipment at the Chuo Kikuu was taken offline after the flood wave. Gathering more different flood waves could result in a more accurate rating curve and the creation of a precipitation-discharge relationship.
- *Validation:* Unfortunately, validation measurements were not performed during the flood wave observed. Therefore, the accuracy of the discharge determinations could not be given. Executing validation measurements – if possible during different stages of the flood wave – would fill this gap.
- *Light intensities:* The complete flood wave observed at the Chuo Kikuu took place during daytime, with bright conditions. It would be interesting how LSPIV performs based on darker imagery or night time imagery, and how the image manipulation process – regarding gray scaling, contrast- and gamma correction – should be changed. Placing an additional light source could be a solution for increasing visibility of seeds during the night.
- *Depth-average coefficient:* The depth-average coefficient is within this approach the factor causing the highest uncertainties. The depth-averaged flow velocities should be determined either through thorough understanding of the evolvement of the coefficient over space and time, or by looking for an alternative approach.
- *User-friendly interface* most of the calculations and processing was performed in Python. Currently the different parts of the LSPIV method are found in different scripts. To be able to use the LSPIV method based on Python, the codes should be made uniform and the scripts applicable without having in-depth knowledge of Python – or coding. Besides this, wide accessibility of the coding should be made possible through the development of a Python class, that can be flexibly called by a user.

Post-processing

- *Filtering:* The filtering process in this research is based on an arbitrary threshold. At the locations where filtering should be applied, observations seem to follow a bimodal distribution. Removing

the lower distribution – e.g. with the use of Otsu's thresholding (Otsu, 1979) – could improve the filtering process and make it less arbitrary.

- *Substitution:* Applying substitution of flow velocities or not is now based on an arbitrary threshold. Improving or changing this threshold could improve the logicalness of the substitution process.

Bibliography

Adnan, S. G. and Kreibich, H. An evaluation of disaster risk reduction (DRR) approaches for coastal delta cities: a comparative analysis. *Natural Hazards*, 83(2):1257–1278, sep 2016. ISSN 15730840. doi: 10.1007/s11069-016-2388-8.

Adrian, R. J. Particle-Imaging Techniques for Experimental Fluid Mechanics. *Annual Review of Fluid Mechanics*, 23(1):261–304, 1991. ISSN 0066-4189. doi: 10.1146/annurev.fl.23.010191.001401.

Arnell, N. W. Climate change and global water resources. *Global Environmental Change*, 9(SUPPL.): S31–S49, 1999. ISSN 09593780. doi: 10.1016/S0959-3780(99)00017-5.

Arneth, A., Barbosa, H., Benton, T., Calvin, K., Calvo, E., Connors, S., Cowie, A., Davin, E., Denton, F., van Diemen, R., Driouech, F., Elbehri, A., Evans, J., Ferrat, M., Harold, J., Haughey, E., Herrero, M., House, J., Howden, M., Hurlbert, M., Jia, G., Gabriel, T. J., Krishnaswamy, J., Kurz, W., Lennard, C., Myeong, S., Mahmoud, N., Delmotte, V. M., Mbow, C., McElwee, P., Mirzabaev, A., Morelli, A., Moufouma-Okia, W., Nedjraoui, D., Neogi, S., Nkem, J., Noblet-Ducoudré, N. D., Pathak, L. O. M., Petzold, J., Pichs-Madruga, R., Poloczanska, E., Popp, A., Pörtner, H.-O., Pereira, J. P., Pradhan, P., Reisinger, A., Roberts, D. C., Rosenzweig, C., Rounsevell, M., Shevliakova, E., Shukla, P., Skea, J., Slade, R., Smith, P., Sokona, Y., Sonwa, D. J., Soussana, J.-F., Tubiello, F., Verchot, L., Warner, K., Weyer, N., Wu, J., Yassaa, N., Zhai, P., and Zommers, Z. Climate Change and Land: Summary for Policymakers. *An IPCC Special Report on climate change, desertification, land degradation, sustainable land management, food security, and greenhouse gas fluxes in terrestrial ecosystems*, page 43, 2019. doi: 10.4337/9781784710644.

Aya, S., Fujita, I., and Yagyu, M. Field-Observation of Flood in a River by Video Image Analysis. *Proceedings of Hydraulic Engineering*, 39:447–452, 1995. ISSN 0916-7374. doi: 10.2208/prohe.39.447.

Beck, H. E., Zimmermann, N. E., McVicar, T. R., Vergopolan, N., Berg, A., and Wood, E. F. Present and future köppen-geiger climate classification maps at 1-km resolution. *Scientific Data*, 5, 2018. ISSN 20524463. doi: 10.1038/sdata.2018.214. URL /pmc/articles/PMC6207062/?report=abstracthttps://www.ncbi.nlm.nih.gov/pmc/articles/PMC6207062/.

Benacchio, V., Piégay, H., Buffin-Bélanger, T., and Vaudor, L. A new methodology for monitoring wood fluxes in rivers using a ground camera: Potential and limits. *Geomorphology*, 279:44–58, 2017. ISSN 0169555X. doi: 10.1016/j.geomorph.2016.07.019. URL https://www.sciencedirect.com/science/article/pii/S0169555X16305931.

Blazkova, S. and Beven, K. Flood frequency estimation by continuous simulation for a catchment treated as ungauged (with uncertainty). *Water Resources Research*, 38(8):14–1–14–14, aug 2002. ISSN 00431397. doi: 10.1029/2001wr000500.

Blazkova, S. and Beven, K. Flood frequency estimation by continuous simulation of subcatchment rainfalls and discharges with the aim of improving dam safety assessment in a large basin in the Czech Republic. *Journal of Hydrology*, 292(1-4):153–172, jun 2004. ISSN 00221694. doi: 10.1016/j.jhydrol.2003.12.025.

Bradley, A. A., Kruger, A., Meselhe, E. A., and Muste, M. V. I. Flow measurement in streams using video imagery. *Water Resources Research*, 38(12):51–1–51–8, 2002. ISSN 0043-1397. doi: 10.1029/2002wr001317.

Cameron, D. S., Beven, K. J., Tawn, J., Blazkova, S., and Naden, P. Flood frequency estimation by continuous simulation for a gauged upland catchment (with uncertainty). *Journal of Hydrology*, 219 (3-4):169–187, jul 1999. ISSN 00221694. doi: 10.1016/S0022-1694(99)00057-8.

Chow, V. T., Maidment, D. R., and Mays, L. W. Applied hydrology. *Journal of Hydrology*, 6(2):224–225, 1968. ISSN 00221694. doi: 10.1016/0022-1694(68)90169-8.

Collins, M. J. and Emery, W. J. A computational method for estimating sea ice motion in sequential Seasat synthetic aperture radar imagery by matched filtering. *Journal of Geophysical Research*, 93 C(8):9241–9251, aug 1988. ISSN 01480227. doi: 10.1029/jc093ic08p09241. URL https://agupubs.onlinelibrary.wiley.com/doi/full/10.1029/JC093iC08p09241https://agupubs.onlinelibrary.wiley.com/doi/abs/10.1029/JC093iC08p09241https://agupubs.onlinelibrary.wiley.com/doi/10.1029/JC093iC08p09241.

Dircke, P., Aerets, J., and Molenaar, A. *Connecting Delta Cities: Sharing Knowledge and Working on Adaptation to Climate Change*. Connecting Delta Cities, 2010. ISBN 9789081606714. URL https://research.vu.nl/en/publications/connecting-delta-cities-sharing-knowledge-and-working-on-adaptati.

Dramais, G., Le Coz, J., Camenen, B., and Hauet, A. Advantages of a mobile LSPIV method for measuring flood discharges and improving stage-discharge curves. *Journal of Hydro-Environment Research*, 5(4):301–312, 2011. ISSN 15706443. doi: 10.1016/j.jher.2010.12.005.

Eltner, A., Sardemann, H., and Grundmann, J. Technical Note: Flow velocity and discharge measurement in rivers using terrestrial and UAV imagery. *Hydrology and Earth System Sciences Discussions*, 24(3):1–29, 2019. ISSN 1812-2116. doi: 10.5194/hess-2019-289.

Fekete, B. M., Looser, U., Pietroniro, A., and Robarts, R. D. Rationale for monitoring discharge on the ground. *Journal of Hydrometeorology*, 13(6):1977–1986, 2012. ISSN 1525755X. doi: 10.1175/JHM-D-11-0126.1.

Fryer, J. G. and Brown, D. C. Lens distortion for close-range photogrammetry., 1986. URL https://www.researchgate.net/publication/241333736.

Fujita, I. and Komura, S. Application of Video Image Analysis for Measurements of River-Surface Flows. *Proceedings of Hydraulic Engineering*, 38:733–738, 1994. ISSN 0916-7374. doi: 10.2208/prohe.38.733.

Fujita, I., Muste, M., and Kruger, A. Large-scale particle image velocimetry for flow analysis in hydraulic engineering applications. *Journal of Hydraulic Research*, 36(3):397–414, 1998. ISSN 00221686. doi: 10.1080/00221689809498626.

Fujita, I., Watanabe, H., and Tsubaki, R. Development of a non-intrusive and efficient flow monitoring technique: The space-time image velocimetry (STIV). *International Journal of River Basin Management*, 5(2):105–114, 2007. ISSN 18142060. doi: 10.1080/15715124.2007.9635310. URL https://iahr.tandfonline.com/doi/abs/10.1080/15715124.2007.9635310.

Gore, J. A. and Banning, J. *Discharge Measurements and Streamflow Analysis*, volume 1. Elsevier Inc., 2017. ISBN 9780124165588. doi: 10.1016/B978-0-12-416558-8.00003-2. URL http://dx.doi.org/10.1016/B978-0-12-416558-8.00003-2.

Guillén, N. F., Patalano, A., García, C. M., and Bertoni, J. C. Use of LSPIV in assessing urban flash flood vulnerability. *Natural Hazards*, 87(1):383–394, 2017. ISSN 15730840. doi: 10.1007/s11069-017-2768-8.

Haase, D. Effects of urbanisation on the water balance - A long-term trajectory. *Environmental Impact Assessment Review*, 29(4):211–219, jul 2009. ISSN 01959255. doi: 10.1016/j.eiar.2009.01.002.

Hanson, S., Nicholls, R., Ranger, N., Hallegatte, S., Corfee-Morlot, J., Herweijer, C., and Chateau, J. A global ranking of port cities with high exposure to climate extremes. *Climatic Change*, 104(1):89–111, dec 2011. ISSN 01650009. doi: 10.1007/s10584-010-9977-4.

Harpold, A. A., Mostaghimi, S., Vlachos, P. P., Brannan, K., and Dillaha, T. Stream discharge measurement using a large-scale particle image velocimetry (LSPIV) prototype. *Transactions of the ASABE*, 49(6):1791–1805, 2006. ISSN 21510032. doi: 10.13031/2013.22300.

Hauet, A., Kruger, A., Krajewski, W. F., Bradley, A., Muste, M., Creutin, J.-D., and Wilson, M. Experimental System for Real-Time Discharge Estimation Using an Image-Based Method. *Journal of Hydrologic Engineering*, 0699(June 2008):1146–1157, 2008. doi: 10.1061/(ASCE)1084-0699(2008)13.

Huntington, T. G. Evidence for intensification of the global water cycle: Review and synthesis. *Journal of Hydrology*, 319(1-4):83–95, mar 2006. ISSN 00221694. doi: 10.1016/j.jhydrol.2005.07.003.

Jodeau, M., Hauet, A., Paquier, A., Le Coz, J., and Dramais, G. Application and evaluation of LS-PIV technique for the monitoring of river surface velocities in high flow conditions. *Flow Measurement and Instrumentation*, 19(2):117–127, apr 2008. ISSN 09555986. doi: 10.1016/j.flowmeasinst.2007.11.004.

Jonkman, S. N. Global perspectives on loss of human life caused by floods. *Natural Hazards*, 34(2):151–175, 2005. ISSN 0921030X. doi: 10.1007/s11069-004-8891-3.

Kantoush, S. A., Schleiss, A. J., Sumi, T., and Murasaki, M. LSPIV implementation for environmental flow in various laboratory and field cases. *Journal of Hydro-Environment Research*, 5(4):263–276, dec 2011. ISSN 15706443. doi: 10.1016/j.jher.2011.07.002.

Kim, Y. *Uncertainty analysis for non-intrusive measurement of river discharge using image velocimetry*. PhD thesis, The University of Iowa, 2006.

Kompenhans, J., Raffel, M., Dieterle, L., Dewhirst, T., Vollmers, H., Ehrenfried, K., Willert, C., Pengel, K., Kähler, C., Schröder, A., and Ronneberger, O. Particle Image Velocimetry in Aerodynamics: Technology and Applications in Wind Tunnels. *Journal of Visualization*, 2(3,4):229–244, jan 2000. ISSN 1343-8875.

Krueger, I., Ayala, L. M., and van Driel, W. F. Delta Alliance Young Professionals Award: Innovative solutions for delta challenges worldwide. Technical report, Wageningen-Delft: Delta Alliance, 2012.

Kummu, M., de Moel, H., Ward, P. J., and Varis, O. How close do we live to water? a global analysis of population distance to freshwater bodies. *PLoS ONE*, 6(6), 2011. ISSN 19326203. doi: 10.1371/journal.pone.0020578.

Le Coz, J., Hauet, A., Pierrefeu, G., Dramais, G., and Camenen, B. Performance of image-based velocimetry (LSPIV) applied to flash-flood discharge measurements in Mediterranean rivers. *Journal of Hydrology*, 394(1-2):42–52, nov 2010. ISSN 00221694. doi: 10.1016/j.jhydrol.2010.05.049.

Le Coz, J., Jodeau, M., Hauet, A., Marchand, B., and Le Boursicaud, R. Image-based velocity and discharge measurements in field and laboratory river engineering studies using the free FUDAA-LSPIV software. In *Proceedings of the International Conference on Fluvial Hydraulics, RIVER FLOW 2014*, pages 1961–1967, 2014. ISBN 9781138026742. doi: 10.1201/b17133-262. URL http://www.envirodiy.org/wp-content/uploads/2016/02/lecoz{_}RiverFlow2014.pdf.

Leese, J. A., Novak, C. S., and Clark, B. B. An Automated Technique for Obtaining Cloud Motion from Geosynchronous Satellite Data Using Cross Correlation, 1971. ISSN 0021-8952.

Lewis, Q. W., Lindroth, E. M., and Rhoads, B. L. Integrating unmanned aerial systems and LSPIV for rapid, cost-effective stream gauging. *Journal of Hydrology*, 560:230–246, may 2018. ISSN 00221694. doi: 10.1016/j.jhydrol.2018.03.008.

McCool, S. F., Clark, R. N., and Stankey, G. H. Water and people: challenges at the interface of symbolic and utilitarian values. Technical report, US Department of Agriculture, Forest Service, Pacific Northwest Research Station, 2008. URL http://www.fs.fed.us/pnw/pubs/pnw{_}gtr729.pdf.

McGranahan, G., Balk, D., and Anderson, B. The rising tide: assessing the risks of climate change and human settlements in low elevation coastal zones. *Environment and Urbanization*, 19(1):17–37, apr 2007. ISSN 0956-2478. doi: 10.1177/0956247807076960. URL http://journals.sagepub.com/doi/10.1177/0956247807076960.

Mitchell, V. G., McMahon, T. A., and Mein, R. G. Components of the Total Water Balance of an Urban Catchment, dec 2003. ISSN 0364152X.

Muste, M., Fujita, I., and Hauet, A. Large-scale particle image velocimetry for measurements in riverine environments. *Water Resources Research*, 46(4), apr 2008. ISSN 00431397. doi: 10.1029/2008WR006950.

Muste, M., Fujita, I., and Hauet, A. Large-scale particle image velocimetry for measurements in riverine environments. *Water Resources Research*, 46(4):1–14, 2010. ISSN 00431397. doi: 10.1029/2008WR006950.

Neumann, B., Vafeidis, A. T., Zimmermann, J., and Nicholls, R. J. Future Coastal Population Growth and Exposure to Sea-Level Rise and Coastal Flooding - A Global Assessment. *PLOS ONE*, 10 (3):e0118571, mar 2015. ISSN 1932-6203. doi: 10.1371/journal.pone.0118571. URL https://dx.plos.org/10.1371/journal.pone.0118571.

Nicholls, R. J., Brown, S., Goodwin, P., Wahl, T., Lowe, J., Solan, M., Godbold, J. A., Haigh, I. D., Lincke, D., Hinkel, J., Wolf, C., and Merkens, J. L. Stabilization of global temperature at 1.5°C and 2.0°C: Implications for coastal areas. *Philosophical Transactions of the Royal Society A: Mathematical, Physical and Engineering Sciences*, 376(2119), may 2018. ISSN 1364503X. doi: 10.1098/rsta.2016.0448.

Osorio-Cano, J. D., Osorio, A. F., and Medina, R. A method for extracting surface flow velocities and discharge volumes from video images in laboratory. *Flow Measurement and Instrumentation*, 33:188–196, oct 2013. ISSN 09555986. doi: 10.1016/j.flowmeasinst.2013.07.009.

Otsu, N. A Threshold Selection Method from Gray-Level Histograms. *IEEE Transactions on Systems, Man, and Cybernetics*, 9(1):62–66, jan 1979. ISSN 2168-2909. doi: 10.1109/TSMC.1979.4310076.

Oxford University Press. Accuracy, 1989a.

Oxford University Press. Precision, 1989b.

Patalano, A., García, C. M., and Rodríguez, A. Rectification of Image Velocity Results (RIVeR): A simple and user-friendly toolbox for large scale water surface Particle Image Velocimetry (PIV) and Particle Tracking Velocimetry (PTV). *Computers and Geosciences*, 109(July):323–330, 2017. ISSN 00983004. doi: 10.1016/j.cageo.2017.07.009.

Probst, J. L. and Tardy, Y. Long range streamflow and world continental runoff fluctuations since the beginning of this century. *Journal of Hydrology*, 94(3-4):289–311, oct 1987. ISSN 00221694. doi: 10.1016/0022-1694(87)90057-6.

Ran, Q.-h., Li, W., Liao, Q., Tang, H.-l., and Wang, M.-y. Application of an automated LSPIV system in a mountainous stream for continuous flood flow measurements. *Hydrological Processes*, 30(17): 3014–3029, aug 2016. ISSN 08856087. doi: 10.1002/hyp.10836. URL http://doi.wiley.com/10.1002/hyp.10836.

Ruhi, A., Messager, M. L., and Olden, J. D. Tracking the pulse of the Earth's fresh waters. *Nature Sustainability*, 1(4):198–203, 2018. ISSN 23989629. doi: 10.1038/s41893-018-0047-7. URL http://dx.doi.org/10.1038/s41893-018-0047-7.

Stumpf, A., Augereau, E., Delacourt, C., and Bonnier, J. Photogrammetric discharge monitoring of small tropical mountain rivers: A case study at Rivière des Pluies, Réunion Island. *Water Resources Research*, 52(6):4550–4570, 2016. ISSN 1093-474X. doi: 10.1002/2015WR018292.

Sutarto, T. E. Application of large scale particle image velocimetry (LSPIV) to identify flow pattern in a channel. *Procedia Engineering*, 125:213–219, 2015. ISSN 18777058. doi: 10.1016/j.proeng.2015.11.031. URL http://dx.doi.org/10.1016/j.proeng.2015.11.031.

Tauro, F., Piscopia, R., and Grimaldi, S. Streamflow Observations From Cameras: Large-Scale Particle Image Velocimetry or Particle Tracking Velocimetry? *Water Resources Research*, 53(12):10374–10394, 2017. ISSN 19447973. doi: 10.1002/2017WR020848.

Tauro, F., Grimaldi, S., and Porfiri, M. Unraveling flow patterns through nonlinear manifold learning. *PLoS ONE*, 9(3):91131, mar 2014a. ISSN 19326203. doi: 10.1371/journal.pone.0091131. URL www.plosone.org.

Tauro, F., Porfiri, M., and Grimaldi, S. Orienting the camera and firing lasers to enhance large scale particle image velocimetry for streamflow monitoring. *Water Resources Research*, 50(9):7470–7483, 2014b. ISSN 1093-474X. doi: 10.1111/j.1752-1688.1969.tb04897.x.

Tauro, F., Olivieri, G., Petroselli, A., Porfiri, M., and Grimaldi, S. Flow monitoring with a camera: a case study on a flood event in the Tiber River. *Environmental Monitoring and Assessment*, 04(4):99–132, 2016a. ISSN 15732959. doi: 10.4236/cus.2016.43021. URL http://dx.doi.org/10.1016/B978-0-08-100412-8.00001-2.

Tauro, F., Petroselli, A., and Arcangeletti, E. Assessment of drone-based surface flow observations. *Hydrological Processes*, 30(7):1114–1130, mar 2016b. ISSN 08856087. doi: 10.1002/hyp.10698. URL http://doi.wiley.com/10.1002/hyp.10698.

Tauro, F., Porfiri, M., and Grimaldi, S. Surface flow measurements from drones. *Journal of Hydrology*, 540:240–245, 2016c. ISSN 00221694. doi: 10.1016/j.jhydrol.2016.06.012.

Tauro, F., Selker, J., Van De Giesen, N., Abrate, T., Uijlenhoet, R., Porfiri, M., Manfreda, S., Caylor, K., Moramarco, T., Benveniste, J., Ciraolo, G., Estes, L., Domeneghetti, A., Perks, M. T., Corbari, C., Rabiei, E., Ravazzani, G., Bogena, H., Harfouche, A., Broccai, L., Maltese, A., Wickert, A., Tarpanelli, A., Good, S., Lopez Alcala, J. M., Petroselli, A., Cudennec, C., Blume, T., Hut, R., and Grimaldia, S. Measurements and observations in the XXI century (MOXXI): Innovation and multi-disciplinarity to sense the hydrological cycle. *Hydrological Sciences Journal*, 63(2):169–196, 2018. ISSN 21503435. doi: 10.1080/02626667.2017.1420191. URL https://doi.org/10.1080/02626667.2017.1420191.

Tauro, F., Piscopia, R., and Grimaldi, S. PTV-Stream: A simplified particle tracking velocimetry framework for stream surface flow monitoring. *Catena*, 172(May 2018):378–386, 2019. ISSN 03418162. doi: 10.1016/j.catena.2018.09.009.

Taylor, Z. J., Gurka, R., Kopp, G. A., and Liberzon, A. Long-duration time-resolved PIV to study unsteady aerodynamics. *IEEE Transactions on Instrumentation and Measurement*, 59(12):3262–3269, dec 2010. ISSN 00189456. doi: 10.1109/TIM.2010.2047149.

Theule, J. I., Crema, S., Marchi, L., Cavalli, M., and Comiti, F. Exploiting LSPIV to assess debris-flow velocities in the field. *Natural Hazards and Earth System Sciences*, 18(1):1–13, 2018. ISSN 16849981. doi: 10.5194/nhess-18-1-2018. URL https://doi.org/10.5194/nhess-18-1-2018.

Thielicke, W. and Stamhuis, E. J. PIVlab – Towards User-friendly, Affordable and Accurate Digital Particle Image Velocimetry in MATLAB. *Journal of Open Research Software*, 2(1), oct 2014. ISSN 2049-9647. doi: 10.5334/jors.bl. URL http://openresearchsoftware.metajnl.com/articles/10.5334/jors.bl/.

Todd, G., Msuya, I., Levira, F., and Moshi, I. City Profile: Dar es Salaam, Tanzania. *Environment and Urbanization ASIA*, 10(2):193–215, 2019. ISSN 0975-4253. doi: 10.1177/0975425319859175.

United Nations. *World Urbanization Prospects The 2018 Revision*, volume 12. United Nations, 2019. ISBN 9789211483192. doi: 10.4054/demres.2005.12.9.

Van de Ven, F. and Voortman, B. De waterbalans van een stedelijk gebied; ervaringen in twee meetgebieden in Lelystad. *H2O*, 18(8):170–176, 1985.

World Bank. The Msimbazi Opportunity : Transforming the Msimbazi Basin into a Beacon of Urban Resilience (Vol. 2) : Volume A - Strategy and Management Framework (English). Technical report, World Bank Group, 2019. URL http://documents.worldbank.org/curated/en/694491555396781552/Volume-A-Strategy-and-Management-Framework.

Xue, Z., Charonko, J. J., and Vlachos, P. P. Particle image velocimetry correlation signal-to-noise ratio metrics and measurement uncertainty quantification. *Measurement Science and Technology*, 25(11), 2014. ISSN 13616501. doi: 10.1088/0957-0233/25/11/115301.

Yang, S. Q., Tan, S. K., and Lim, S. Y. Velocity distribution and dip-phenomenon in smooth uniform open channel flows. *Journal of Hydraulic Engineering*, 130(12):1179–1186, 2004. ISSN 07339429. doi: 10.1061/(ASCE)0733-9429(2004)130:12(1179).

Zhu, X. and Lipeme Kouyi, G. An Analysis of LSPIV-Based Surface Velocity Measurement Techniques for Stormwater Detention Basin Management. *Water Resources Research*, 2019. ISSN 19447973. doi: 10.1029/2018WR023813.

A

From rivers to discharges: a guide

This document provides a guide for setting up a gauging site for LSPIV purposes. The different steps of this guide are with a specific case in mind: (1) monitoring flood waves (2) using a fixed camera (3) with an incline (4) at a set interval. An introduction to LSPIV is provided in Section 2.3 of the main report. In Section 2.4 the basics of the image preparation and PIV processing is provided.

A.1. Setting up the gauging site

When setting up the gauging site, the following points should be taken into account, regarding (1) camera placement, (2) data collection and storage, (3) ground control points, (4) water level gauging, and (5) river characteristics. Before all, a potential gauging site should contain enough seeding during increased water levels – at least 10% of the surface – and an area of interest should be chosen (where the bathymetry is measured).

A.1.1. Camera placement

When setting up the camera, the following requirements and recommendations should be taken into account:

1. *Camera choice* The camera should have a high enough resolution – i.e. seeds need to be distinguishable – and should provide the possibility to film by night (e.g. night vision). Further research has to be done to access whether night time imagery can be used for the LSPIV method. To improve seed visibility, an additional light source could be applied.

2. *Clear view* Make sure that the location chosen provides a clear view on the river. Vegetation, pillars or any other objects in the line of sight of the camera, will reduce the accuracy of the results obtained. Also, take the floodplains into account for this assessment.

3. *Limited camera movement* Camera movement will reduce the method's precision. Preferably, the camera is placed against a wall, or any other rigid structure, or stabilisation on the videos should be applied during the image preparation step.

4. *Limited incline* The best LSPIV results are obtained when filming at an incline between 15°and 30°, relative to nadir. An incline up to 85°should be possible, but at this point, errors increase significantly.

5. *Limit environmental factors* Water droplets, lens flares and sun glints in the water reduce the LSPIV accuracy. Sun glints and lens flares can be (partly) prevented by pointing the camera with its back to the sun. Water droplets (and lens flares) can be prevented by adding a cap to the camera.

A.1.2. Data collection and storage:

Next to the camera placement, data collection and storage has to be considered. These considerations can be divided into the following items:

1. *Video frame rate* Approximately 20 till 25 frames per second is adequate for acquiring accurate flow velocities. The higher the frame rate, the more storage space is needed.
2. *Video length* Videolengths of 5 till 10 seconds are adequate for acquiring accurate flow velocities, the longer the video, the higher the precision. However, longer videos need more storage space.
3. *Trigger* Storing videos should be triggered when a flood wave is occuring. A trigger could be collected to e.g. the water level, or precipitation observed upstream. An example of a trigger based on water levels is presented in Figure A.1. An other alternative is a trigger based on precipitation levels.
4. *Storage* It has to be considered whether imagery is stored and processed on site, or send over the internet and processed on a server. If imagery is directly send over the internet, there is a possibility to loose frames due to slow connections. If imagery is saved on site, imagery compression might be necessary to decrease file sizes.

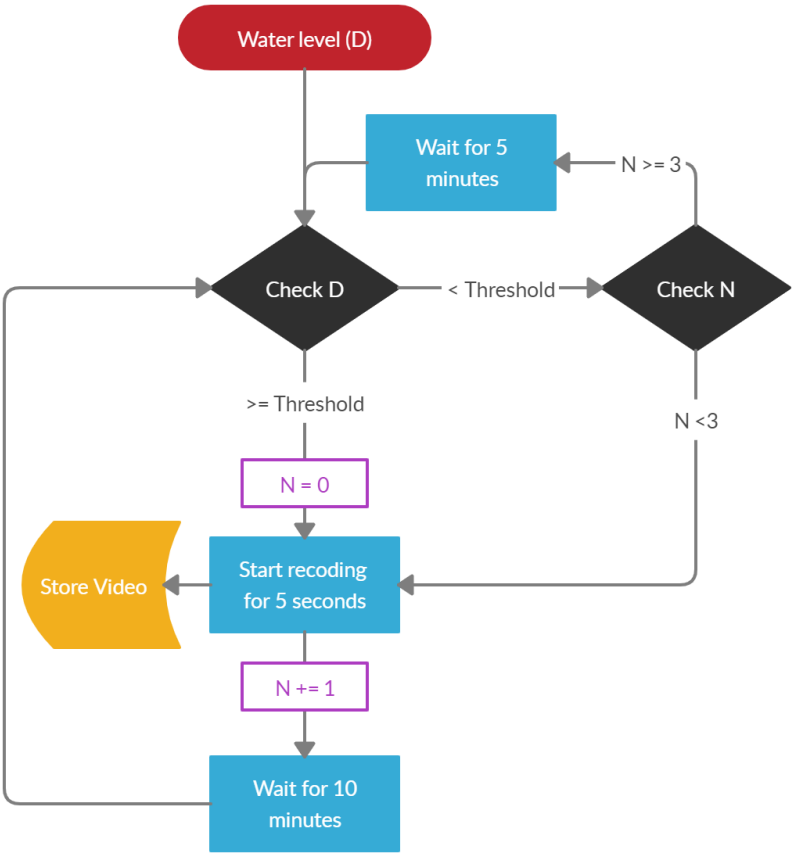

Figure A.1: Example flow chart of a trigger set-up based on the water level. If the water level is below a certain threshold, the camera will continue to gather imagery for at least 30 minutes.

A.1.3. Ground control points

Along the river, within in the line of site of the camera GCPs should be placed – preferably at different sides of the river to reduce errors. These GCPs are used for the orthorectification – and of necessary stabilisation – of the imagery. A minimum amount of 6 GCPs are necessary, but more are recommended. The longitude, latitude, and height of each GCP can be determined using geometry of (preferably) GPS (e.g. U-blox GNSS). These GCPs should be visible during different flood wave stages

A.1.4. Water level gauging

To determine discharges, the water level during each video is needed. These water levels can be obtained *electronical* – e.g. by using a radar gauge – or *visually* by extracting the water level from the imagery (automatically). The latter approach is not preferred, as debris can block the staff gauge resulting in unreadability.

A.1.5. River characteristics

The following river characteristics are needed in order to perform the complete post-processing:

1. *Bathymetry* To determine discharges, the bathymetry fo the whole river – including potential floodplains – are needed.
2. *Depth-average coefficient* To convert surface flow velocities to depth-averaged flow velocities, the empirical depth-average coefficient is used. To estimate this coefficient, several vertical profiles of the flow velocities should be measures at different cross-sectional sections and water level stages.

A.2. Image manipulation

To prepare the imagery for PIV processing, the following steps should be applied. In Section 2.4 provides in-depth information on the different manipulation steps.

1. *Lens distortion correction* To remove lens distortion, the camera characteristics are needed – i.e. the focal length and optical centre.
2. *Stabilisation* If there are significant camera movements, stabilisation should be applied.
3. *Orthorectification* To eliminate the effect of perspective distortion, orthorectification is applied using the GCPs. In this research, orthorectification was performed based on four GCPs. However, as the GCPs are (probably) not in the same plane as the water level, more GCPs should be used. For this processing it is advised to use a pinhole model as explained in Jodeau et al. (2008). During the orthorectification process the pixels per metre is set – e.g. 100 px/m – and unwanted outer areas can be removed.
4. *Gray scaling* Turns the imagery in gray scale.
5. *Contrast- and gamma correction* to enhance visibility of seeds by applying contrast- and gamma correction. This process should be related to the light intensity.

(a) Original frame **(b)** Manipulated frame

Figure A.2: Example of the full image manipulation process for imagery obtained at the Chuo Kikuu. Sequentially, the image is lens distortion corrected, orthorectified, and turned into gray scales with additional gamma correction.

A.3. PIV processing

The PIV processing provided is based on the use of OpenPIV (version 0.21.3) in Python. The software is still under development and – at the moment of writing – the current version is 0.22.2. The latest addition is the possibility to adjust the search area (Originally, the search area was the same as the interrogation area.) The runtime of the PIV processing step is mainly based on the sizes of the interrogation windows, search areas, size of the imagery, and number of frames.

1. *Input* two (subsequent) images, frame rate, dimension (pixels per meter), interrogation window size (pixels), search area size (pixels), overlap interrogation windows (pixels).
2. *Output* xy-coordinates of the interrogation window centres, Vx (flow velocity in the x direction), Vy (flow velocity in the y direction), signal-to-noise ratio – providing the certainty of a found flow velocity based on similarity.

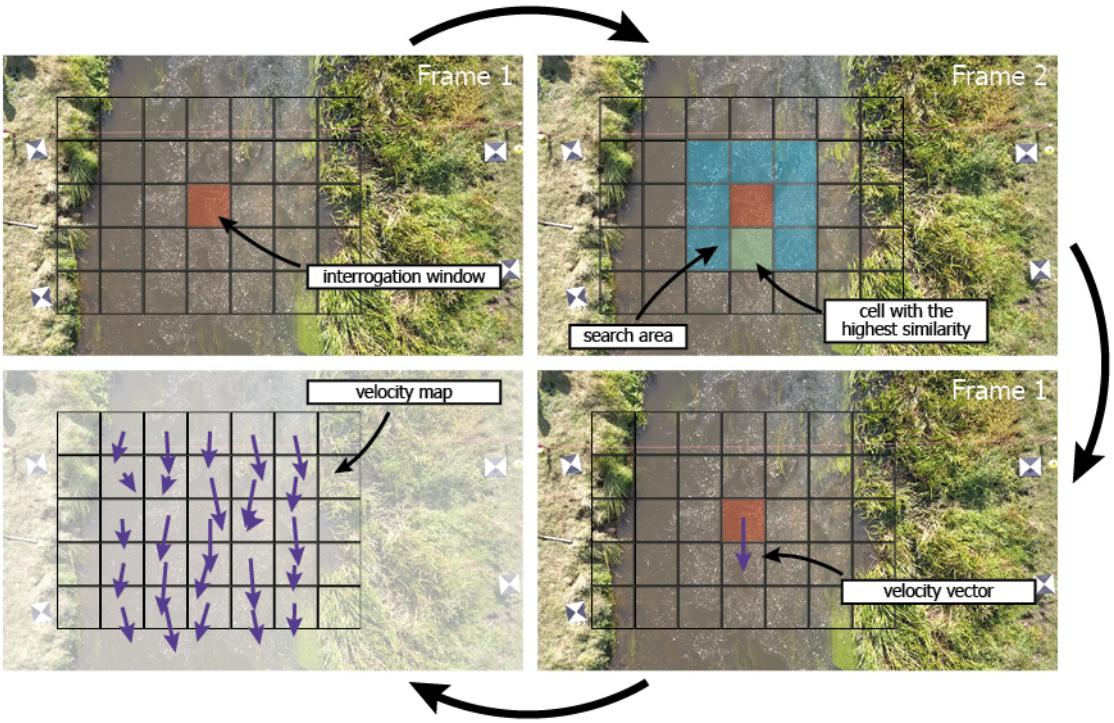

Figure A.3: Schematic view of the LSPIV method where a interrogation window is determined (the grid is drawn larger dan usually applied) in the first frame and present seeds are compared to a search area in the sequential frame 2 to determine their displacements. By multiplying the displacement with the frame time period, the velocity is determined. When applying this over the whole image, a surface flow velocity map can be created for each individual frame.

A.4. Post-processing

Due to insufficient seeds, flow velocities obtained using the LSPIV are usually underestimating the actual flow velocities. To obtain more accurate results, post-processing can be applied. In this research, two post-processing are applied: (1) flow velocity filtering, and (2) flow velocity substitution (*see* Section 5.5).

1. *Filtering* Removal of low flow velocities, if high flow velocities are found. Optimally, this filtering is based on the bimodality of cross-sectional section results: if bimodality is found, remove the lowest distribution based on Otsu's thresholding (Otsu, 1979).
2. *Substitution* At points where during the video length no seeds are detected, no flow velocities are found. These flow velocities could be estimated based on the vertical logarithmic progression relationship of the surface flow velocities. Based on known surface flow velocities and the local depth a relationship can be made how the surface flow velocities evolve when the water level changes. This relationship is based on the filtered surface flow velocities.

After the post-processing, average surface flow velocities and uncertainty bandwidths can be estimated for each cross-sectional section within the area of interest.

A.5. Discharge estimation

Discharges are estimated using the velocity-area method (*see* Section 2.2.1). The following steps are applied. Uncertainty bands can be created to use different percentile flow velocities instead of the average flow velocity.

1. *Interpolation surface flow velocities* The surface flow velocities are interpolated (for example quadratic) to estimate the flow velocities over the whole river width. Flow velocities at the river's banks are set to zero.
2. *Depth-averaged flow velocities* The surface flow velocities are converted to depth-averaged flow velocities using the aforementioned estimation of the depth-average coefficient.
3. *Interpolation of the bathymetry* The bathymetry is interpolated to the same coordinates as the depth-averaged velocities.
4. *Water depth estimation* Water depths are estimated by determining the distance between the bathymetry and water level.
5. *Discharge estimation* By multiplying the water depth, depth-averaged flow velocity, and section width, and summing these products together for the whole width, discharges are estimated.

A.6. Validation

To improve or validate the found results, some benchmark measurements should be performed. These are:

1. *Surface flow velocity validation* The surface flow velocities can be validated by optically tracing debris within videos, or by using current meters just below the river's surface or a radar gun.
2. *Discharge validation* Discharges can be validated using the sudden gulp salt dilution method or an ADCP (preferred).

If there are (large) offsets in results between the benchmark measurements and the LSPIV method. The post-processing could be adjusted, or – if the surface flow velocities are correct – the depth-average coefficient reconsidered.